Doctoral Dissertation
Doctoral Program in Materials Science and Technology (32th Cycle)

Thermochemical energy storage with salt hydrate composites: from materials design to lab-scale reactor validation

Sergio Salviati
* * * * * *

Supervisors
Prof. Alberto Fina, Supervisor
Prof. Federico Carosio, Co-Supervisor

Doctoral Examination Committee:
Prof. Luisa Cabeza, Referee, Universidad de Lleida
Prof. Camilo Rindt, Referee, Technische Universiteit Eindhoven
Prof. Candida Milone, Referee, Università degli Studi di Messina
Prof. Vittorio Verda, Referee, Politecnico di Torino
Prof. Alberto Frache, Referee, Politecnico di Torino

Politecnico di Torino
March 6, 2020

I hereby declare that, the contents and organization of this dissertation constitute my own original work and does not compromise in any way the rights of third parties, including those relating to the security of personal data.

………………………………....

Sergio Salviati

Turin, March 6, 2020

Summary

The development of improved heat management technologies is a mandatory step in the mitigation of greenhouse gases emissions. In particular, innovative Thermal Energy Storage (TES) systems can introduce significant improvements in energy production and usage. Already developed TES technologies include the storage of sensible heat in high thermal capacity materials (i.e. water) or the use of latent heat of phase change materials. Thermochemical energy storage is an innovative TES approach that focuses on the sorption/desorption reaction of a gas/solid system and inorganic salt hydrates are known as valuable candidates for the application of this technology. When these materials are heated, they produce water with a dehydration reaction. The salt is maintained dry by keeping it isolated from the environment, thus storing heat for a theoretically unlimited period. Heat is then delivered to the environment by rehydrating the material. The main advantages of this technology are i) a high energy storage density and ii) the possibility to trigger the energy release independently on ambient conditions, thus offering efficient solutions in applications such as seasonal storage in household and waste heat recovery in industrial processes. Since salt hydrates present limitations such as low cyclability, corrosivity, slow hydration/dehydration kinetics and low thermal conductivity, they may be enclosed in a porous matrix to form composite materials. These compounds are then included in thermochemical reactors, designed to fulfill the heating needs of a considered application.

In this PhD thesis, $MgSO_4 \cdot 6H_2O$, $LaCl_3 \cdot 7H_2O$ and $SrBr_2 \cdot 6H_2O$ were selected after a careful literature screening and evaluated as thermochemical materials. While all of them were found suitable for thermochemical energy storage, only $SrBr_2 \cdot 6H_2O$ was exploited for the preparation of composites due to its fastest sorption and desorption rates and chemical stability up to at least 50 hydration/dehydration cycles. A wet impregnation process was used for materials

preparation, using expanded graphite as porous conductive matrix, as well as including polyelectrolytes or cellulose nanofibers as binders. A decrease in the salt grains size on the graphite lamellae compared to state of the art salt/graphite composites was obtained, coupled with an energy storage density higher than expected due to the active contribution of the binders to the storage process. Freeze-drying procedure was also applied as an alternative preparation route, obtaining porous structures with sorption kinetic increased by 50% with respect to the pristine salt. Further studies on the binders' sorption/desorption reactions showed a strong effect of their concentration on performance. An optimal binder/graphite weight ratio of 0.5/1 was identified. Higher concentrations lead to hindrance phenomena in water mass transfer from the salt hydrate.

Composite powders were then pressed into tabs to obtain a modular and scalable design. The presence of hydroscopic binders resulted in an increase in sorption kinetics and mechanical stabilization compared to salt/graphite composites. The tabs were also exploited in a lab scale open thermochemical reactor including a 0.3 l material bed, obtaining an output power in the range of a few tens of mW/g. Different closed reactors were also evaluated, comparing a state of the art system to a design in which evaporator and condenser are formed by two physically uncoupled surfaces, obtaining a better control on water condensation. A thermo-fluidodynamics model was also developed and validated on a closed reactor to predict heat and water mass transfer phenomena. Condensation surfaces can also be defined in the model with the identification of saturated humidity volumes.

Overall, this thesis evaluated the performance of salt/graphite/binder thermochemical materials and different reactor concepts, demonstrating the possibility of efficient improvements in thermochemical salt hydrates towards their application in heat storage systems.

Acknowledgment

To my family

Contents

List of Tables

List of Figures

List of abbreviations

ACF	Activated Carbon Foam
CEM	Controlled Evaporator Mixer
CFD	Computational Fluid Dynamics
CMC	Carboxymethyl cellulose
CNF	Cellulose NanoFibers
DSC	Differential Scanning Calorimetry
EES	Electrical Energy Storage
FD	Freeze Drying
G	Expanded Graphite
g	Graphene
GFC	Gas Flow Controller
IEA	International Energy Agency
LAH	Lithium Acetate dihydrate
LFC	Liquid Flow Controller
PAA	Polyacrylic acid
PCM	Phase Change Material
PDAC	Poly diallyldimethylammonium chloride
SAH	Sodium Acetate trihydrate
SBH	Strontium Bromide Hexahydrate
SEM	Scanning Electron Microscope
SIM	Salt in porous Matrix
TCM	Thermochemical Storage Material
TES	Thermal Energy Storage
TGA	Thermogravimetric Analysis
TPS	Transient Plate Source
WI	Wet Impregnation
XRD	X-Ray Diffraction

List of symbols

$[H_2O]_{cry}$	$[mol\ m^{-2}]$	Salt hydrate water concentration
$[H_2O]_{liq}$	$[mol\ m^{-2}]$	Condenser water concentration
$[H_2O]_{vap}$	$[mol\ m^{-3}]$	Air water vapor concentration
A	[-]	Antoine constant
B	[°C]	Antoine constant
BL	[W]	DSC baseline
C	[°C]	Antoine constant
C_p	$[J\ °C^{-1}]$	Heat capacity at constant pressure
$C_{p,air}$	$[J\ kg^{-1}\ °C^{-1}]$	Air specific heat capacity
$C_{p,w}$	$[J\ kg^{-1}\ °C^{-1}]$	Water specific heat capacity
D_w	$[m^2\ s^{-1}]$	Diffusivity of water vapor in air
DSC	[W]	DSC signal
E_c	$[J\ g^{-1}]$	Composite energy storage density
E_d	$[J\ g^{-1}]$	Experimental energy storage density
E_{exp}	$[J\ g^{-1}]$	Expected energy storage density
E_l	$[J\ g^{-1}]$	Energy storage density reported in literature
E_{PDAC}	$[J\ g^{-1}]$	PDAC energy storage density
E_{SBH}	$[J\ g^{-1}]$	Experimental SBH energy storage density
E_{SBH_G}	$[J\ g^{-1}]$	SBH_G energy storage density
g	$[m\ s^{-2}]$	Gravity acceleration vector
J$_w$	$[mol\ m^{-2}\ s^{-1}]$	Diffusion flux vector of water in air
K	$[N\ m^{-3}]$	Viscous forces vector
k_1	$[s^{-1}]$	Dehydration reaction equilibrium constant
k_2	$[s^{-1}]$	Condensation equilibrium constant
m	[g]	Sample mass
M_{air}	$[g\ mol^{-1}]$	Air molecular weight
m_s	[g]	Starting sample mass
M_w	$[g\ mol^{-1}]$	Water molecular weight
m_w	[g]	Water mass
$\dot{m}_w$	$[g\ h^{-1}]$	Inlet water vapor mass flow
$\dot{m}_{w,air}$	$[g\ h^{-1}]$	Air flow
$m_{w,cry}$	[g]	Theoretical salt hydrate crystallization water
$M_{w,desorbed}$	$[g\ mol^{-1}]$	Desorbed water molar weight
$M_{w,hydrate}$	$[g\ mol^{-1}]$	Salt hydrate molar weight
$\dot{m}_{w,out}$	$[g\ h^{-1}]$	Outlet water vapor mass flow
p	[Pa]	Pressure
p_0	[Pa]	Standard pressure
$P_{air,out}$	[W]	Inlet air power

$P_{air,out}$	[W]	Outlet air power
p_w	[Pa]	Water vapor pressure
$p_{w,sat}$	[Pa]	Water vapor saturation pressure
Q	[J]	Heat
$\dot{Q}$	[W]	Heat flux
$\mathbf{q}$	[W m^{-2}]	Heat flux vector
Q_s	[J]	Sensible heat
Q_s	[J s^{-1}]	Heat source or sink
R	[J K^{-1} mol^{-1}]	Gas constant
r	[mol m^{-3} s^{-1}]	Reaction rate
RH	[-]	Relative Humidity
R_w	[mol s^{-1}]	Rate of water production or consumption
T	[°C]	Temperature
t	[s]	Time
T_1	[°C]	Inlet temperature
t_1	[s]	Starting time
T_2	[°C]	Outlet temperature
t_2	[s]	Ending time
T_a	[°C]	Ambient temperature
T_{hs}	[°C]	Heat source temperature
$\mathbf{u}$	[m s^{-1}]	Flow velocity vector
w_c	[%]	Composite weight
w_e	[%]	Experimental weight loss
w_{PDAC}	[%]	PDAC weight
w_{SBH}	[%]	SBH weight
w_t	[%]	Theoretical weight loss
X	[-]	Mixing ratio of water vapor in air
x_{PDAC}	[-]	PDAC weight fraction
x_{SBH}	[-]	SBH weight fraction
x_{SBH_G}	[-]	SBH_G weight fraction
α	[-]	Dehydration conversion
ΔG	[J/mol]	Molar Gibbs free energy difference
ΔH	[J/mol]	Molar enthalpy difference
ΔH_{PC}	[J]	Latent heat of phase change difference
ΔH_r	[J]	Latent heat of reaction difference
$\Delta \dot{m}_w,$	[g h^{-1}]	Water vapor mass flow difference
ΔP_{conv}	[W]	Convective power difference
ΔS	[J K^{-1} mol^{-1}]	Molar entropy difference
ΔT	[°C]	Inlet/outlet temperature difference
λ	[W m^{-1} K^{-1}]	Thermal conductivity
ρ	[g cm^{-3}]	Density

Chapter 1

State of the art

1.1 Thermal storage applications

Human influence on climate change is one of the most challenging issues ever faced by society. In 2015, representatives from 195 countries met in Paris during the United Nations Framework Convention on Climate Change and adopted a universal program to fight climate change, known as the Paris Agreement. This decision consists in a collaborative effort to fight global warming and establishes as main goal the reduction of the average global temperature increase below 2 °C, comparing it to the average temperature of the pre-industrial revolution period. The countries involved in the agreement must mobilize financial resources and improve policy frameworks towards the development and application of new technologies in order to reduce the impact of climate change [1].

One of the most important causes of climate change is the enhancement of greenhouse gases in the past decades. In particular, CO_2 emissions coming from fossil fuels have more than doubled since the early seventies and increased by around 40% from 2000 to 2017, as shown in Figure 1 [2].
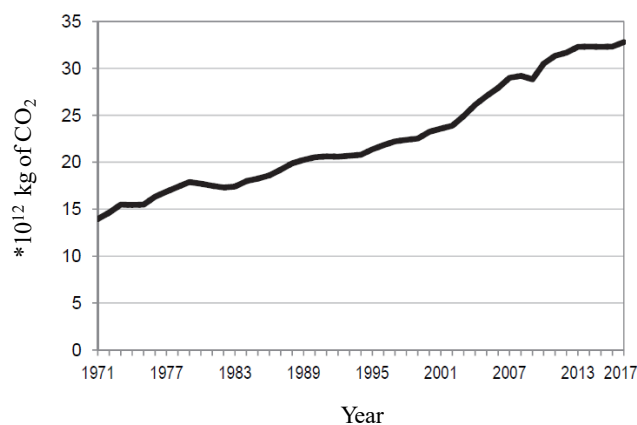
Figure 1. Mass of CO_2 emitted by anthropogenic sources worldwide. Adapted from [2].

In order to limit the anthropogenic contribution to the emissions growth, it is compulsory that all technological fields in the energy sector are improved towards a highly sustainable system [3]. In this frame, energy storage technologies have a high potential in the fight for climate change, by enhancing the systems energy efficiency, reducing wastages and facilitating the implementation of renewable energy technologies. Energy storage is mainly represented by Electrical Energy Storage (EES) and Thermal Energy Storage (TES) [4]. EES comprises technologies that use electrochemical accumulators, compressed air, supercapacitors, superconducting magnetic storage or fuel cells. [5]. On the other hand, TES includes techniques to store sensible or latent heat.

Smart heat management is nowadays a central topic in greenhouse gases mitigation and the approach of TES has a key role in achieving this goal. According to a model developed by Arce et al. [6], these technologies have been proven to have a potential reduction in CO_2 emissions that may significantly contribute to meet the Paris agreement goals. In 2014, the International Energy Agency (IEA) outlined the most relevant applications in which TES could provide the greatest benefits. TES applications are classified in three main categories depending on the temperature of the stored heat: low temperature (<10 °C), medium temperature (10-250 °C) and high temperature (>250 °C) thermal storage [7]. Low temperature storage is mainly applied in air conditioning systems, cooling substances such as water when power generated from the grid is cheaper or easily available (e.g. because of intermittent energy sources) and reusing the stored cold when needed [8]. The main high temperature application is Concentrating Solar Power technology, where heat from the sun is reflected by mirrors, concentrated in a small area and used to produce electricity with a heat engine. TES is used to provide a constant heat source to the engine, minimizing the interruptions in electricity generation [9].

Medium temperature TES comprises a broad range of applications, listed in Table 1. This thesis focuses on technologies in this field because of the great opportunities offered in terms of energy efficiency and performance improvement [10]. Seasonal storage takes into account the storage of extra heat from solar thermal collectors in summer and its usage in winter instead of other energy sources, in particular for household or public buildings heating [11]. The main operations performed in this sector are space heating, open air swimming pool heating, domestic hot water preparation, and cooking [12]. Transmission and distribution congestion relief comprehends all the technologies that allow a temporal or geographical shift in energy supply or demand to diminish excess load in bottleneck grid points. Demand shifting could alleviate the energy usage during peak hours by splitting supply and demand in different times, generating energy when it is cheaper or more easily available. Off-grid technology takes into account the need of heating in regions where the access to the energy grid is difficult or impossible, where people rely on fossil fuel for their energy needs. Energy storage can provide benefits in this field by increasing the amount of renewables in off-grid applications. The introduction of renewables has the inherent problem of having a variable energy production in comparison to fossil fuels. Variable supply resource integration could

be easier with efficient storage technologies to match production and demand. Waste heat utilization takes into account the collection and reuse of heat outcomes from industrial processes as byproduct [13]. Eventually, combined heat and power is a highly efficient use of fuels since it consists of the production of electricity and heat at the same time, minimizing the byproducts.

Table 1. Relevant applications for medium temperature thermal energy storage considered by IEA [7].

Application	Size (MW)	Discharge duration	Cycles	Response time
Seasonal storage	500-2000	Days to months	1-5 per year	Day
Transmission and Distribution congestion relief	10-500	2 h - 4 h	0.14-1.25 per day	> 1 h
Demand shifting	0.001-1	Minutes to hours	1-29 per day	<15 min
Off-grid	0.001-0.01	3 h – 5 h	0.75-1.5 per day	<1h
Variable supply resource integration	1-400	1 minute to hours	0.5-2.0 per day	<15 min
Waste heat utilization	1-10	1 h to 1 day	1-20 per day	<10 min
Combined heat and power	1-5	Minutes to hours	1-10 per day	< 15 min

IEA report [7] compares the applications using as parameters the system size, evaluated as the amount of energy to be stored, the discharge duration, strictly connected to the heat power output of the system, the typical number of charge/discharge cycles and the required time needed to ramp up the system (response time).

In addition to these fields, thermal storage is also employed in batch processes to enhance the amount of recovered waste heat, thus reducing energy consumption and costs [14]. Other applications are found in the vehicles sector, recovering thermal energy from the powertrain or exhaust gases for an efficient heat management in internal combustion [15] or electric [16] engines, or for cabin and cargo cooling [17]. It is important to notice that all the required operating parameters differ substantially between the applications, thus requiring many different and versatile energy storage solutions.

The next chapter introduces the most common TES technologies.

1.2   Thermal storage technologies

The main established classification of TES technologies takes into account the phenomenon used to store heat. In particular, as it is shown in Figure 2, three main categories are proposed: Sensible Heat Storage Materials, Phase Change Materials (PCMs) and Thermochemical Storage Materials (TCMs).
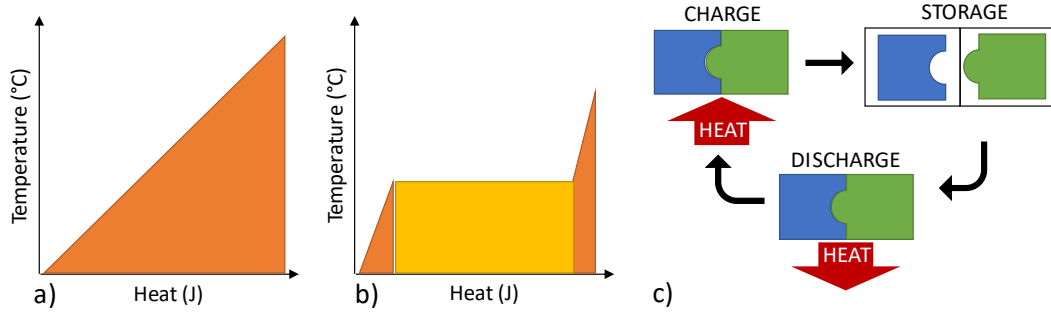
Figure 2. Principles of Thermal Storage technologies. a) Sensible Heat Storage, b) Phase Change Materials, c) Thermochemical storage.

In Sensible Heat Storage Materials energy is stored in the form of sensible heat (Q_s) and it is therefore dependent on the material heat capacity $C_p(T)$ and the difference between ambient temperature (T_a) and the heat source temperature (T_{hs}) following equation (1) [18].

$$Q_s = \int_{T_a}^{T_{hs}} C_p(T) \ dT \qquad (1)$$

Sensible Heat Storage technology is the most widely applied technology. Figure 3 shows the main sensible storage materials in an Ashby plot comparing two of their most important characteristics: specific heat and density. These materials are commonly classified depending on the presented phase at the usual temperatures of operation, liquid or solid.

The main liquid storage material (which is also the most used thermal storage material above all) is water, being it environmentally friendly, easily available, dense and with a high heat capacity. Artificial or natural water reservoirs are used for a great number of heat storage applications, from short-term to even seasonal heat storage [19].

The most commonly used solid materials for storage are rocks, metal, concrete, sand and bricks. Solid storage has many advantages compared to liquid storage materials, such as higher operating temperatures (> 100°C) absence of leakage issues and high thermal conductivity. Their main problems are a low specific heat compared to water and the need for more complex geometries including heat exchangers to transport the heat between the storage medium to a heat transfer fluid.
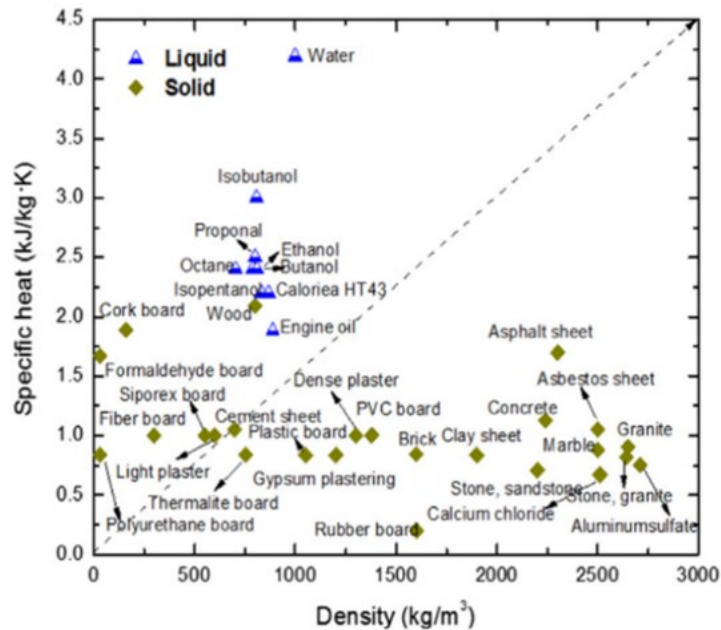
Figure 3. Thermal properties of sensible heat materials. Reprinted from [18], Copyright (2016), with permission from Elsevier.

An example of sensible heat seasonal storage system is reported in Figure 4. Heat is accumulated by an array of solar thermal collectors placed on buildings roofs and stored underground using a heat transfer network. Heat pumps then recover the stored thermal energy delivering it to the buildings via a heat distribution network. This principle was applied in Drake Landing Solar Community (Alberta, USA) [20], where more than 90% of the energy used for space heating in winter is provided by the TES system.
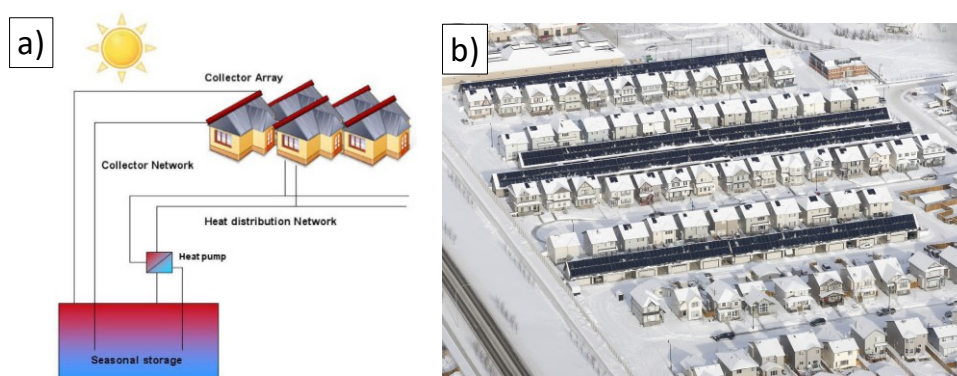
Figure 4. a) Scheme of sensible heat seasonal storage concept for buildings, reprinted from [19], Copyright (2010), with permission from Elsevier and b) aerial view of Drake Landing Solar Community [21].

PCMs use latent heat of phase change (ΔH_{PC}) to enhance the energy storage density of a material in addition to Q_s, as shown in equation (2).

$$Q = Q_s + \Delta H_{PC} \qquad (2)$$

This technology allows to enhance the energy storage density of sensible heat storage materials with a contribution of latent heat of phase change [22]. While different phase change mechanisms are considered in literature, the most used one is solid/liquid because it is easier to implement in TES systems than liquid/gas and has a higher energy density than solid/solid transitions.

Figure 5 shows a comparison of different solid/liquid PCM classes. Considering the wide intervals of melting enthalpy and temperature employed by the different materials, PCMs are versatile candidates for many different applications.
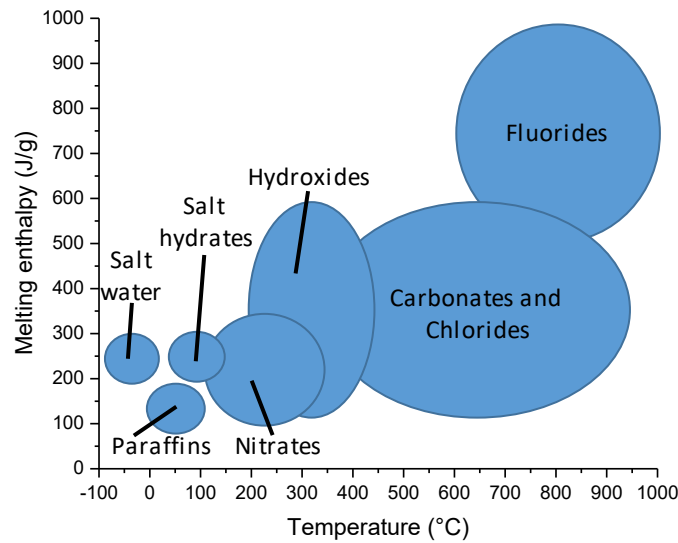
Figure 5. Classification of solid/liquid PCM classes.

In order to avoid leakages and materials degradation, encapsulation is a mandatory procedure in the use of solid/liquid PCMs. Two main strategies are defined depending on the scale of the encapsulating structure: microencapsulation (1-300 μm) and macroencapsulation (>1 cm) [23]. Figure 6 shows examples of commercial encapsulated PCMs.

PMCs performance were validated in different case studies in the built environment. For example, Figure 7 reports case studies in which these materials were implemented as insulators in bricks [24] and as heat sinks in photovoltaic panels [25].
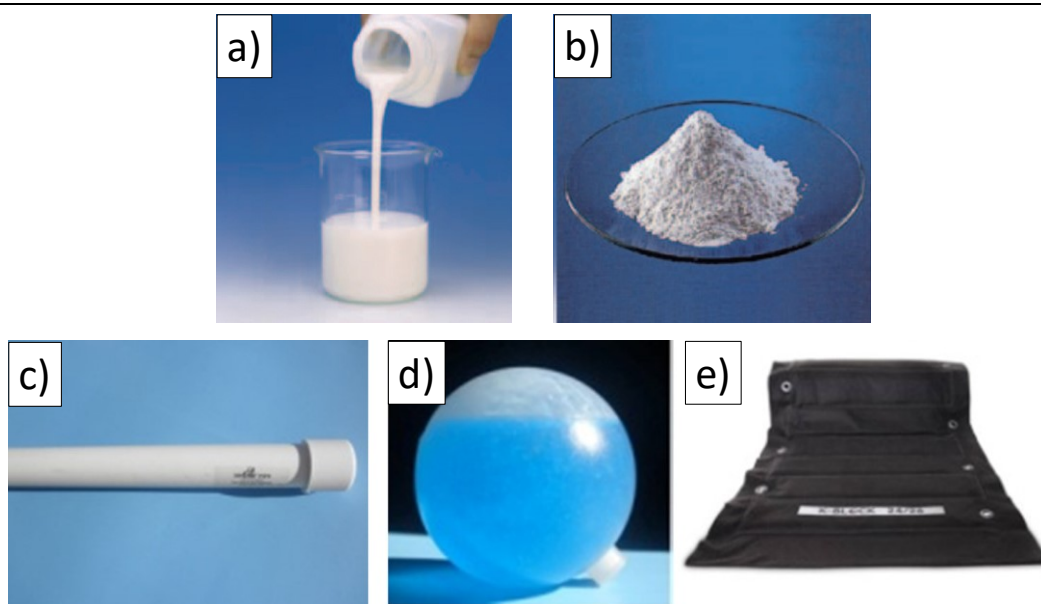
Figure 6. Encapsulation of commercial PCMs. Microencapsulation as liquid dispersion (a) and powder (b). Macroencapsulation as tube (c) sphere (d) or panels (e). Reprinted from [23], Copyright (2015), with permission from Elsevier.
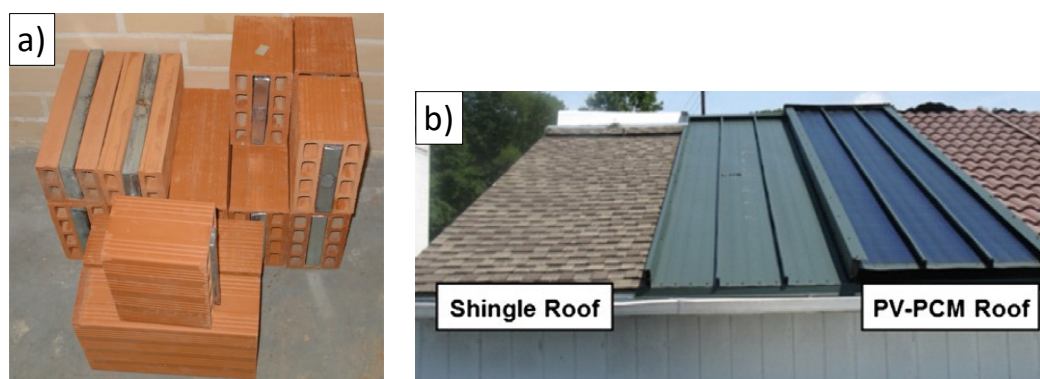
Figure 7. PCMs applications as insulators in bricks (adapted from [24]) and as heat sink of photovoltaic panels. Reprinted from [25], Copyright (2012), with permission from Elsevier.

Latent heat is used also in TCMs but, in this case, the reaction enthalpy of a reversible chemical reaction (ΔH_r) is used for energy storage as shown in equation (3).

$$Q = Q_s + \Delta H_r \qquad (3)$$

The process can be divided in three steps, as depicted in Figure 2. In the charge step, heat is provided to the TCM that reacts forming two products. In the storage step, the two products are separated to avoid their interaction. In the discharging step, the reverse reaction reforms the starting material providing thermal energy to the environment or to a heat exchanger.

One of the most important technological parameters in the classification of TES materials is the energy storage density, also called storage capacity, expressed in

terms of energy per mass or volume unit. Figure 8 shows the common values of the three classes for temperatures below 200°C.
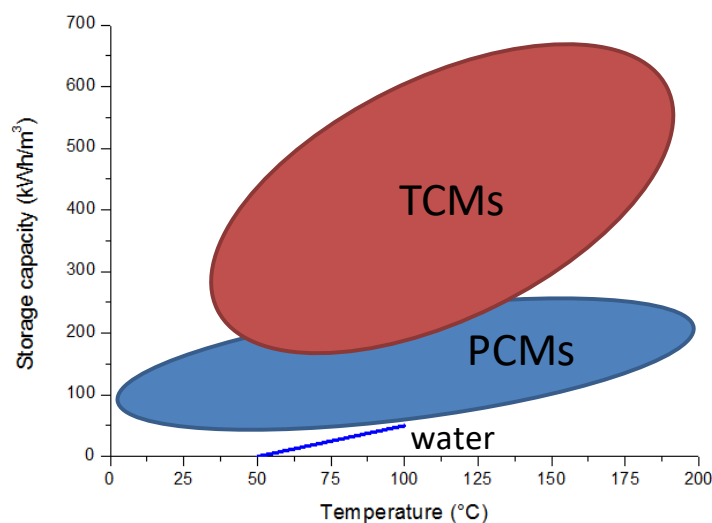
Figure 8. Classification of thermochemical storage materials in terms of storage capacity. Adapted from [26].

It is important to consider that, despite these materials values are intrinsic, the actual performance obtained may strongly depend on the system components needed for the TES process. In particular, sensible heat storage materials and PCMs require only a heat transfer between a source and a bulk mass, while on the other hand TCMs need to be included in systems with a higher degree of complexity, since they also comprise a two components chemical reaction. While the material storage capacity is a good first indicator of the overall volume of a TES reactor, each design must be independently evaluated based on the application-related criteria.

Supercooled PCMs for long-term storage

The phenomenon of supercooling in solid/liquid PCMs is related to the presence of the liquid state at temperatures below the melting point. While this effect is commonly considered a drawback that reduces performance [27], it can also be used for long-term heat storage as explained in Figure 9. Even if the material considered is a PCM, the storage process is similar to the thermochemical one. A solid material is charged with heat above its melting point and then cooled to lower temperatures. The material can be stored in its supercooled state for months to allow seasonal storage. Eventually, to begin the discharge phase, solidification is triggered by a mechanical stimulus.
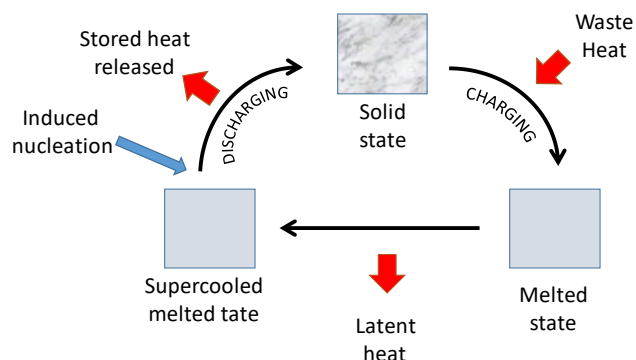
Figure 9. Concept of long-term storage with supercooled PCMs.

While properties of polyols were studied for supercooled heat storage [28], Sodium Acetate Hydrate (SAH) is a cheap material that is already implemented in commercial devices such as heat pads [29]. These are fabricated including SAH in a plastic bag, adding a trigger that is needed to easily trigger the salt nucleation and heat release (Figure 10).

Figure 10. Commercial heat pads (a), with details of flexible disc (b) and spring type (c) triggers. Adapted from [29].

1.3 Thermochemical energy storage

IEA compared different energy storage technologies relating the capital requirement and risk for their deployment, compared to their maturity level for both EES and TES [7] (Figure 11). EES comprises a broad variety of technologies that uses different phenomena to meet the needs of many applications. Short-term storage (seconds to minutes), comprises superconducting magnetic energy storage [30], flywheels [31] or supercapacitors [32] that present high performance, but still high deployment costs to become broadly applied. In long-term storage (hours to seasons), pumped storage hydropower [33] is at the present time the state of the art technology, while also some compressed air energy storage [34] facilities were deployed, despite their need for investment costs reduction. Battery storage field comprises all the technologies that store electricity using a chemical reaction, and includes different products with varied levels of readiness [35].

Regarding TES, technologies such as underground thermal energy storage [36,37], pit storage or cold-water storage [19] are already applied in different

facilities, mainly for district heating. Molten salt [38] and ice storage [39] are under development, the former applied to concentrating solar power, the latter for air conditioning and cooling.

Eventually, thermochemical energy storage was found as one of the least developed, while being very promising in terms of low capital investments and risk.
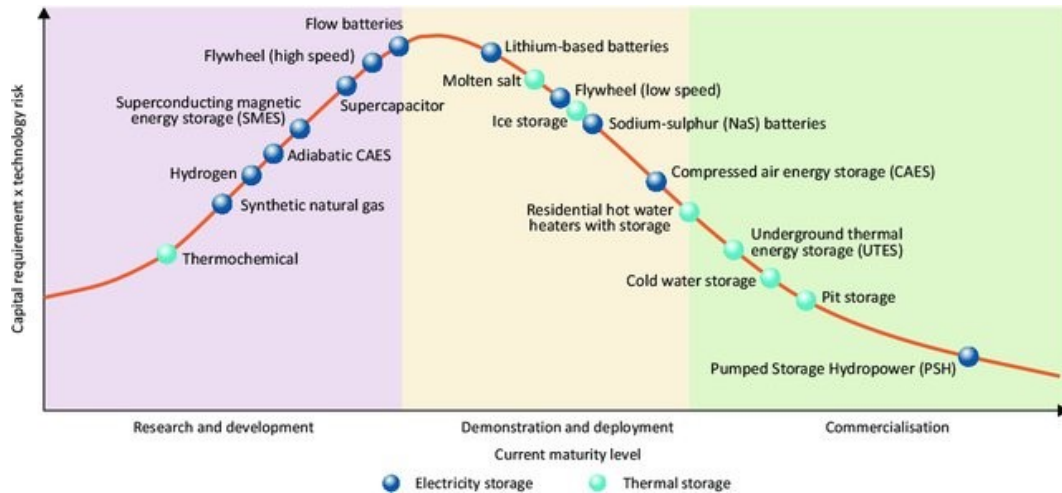
Figure 11. Comparison of energy storage technologies maturity levels, capital requirements and technology risk. Adapted from [7].

The main advantage of TCMs, together with a high energy storage density (Figure 8) is the achievability of a theoretically unlimited storage time, without issues of heat loss present in sensible heat storage and PCMs [40]. This effect is realized because in TCMs heat is stored by isolating the material from the environment in its dry state. In this way, all the system is kept in equilibrium temperature with the environment removing the heat losses issues and allowing a long-term storage, independently of ambient conditions. The same storage time was achieved by sensible heat storage only building large scale plants underground in order to minimize the heat losses, e.g. Drake Landing Solar Community (Alberta, USA) [20]. With these properties, TCMs are valuable in applications such as waste heat recovery from industrial processes and vehicles [41], micro-combined heat and power [42,43] and seasonal thermal storage in households [44]. Regarding this last subject at the present two international research projects focus on TCMs materials and systems: CREATE [45] and SWSHeating [46]. Both of them focus on the building sector and face the challenge of a scale up of currently developed materials and devices, deploying demonstrators in real constructions trying to realize a breakthrough in the application of this technology.

A common set of definitions and classifications of TCMs in literature is not yet established, and authors use the terms "sorption storage" and "thermochemical storage" with slightly different meanings [47]. The term "sorption storage" is generic since it describes the mechanism of interaction of a gas phase and a solid or liquid phase, independently on the type of bonds between the phases. On the other hand, "thermochemical storage" is related to a chemical reaction between the two phases triggered by temperature, thus technically excluding physisorption

phenomena. In this thesis, the term "thermochemical" will be used to define all kinds of solid/gas interactions, this being the most widely accepted definition in literature. One of the often used TCMs arrangement was presented by Yu et al. [48] and divide these materials in four classes: liquid/gas absorption, solid/gas adsorption, solid/gas absorption (chemical reaction) and composite materials (Figure 12).

Liquid absorption	Solid adsorption	Chemical reaction	Composite materials
• Two phase • Three phase	• Silica gels • Zeolites • Aluminophosphates • Silico-aluminophosphates • Metal organic frameworks	• Coordination reaction of ammoniates • Hydration reaction of salt hydrates	• Salt inside porous matrix
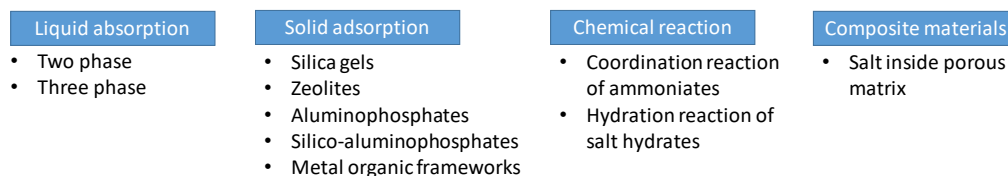
Figure 12. Classification of TCMs by Yu et al.

In liquid absorption, a vapor phase interacts with a solution during heating or cooling processes. The variation of concentration of the solute determines the exchange of heat of dilution with the environment. It is a mature and widely applied technology, in particular in the field of cooling circuits. The most commonly used solutes are lithium based ionic salts, such as LiBr [49] and LiCl [50] dissolved in water.

Regarding solid sorption materials, the main difference between solid adsorption and chemical reaction is the nature of the bond between sorbent and sorbate, that is physisorption for the former and chemisorption for the latter [48]. The most commonly investigated materials in this class are Zeolites (in particular 13-X), thanks to their high porosity and availability [51]. Also aluminophosphates were proven to be a promising opportunity for sorption storage, with high water loadings in particular for low temperature applications [52]. In the last years, Metal Organic Frameworks were investigated for TES purposes, demonstrating a high efficiency, but at the highest production cost in this class [53].

Chemical reaction storage materials are mainly composed of inorganic salts and are divided in two main classes depending to the nature of the sorbate (ammonia or water). The former class is still at an early research stage, presenting disadvantages such as high pressure of operation and safety in household environment [54]. On the other hand, salt hydrates/water reactions were tested and compared in a broad range of conditions and applications. Their issues compared to adsorption materials comprehend low chemical stability, material degradation over multiple cycles and low thermal conductivity, but they present the highest energy storage densities and fastest sorption kinetics in this field. Since salt hydrates performance can be improved on both materials and system design level, we decided to focus on this class. In the next chapter, the properties of different salt hydrates will be presented and discussed.

1.4   Salt hydrates material portfolio

Salt hydrates of general structure $M_nA_m \cdot XH_2O$ are capable of storing energy using a hydration/dehydration reversible reaction (a):

$$M_nA_m \cdot XH_2O + \Delta H_r \leftrightarrows M_nA_m \cdot (X-Y) H_2O + YH_2O \qquad (a)$$
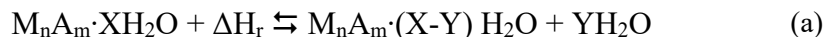
Salt hydrates selection is one of the most important steps in thermochemical systems design, because the vast variety of materials and the diversity of TES applications makes it challenging to identify the best candidates. The main parameters to consider in this process include commercial availability, possible health hazards, safety, price, chemical stability, hydration/dehydration cyclability, energy storage density, reaction kinetics and reversibility. Different reviews [47,55–65] were previously published and aimed at the selection of salt hydrates are summarized in Table 2.

Table 2. Published papers on thermochemical salt hydrates selection.

Source	Salts analyzed	Application focus	Heat temperature (°C)	Method used
N'Tsoukpoe[47]	4	Seasonal storage in households	90-180	Literature review, thermal analysis
Trausel et al. [55]	5	Seasonal storage in households	150	Calculation from thermodynamic data
N'Tsoukpoe et al. [58]	125	Micro-combined heat and power	105	Literature review, thermal analysis
Yan et al. [59]	5	Waste heat recovery	90-200	Literature review
Deutsch et al. [60]	4528	Different applications	25-1000	Mathematical search algorithm
Donkers et al. [61]	262	Seasonal storage in households	100	Literature review, thermal analysis
Richter et al. [62]	308	Waste heat recovery	300	Literature review, thermal analysis
Donkers et al. [63]	4	Seasonal storage in households	150	NMR analysis
Kiyabu et al. [64]	163	Industrial processes	50-600	First principle calculations
Afflerbach et al. [65]	29	Renewable heat storage	100-400	Mineral classification search algorithm
Palacios et al. [56]	9	Seasonal storage in households	150	Literature review
Gutierrez et al. [57]	6	Waste heat recovery	300	Thermal analysis

In recent years, extensive effort was focused in the classification, screening and selection of salt hydrates. While different application targets and temperature ranges were considered, there is a particular focus on medium temperature storage (10 to 250 °C) for waste heat recovery in industries and seasonal storage in households. Table 3 reports the temperature ranges for different typical heat sources for those two applications.

Table 3. Waste heat temperatures for selected industrial sectors.

Source	Temperature range (°C)
Flat plate solar thermal collectors [10]	up to 80 °C
Steel production – cooling water [66]	20 to 40
Municipal waste heat [67]	-6 to 90
Chemicals production – water sources [66]	45 to 82
Mining industry [67]	-25 to 65
Data centers [68]	25 to 70
Evacuated tube solar thermal collectors [10]	up to 160 °C
Steel production – other sources [66]	190 to 400
Glass production [66]	140 to 200
Chemicals production – gas sources [66]	230 to 340

From those data emerges the presence of an additional subdivision of medium temperature sources in two sub-groups, below and above 100 °C, respectively.

The most used selection method follows a systematic approach, starting from a list of commercially available materials, discarding the ones with toxic or hazardous properties and evaluating the performance of the rest with thermoanalytic techniques, including Thermogravimetic Analysis (TGA) and Differential Scanning Calorimetry (DSC). However, some of the most recent reviews [64,65] try to identify new salt hydrates applying search algorithms to materials databases

In addition to works on salt selection, some salt hydrates were studied in detail. Table 4 reports their main properties as reviewed by Donkers et al. [61], Trausel et al. [55] and N'Tsoukpoe et al. [58]. For each salt different reaction mechanisms at different temperatures can be considered. In this case, the most widely studied reactions for applications below 150 °C are reported, resulting in temperatures of operation in the range 29-140 °C. All the materials present energy storage densities higher than PCMs, which are usually lower than 300 J/g [69]. The reported densities are for the salts in the highest hydrate condition. Those values are usually reduced when the materials dehydrate. The volumetric energy storage density is also reported, since it is of great importance in many applications. All the prices are obtained for industrial grade materials, with the only exception of $LaCl_3$, which is reagent grade.

$MgSO_4$ [70–76] and $CaCl_2$ [77] are among the most widely evaluated salts because of their high energy storage densities compared to their low cost [70–76]. Also $SrBr_2$ was widely studied because of its high chemical stability and storage density, but at a higher market price [78]. Another advantage of this salt is its high density, which is linked to a volumetric energy storage density comparable to

$MgSO_4$ and $CaCl_2$. $MgCl_2$ also received great attention because of its high storage density, while presenting poor chemical stability due to the formation of gaseous HCl [76,79–83]. On the other hand, K_2CO_3, despite its low energy density, provides low corrosivity making it compatible with metal components [80,84]. Na_2S [80,85,86], Na_2SO_4 [73] and $LaCl_3$ [87] were preliminarily considered as promising salts and need additional tests towards performance evaluation. Some double salts, byproducts of mining industry processes, were also proven to be usable as thermochemical storage materials [88] [89]. Those salts present a good opportunity because, despite presenting low energy storage densities and more complex dehydration reaction steps than pure salts, they have low production costs. Carnallite ($KCl \cdot MgCl_2 \cdot 6H2O$) is reported as an example.

Table 4. Main properties of selected salt hydrates.

Salt hydrate	Reaction	Energy storage density (J/g)	Temperature (°C)	Density (g/cm^3)	Volumetric energy storage density (kJ/m^3)	Price (€/kg)
$MgSO_4$	$MgSO_4 \cdot 7H_2O \leftrightarrows MgSO_4 \cdot H_2O$	1363	49	1.67	2.28	0.077
$CaCl_2$	$CaCl_2 \cdot 6H_2O \leftrightarrows CaCl_2 \cdot H_2O$	1265	29	1.71	2.16	0.29
$SrBr_2$	$SrBr_2 \cdot 6H_2O \leftrightarrows SrBr_2 \cdot H_2O$	948	89	2.39	2.27	2.4
$MgCl_2$	$MgCl_2 \cdot 6H_2O \leftrightarrows MgCl_2 \cdot 2H_2O$	1255	117	1.56	1.96	0.18
K_2CO_3	$K_2CO_3 \cdot 1.5H_2O \leftrightarrows K_2CO_3$	691	80	2.16	1.49	1
Na_2S	$Na_2S \cdot 5H_2O \leftrightarrows Na_2S \cdot 0.5H_2O$	1684	80	1.58	2.66	0.65
Na_2SO_4	$Na_2SO_4 \cdot 10H_2O \leftrightarrows Na_2SO_4$	1749	30	1.46	2.55	0.054
$LaCl_3$	$LaCl_3 \cdot 7H_2O \leftrightarrows LaCl_3 \cdot 1H_2O$	958	91	2.22	2.13	664
Carnallite	$KCl \cdot MgCl_2 \cdot 6H_2O \leftrightarrows KCl \cdot MgCl_2$	688	140	1.59	1.09	0.031

1.5 Salt hydrates limitations

While salt hydrates present excellent properties regarding their use as thermochemical materials, the implementation of those materials in a system designed to address a real application presents several limitations, including poor chemical stability, high corrosivity and low thermal conductivity.

Chemical stability

The evaluation of salt hydrates stability is mandatory in the design of TCM based system. Both the interaction of the salt with the environment and the chemical modifications that occur in the salt upon repeated sorption and desorption cycles must be evaluated. Salt deliquescence is the phenomenon of the salt transforming into a liquid solution through excessive water sorption from the environment. Deliquescence was found to cause leakages and morphology changes due to salt solubilization and recrystallization [90]. Another structural change is the formation of cracks caused by water mass transfer to and from the salt during hydration and dehydration [91]. This phenomenon reduces the volumetric energy storage density of the material by enhancing the salt bed volume cycle by cycle, eventually introducing the risk of a damage of the reactor if the salt volume exceeds the one of its storage tank in the reactor. Also the change in performance of the sorption/desorption reaction must be considered. In this case, each salt hydrate must be considered separately because every chemical species react differently when exposed to hydration/dehydration cycles. For example, a dramatic reduction of hydration time for $K_2CO_3 \cdot 1.5H_2O$ by 10-12 times after 12 cycles caused by crack formation was reported [92]. On the other hand, $CaSO_4 \cdot 2H_2O$ was tested for 10 cycles and, while the sorption time remained almost constant, the amount of absorbed water diminished due to the formation of a new crystal phase unable to hydrate. On the other hand, $SrBr_2 \cdot 6H_2O$ showed better stability, maintaining its performance unvaried over 10 cycles [93]. Further tests are required to investigate the cyclability of those materials in large-scale devices and up to a higher number of cycles, even developing accelerated aging techniques.

Corrosion

In thermochemical reactors, TCMs are usually placed in a storage tank, in which the materials are in direct contact with the walls of this vessel and the surfaces of other components, e.g. heat exchangers. The use of metals for the assembly of those components is common, due to their high availability, high thermal conductivity and low cost [94]. However, salt hydrates corrosivity issues are to be carefully addressed. Corrosion tests were realized to evaluate the reactivity of common metals, such as copper, stainless steel, carbon steel and aluminum in direct contact with salt hydrates at different temperature and humidity conditions, simulating real applications. All the metals resulted with corrosion damage after the exposure to different kinds of salts, finding stainless steel as the most resistant. The variation of the temperature and humidity conditions introduced to reduce the corrosivity is not enough to prevent irreversible damage to the metals [95,96].

Stainless steel was further tested in contact with strontium bromide, finding a high corrosion rate (1 mm/year) at 80°C and 35% RH. The corrosion mechanism was studied in depth, highlighting that the presence of atmospheric CO_2 causes the generation of the byproducts $SrCO_3$ and HBr that enhance the corrosivity. [97]Corrosion was also found in large scale using strontium bromide in a reactor made of aluminum, without quantitatively evaluating it [98]. Another issue was found in chloride salts, that produce gaseous HCl at temperatures close to the operational range of TCMs (e.g. 167 °C for $MgCl_2$) [83]. One solution for this issues can be the use of different materials for the reactors components (i.e. polymers or ceramics), which typically have lower thermal conductivity compared to metals. Another approach is the surface treatment of metals with paints, with a careful evaluation of coating defects, since those are preferential sites for corrosion phenomena.

Thermal conductivity

The applicability of TCMs depends also on the performance in term of heat transfer rate between the active material and the components of the thermochemical system in which the material is included. Beside the issues related to the use of corrosion resistant materials for the vessel and heat exchanger surfaces, heat transfer phenomena in the active thermal storage phases should be carefully addressed. While convection phenomena are mainly related to the reactor geometry, conduction is a property of the material. It is particularly important for applications because it is linked to the heat flux **q**, and therefore to input and output heat power, by Fourier's law (Equation (4)):

$$\boldsymbol{q} = -\lambda \nabla T \qquad (4)$$

Here λ is the thermal conductivity and ∇T is the temperature gradient between the surface and core of the active material. During the charging step in low temperature applications, ∇T is usually low because of the small difference between the environment temperature and the reaction temperature of the salt hydrates. Also in the discharging step, if heat is not efficiently removed from the material bed, the salt temperature could increase excessively and reach values that do not thermodynamically allow the hydrated phase, thus hindering the hydration reaction. In these cases, high values of thermal conductivity are required. The thermal conductivity of different salt hydrates used as TCMs are typically in the range 0.7-1.0 W/mK [99]. These values are one order of magnitude lower than the typical ones found for the metals used for reactors components (e.g. ~15 W/mK for stainless steel [100]) and can therefore be a limiting factor in heat transfer. Different technological approaches are applied to overcome these limitations. At material scale, salt hydrates are mixed with substances that present high thermal conductivity and resistance to corrosion, such as graphite [101]. At reactor scale, heat extraction is obtained using a heat transfer fluid, e.g. air in direct contact with the salt bed or a liquid with the use of a heat exchanger. Various concepts are

applied to salt bed containers in order to maximize the heat transfer efficiency between the active material and the fluid [94].

Mass transport

Hydration and dehydration reactions in salt hydrates are based on the interaction between water vapor and solid surfaces. Since these materials are commonly used in powder form, two different phenomena affect the reaction kinetics: the diffusion of water molecules inside the salt grains and water transport between the environment and the grain surface [102]. Both phenomena were characterized using different grain size and bed thicknesses, finding that the kinetics is affected more by airflow fluid dynamics than by diffusion [70]. A careful design of thermochemical reactors geometry is therefore necessary for the application of TCMs [103].

1.6   Salt hydrates-based composites

The main approach used to improve the performance of salt hydrates is their combination with other materials in the preparation of composites. Two main approaches are identified: salt hydrates mixtures and stabilization with a matrix (Figure 13).
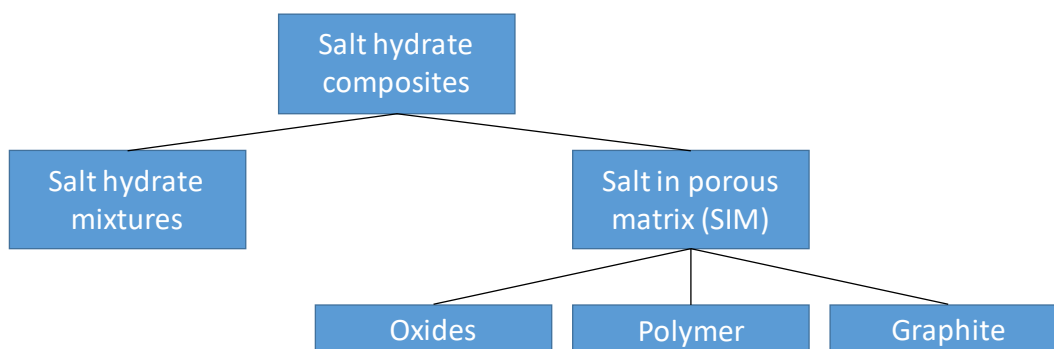
Figure 13. Classification of salt hydrates composites.

Mixtures of salt hydrates, also called doped salt hydrates, consist of the combination of two materials sharing a common cation or anion. The mixture $MgCl_2/CaCl_2$ was deeply studied with both computational [81,104] and experimental [90,105] methods. Other mixture considered were $MgCl_2/MgSO_4$ [106] and $KCl/CaCl_2$ [101]. Those composites show increased cyclability and chemical stability, a reduction of deliquescence ad a limitation of undesired side reactions. The main advantage of this approach is the improvement of salt hydrates properties without a considerable reduction in the energy storage density, since both materials introduced in the composite participate to the thermochemical storage process. On the other hand, it is impossible to overcome some issues common to all the salt hydrates class, such as corrosion.

The most widely used approach in improving salt hydrates performance is relative to their stabilization in matrices. Figure 14 shows the principles of the design of a composite Salt in porous matrix (SIMs).
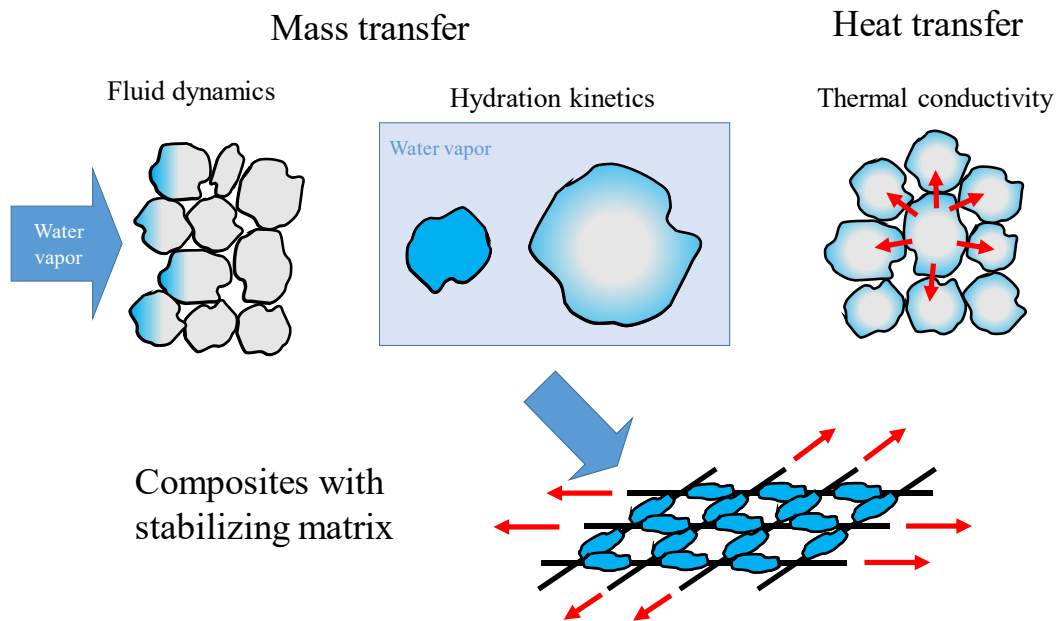
Figure 14. Principles of composite thermochemical materials design.

The supporting material should allow a good mass transfer of water in air between the salt grains, a high diffusion of molecules in the bulk and a high input/output thermal power, related to thermal conductivity. A high grade of porosity is a mandatory requirement in order to allow an optimal salt loading. In addition to these, the matrix should allow a higher stabilization of the salt, preventing agglomeration, leakage and morphology changes due to volume expansion of the salt after several hydration/dehydration cycles.

Different techniques were developed in literature to prepare SIMs:

- Mixing: the components are mixed together and grinded with mortar and pestle [107].
- Wet Impregnation: the matrix is impregnated with a water based salt solution and the solvent is removed with heating [101].
- Molten Salt Impregnation: the salt is heated above its melting temperature and then used to impregnate a matrix [101].
- Encapsulation: in which a core-shell structure is realized, where the core is the active material and the shell is used to stabilize it. This technique is widely applied in PCMs fabrication [108].
- Precipitation: the salt hydrate and the matrix are dissolved in a solution. They react forming a precipitate that is subsequently filtered and dried.
- Spray Drying: the salt hydrate and matrix are dissolved in a solvent, sprayed on a surface and dried [109].

- Precursor derived incorporation: The matrix is synthetized *in situ* starting from precursors in the presence of the salt hydrate. The salt is included in the matrix while its formation reaction develops [110].

The commonly used matrices can be divided in three main categories: ceramics, polymers and graphite-related materials. Also copper [107] was tested because of its high thermal conductivity, but metals use should be limited because of corrosion issues [96]. The most widely used matrices are oxides, including silicates such as zeolites [92], silica gel, attapulgite, vermiculite [102] and pumice [113]. Those materials present advantages such as low density and high porosity, but with low thermal conductivities (comparable to salt hydrates). Some of the materials in this class, such as vermiculite, present costs that are definitely lower than salt hydrates. While those materials are easily available on the market, they present a higher complexity in morphology modification and performance improvement when compared to polymers or graphite.

A deep study on matrices composed by oxides is outside the scope of this thesis, which focuses on polymer-based and graphite-based materials. Table 5 lists the composite materials prepared with a polymeric matrix. Various encapsulation approaches were tested to implement polymers and elastomers with salt hydrates. The main goal of this approach is to stabilize mechanically the salt while maintaining satisfactory water transport from and to the surface salt grains. Encapsulation with spray-drying was demonstrated to enable stabilization of the salt expansion, also increasing the resistance to over-hydration and subsequent deliquescence and leakage [109,114]. Another approach consists in the addition of the salt hydrate during the synthesis of the encapsulating matrix, defined as incorporation. This technique was employed to realize siloxane-based [110] and alginate-based [115] foams, with the possibility to tune the composite morphology and properties varying salt loading.

Table 5. Known composite materials based on salt hydrates and polymeric matrix.

Source	Salt hydrates	Matrices	Preparation method
Kallenberger et al. [116]	$MgSO_4$	Polyvinyl pyrrolidone	Precipitation
Brancato et al. [110]	$MgSO_4$	Siloxane foam	Incorporation
Cuypers et al. [114]	$CaCl_2$	Polymer	Spray Drying
Gaeini et al. [109]	$CaCl_2$	Ethyl cellulose	Spray Drying
Kallenberger et al. [115]	$MgSO_4$, $MgCl_2$, $CaCl_2$, $SrCl_2$	Alginate	Incorporation

Graphite-based materials have been also considered for the fabrication of TCM composites because of their high thermal conductivity and porosity. Table 6 lists

the known composites materials comprising graphitic matrices. The most widely employed materials in this class are expanded graphite (G) and Active Carbon Foam (ACF). G, in particular, is obtained by chemical intercalation and thermal expansion of natural graphite, delivering a highly porous structure and surface area typically in the range of 30-60 m^2/g [117]. Expanded graphite was reported able to enhance hydration/dehydration rates in Thermogravimetric test, compared to pristine hydrated CaCl2 [101]. The use of expanded graphite results also in higher specific heat capacity with respect to the salt, allowing for the storage of more sensible heat [118]. It has been also demonstrated that the water permeability of the materials can be tuned by altering the density of the samples and is weakly influenced by the salt/graphite ratio [119].

Table 6. Known composite materials based on salt hydrates and graphitic matrix.

Source	Salt hydrates	Matrices	Preparation method
Opel et al. [107]	$MgCl_2 \cdot 6H_2O$	Graphite	Mixing
Druske et al. [120]	$CaCl_2$, KCl_2	G, ACF	Wet Impregnation, Molten Salt Impregnation
Yu et al. [121]	$LiCl \cdot H_2O$	G, ACF	Wet Impregnation
Korhammer et al. [101]	$CaCl_2$	G, ACF	Wet Impregnation, Molten Salt Impregnation
Cammarata et al. [118]	$SrBr_2 \cdot 6H_2O$	G	Wet Impregnation
Zhao et al. [119]	$SrBr_2 \cdot 6H_2O$	G	Wet Impregnation
Gaeini et al. [109]	$CaCl_2$	G	Wet Impregnation

While different research works were carried out to understand the structure and properties of salt hydrate composites, a definitive conclusion is not yet reached. Issues like morphology changes, cycling stability and scalability still affect the global systems efficiency. Different approaches can be combined to achieve SIMs or salt mixtures with higher performance. For example, salt hydrates stabilized with polymer encapsulation can be included in porous matrices in order to enhance sorption/desorption kinetics and thermal conductivity.

1.7 Thermochemical reactors introduction

The use of thermochemical energy storage presents multiple advantages over other technologies that uses sensible heat or PCMs. One of the main differences between those technologies is that TCMs working process requires the reaction of two components (most commonly water and a salt hydrate). This system requires

the need for the design of reactors with a higher level of complexity compared to other TES solutions. The optimal integration of TCMs in heat management systems is fundamental to make use of the materials properties.

The main classification used for thermochemical systems is between open and closed reactors [122] [94] as shown in Figure 15. In open reactors, air is taken from the environment and forced to flow through a TCM bed, serving as both heat and mass transfer fluid. During the charging step, hot air causes the material to dehydrate, while the heat release process is carried out with a humid flow at lower temperature. The main advantage of this system is that it is simple, compared to closed ones, while its main issues are the contamination between the environment and the material and the possible need of a humidifier to provide correct amount of humidity to the TCM. On the other hand, closed thermochemical reactors present a more complex design where the components are isolated from the environment. In addition to the TCM bed, a condenser is included to collect water during dehydration. These systems are usually evacuated and the mass transfer driving force is the difference in water vapor pressure between the TCM and the condenser [98]. A heat exchanger must also be included to transfer thermal energy between the bed and the environment. The design of a thermochemical reactor that allows the usage of the maximum potential of TCMs is very challenging and a satisfactory design is yet to be identified [123].
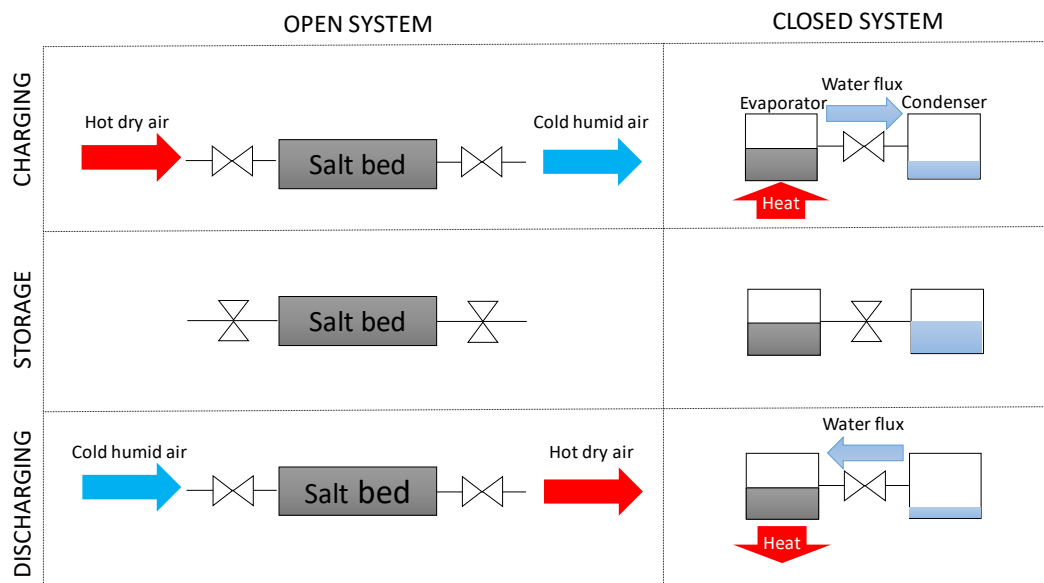
Figure 15. Comparison of open and closed system concepts in charging, storage and discharging steps.

A mandatory step in the design of a thermochemical reactor is the setting of the charging and discharging temperatures and pressures, which depend on the considered case study and on the reactor type. For example, for seasonal thermal storage in households where heat derives from solar thermal collectors and is used for space heating the system is charged at temperatures up to 120°C [124] and discharged at ambient temperature. In open systems, the driving force that triggers the sorption reaction is a temperature increase of the salt bed, together with a forced

airflow. On the other hand, in closed reactors the difference in water vapor pressures between evaporator and condenser must be taken into account. During the dehydration phase, the raise in temperature in the salt bed enhances the water vapor pressure that becomes greater than in the condenser. This phenomenon generates a difference in vapor pressures that allows the water transfer between evaporator and condenser. These systems are usually evacuated and operated at low pressures in order to remove the hindrance effect of air in water vapor transport. In hydration, evaporator and condenser are commonly kept at the same temperature (i.e. room temperature), or the condenser is heated with a low temperature source to obtain a higher water vapor pressure in the condenser, driving diffusion towards the salt bed and enhancing the absorption kinetics.

When choosing a TCM for the reactor, its phase diagram must be carefully taken into account. Temperature/pressure phase diagrams are commonly calculated using equation (5).

$$\Delta G = \Delta H - T\Delta S = -RT \ln \frac{p}{p_0} \tag{5}$$

Where G is the Gibbs free energy, H is the molar enthalpy, S is the molar entropy, R is the gas constant, T is temperature, p is pressure and p_0 is the standard pressure (1 bar at 20°C). ΔH and ΔS can be calculated with experimental or theoretical methods and then used in the equation. Some literature papers report values for enthalpy and entropy for a great variety of salts [61,125]. As an example, Figure 16 shows phase diagrams of the equilibrium for strontium bromide hydrate (chemical equation (b)).

$$SrBr_2 \cdot 6H_2O \leftrightarrows SrBr_2 \cdot H_2O + 5\ H_2O \tag{b}$$
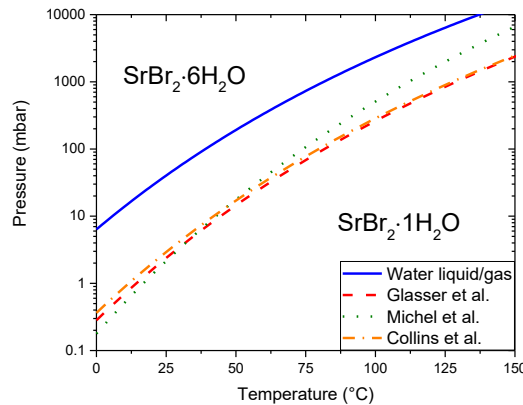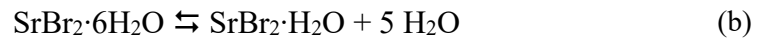
Figure 16. Phase diagrams for liquid/gas water and hexahydrate/monohydrate strontium bromide equilibria.

Different values of ΔH and ΔS were considered from the aforementioned work by Glasser et al. [125], from an experimental procedure by Collins et al. [126] and from Michel et al. [127]. The first two data match almost perfectly, while in the last

work a slightly mismatched curve is present. Figure 16 also shows the liquid/gas water equilibrium curve calculated with the Antoine equation [128].

As an example to illustrate the technological importance of the evaluation of a TCM phase diagram, we consider a closed reactor based on strontium bromide. Starting in a situation where the salt is at equilibrium in its hexahydrate state (e.g. at 12 mbar and 20 °C), if the evaporator is charged with a heat source at 100 °C, the monohydrate state becomes the stable phase and salt dehydration is thermodynamically possible. In order to collect the dehydrated water, the condenser must be kept at a temperature that allows the formation of liquid water (e.g. 20 °C). In this way the difference of evaporator and condenser water vapor pressures, 300 mbar and 10 mbar respectively, acts as driving force for water mass transfer, allowing the battery charge. For the battery discharge, if both evaporator and condenser are kept at 20 °C, the difference between the two water vapor pressures (30 mbar and 1 mbar respectively) allows the hydration of the salt.

An additional phenomenon to consider is the presence of a metastable zone for the hydrated/dehydrated salt equilibrium. Sögütoglu et al. [129] demonstrated that nucleation and growth phenomena in the transitions between different hydration states of the salts are of great importance in their application as TCMs. In particular, the presence of metastable zones in the phase diagrams limits the temperature and pressure range of operation of a salt hydrate. Figure 17 reports as an example hydration and dehydration studies on $K_2CO_3 \cdot 1.5H_2O$.
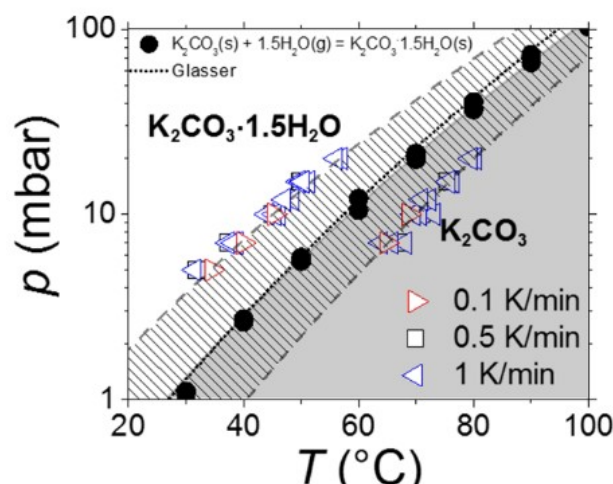
Figure 17. Metastable zone for $K_2CO_3 \cdot 1.5H_2O$. Adapted from [80].

The solid/solid reaction is hindered by nucleation effects. The transition between one phase to the other is mediated by the presence of a wetting layer and its mobility is dependent on the water vapor pressure. Since instantaneous nucleation happens at the metastable area boundary, temperature and pressure parameters in a reactor should be chosen outside this zone. The importance of this effect varies between the salt hydrates. For example, it is present in $CuCl_2 \cdot 2H_2O$ and $MgCl_2 \cdot 6H_2O$, but is almost absent in $LiCl \cdot H_2O$ [80].

1.8 Thermochemical reactors review

Different reactor designs were described in the literature and developed with the aim of evaluating the performance of TCMs in a laboratory scale, acquiring data towards a scale up in household or industrial environment. Zhang et al. developed an open reactor for space heating applications. Its structure is summarized in Figure 18 [130].
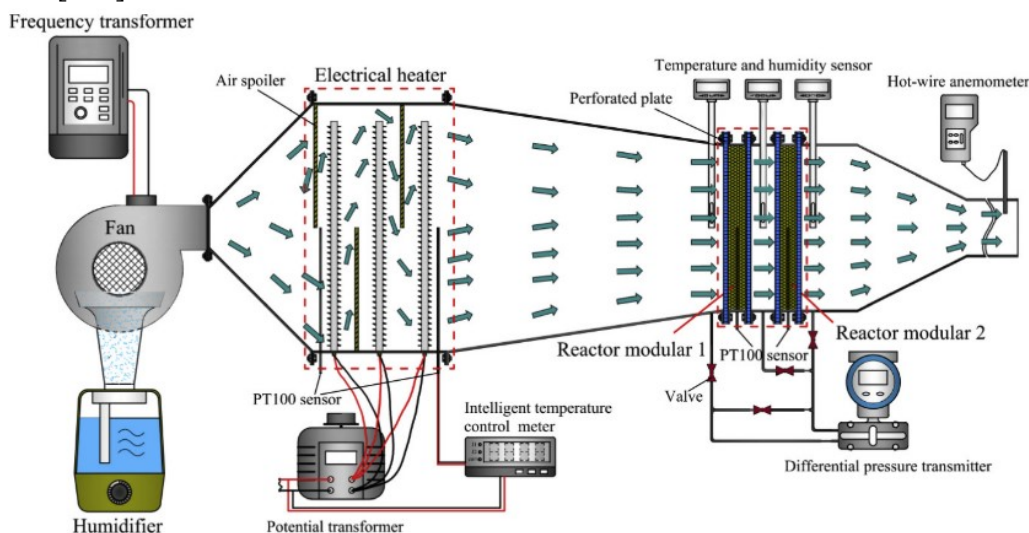
Figure 18. Schematic representation. Reprinted from [130], Copyright (2017), with permission from Elsevier.

The material used is a composite where LiCl is included in a matrix of activated alumina, weighting 6.5 kg. Air is blown over the TCM using a fan. A humidifier and an electrical heater are included in a system to set a desired air temperature and humidity. Temperature and humidity sensors are placed near the salt bed to evaluate the system performance. It is capable of storing 191 kWh/m^3 of thermal energy, providing air with a temperature higher than 30 °C for 7 h and an output power up to 137 W.

Gaeini et al. also realized an open system for space heating, using Zeolite 13XBF as sorbent material. A picture of the system is reported in Figure 19.

Figure 19. Zeolite based thermochemical system. Adapted from [131].

In this concept, the reactor is divided in four identical segments. In each of them, air is blown through a humidifier and a heater to adjust the air conditions and then through a tank filled with zeolites. Inlet and outlet temperatures and humidity are checked with sensors. The material energy storage density is 198 kWh/m^3, and it is almost halved if we consider the whole reactor volume (108 kWh/m^3). The system is able to provide a power of 3.6 kW for 10 h during its discharge phase. [131]

Johannes et al. realized a zeolite based reactor, reported in Figure 20 [132].
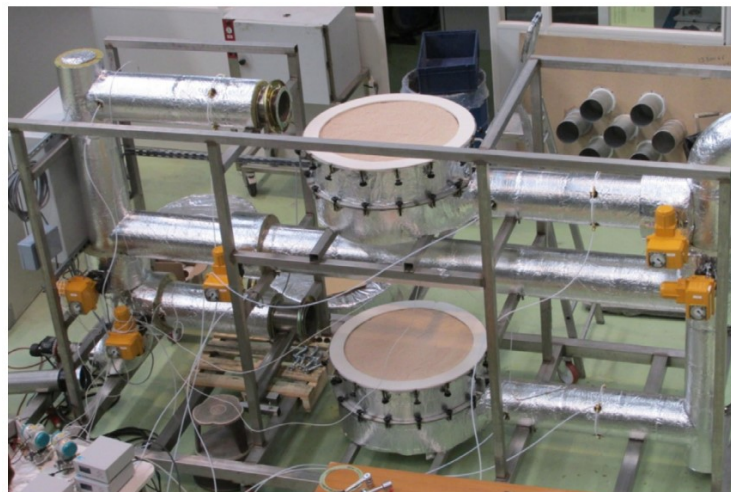
Figure 20. Zeolite based reactor realized by Johannes et al. Reprinted from [132], Copyright (2015), with permission from Elsevier.

80 kg of zeolite are used, divided in equal parts in two containers, in order to realize a modular device. Air is used as heat and humidity transfer medium. In this case, the system was designed to store heat when it is cheaper to generate it due to

low electricity prices, using it to fulfill the heating needs of a building in peak hours. The goal is therefore to obtain 2 kW or thermal power for 2 h. The reactor was able to outperform those criteria by providing 2.25 kW for 6 h.

The closed system developed by Palomba et al. uses 4.3 kg of the commercial zeolite-based water absorber AQSOA FAM Z02 [133]. The configuration is reported in Figure 21.

The zeolite is placed in chamber 1, while chamber 2 functions as a condenser/evaporator for water during the charging and discharging processes. The hydraulic system 3 is used to provide heat and cold fluids to the chambers and the vacuum valve 4 is operated to isolate the two chambers during the storage phase. The system is able to store up to 280 Wh/kg of thermal energy, providing a power output of 200-650 W.

Michel et al. designed a reactor comprising strontium bromide hexahydrate as TCM [134]. 400 kg of salt are distributed in a layered chamber (Figure 22). This setup is chosen to obtain a modular structure that can be upscaled or downscaled easily. Air is used as heat transfer medium to hydrate/dehydrate the TCM. Seven cycles were tested, finding power outputs up to 2 W/kg and an energy storage density equal to 388 kWh/m^3
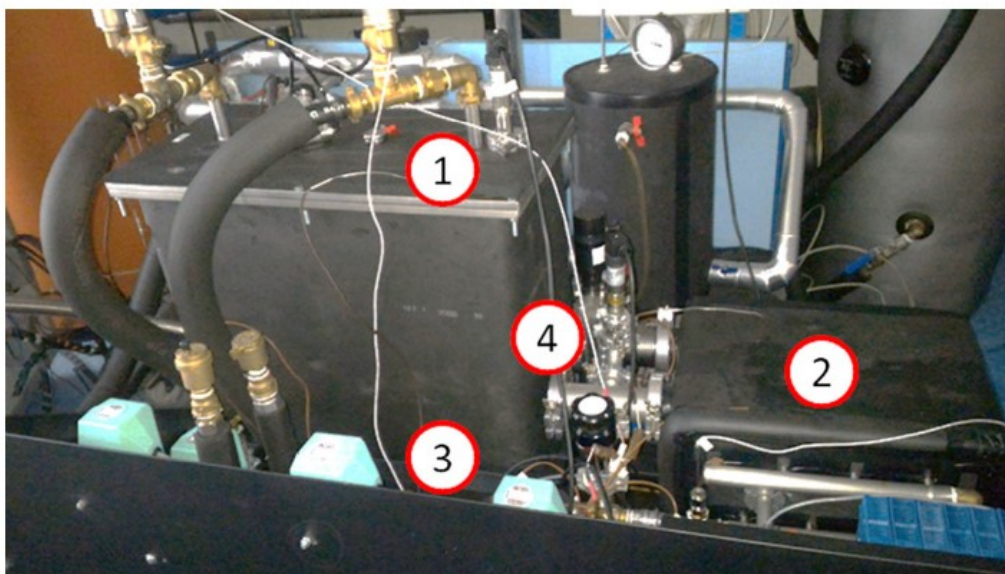
Figure 21. Thermochemical system by Palomba et al. Reprinted from [133], Copyright (2017), with permission from Elsevier.
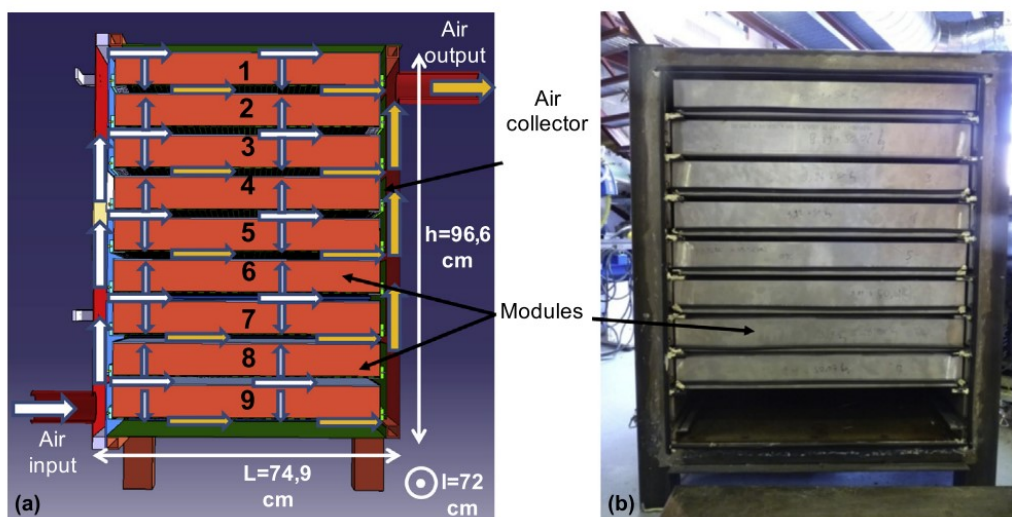
Figure 22. Modular TCM reactor chamber. Reprinted from [134], Copyright (2014), with permission from Elsevier.

Fopah-lele et al. presented a closed thermochemical reactor, reported in Figure 23 [98]. The system is operated under vacuum and is divided in two main chambers, placed vertically one on top of the other and linked by a valve. While the lower chamber operates as an evaporator/condenser and water storage tank, the upper one contains the salt, hold in an aluminum heat exchanger with a honeycomb structure that enhances the heat transfer. 1 Kg of salt was tested for 13 cycles, with an energy storage density of 65 kWh/m^3.
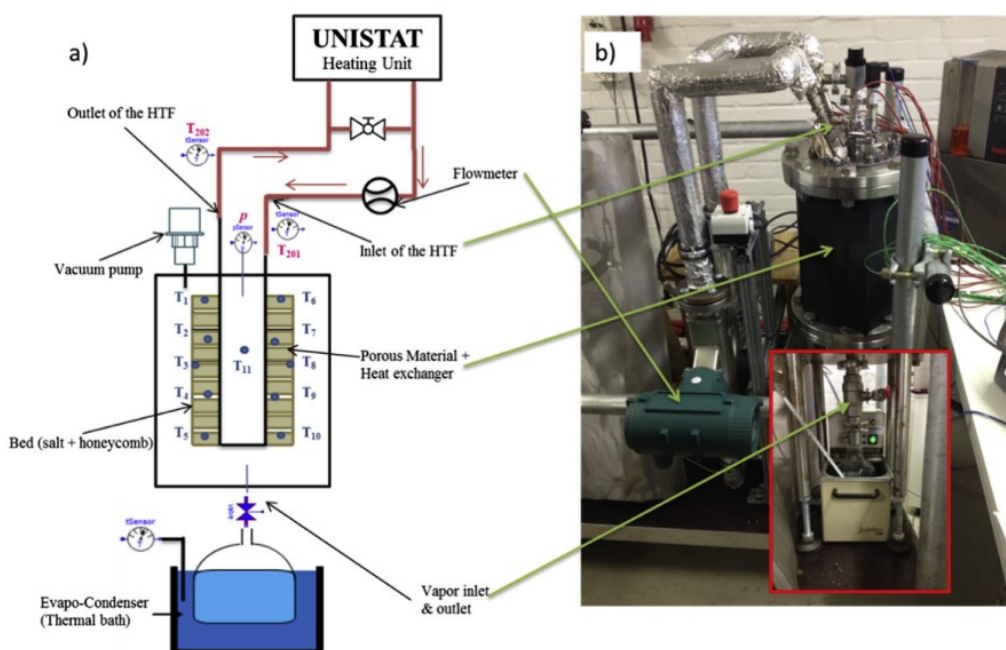
Figure 23. a) Schematics and b) picture of the closed thermochemical setup using strontium bromide hexahydrate realized by Fopah-Lele et al. Reprinted from [98], Copyright (2016), with permission from Elsevier.

In conclusion, multiple designs were tested at different materials scale. The main focus of all the above mentioned research papers is heating in households, an application that presents clear input/output requirements for parameters such as average temperatures, humidity and power. In this scenario, different setups were able to show the benefits of a thermochemical system, while presenting issues such as the difficulty of maintaining a constant output power for long times. Both open and close setups were proposed, with similar performances. The research works focused in this stage in understanding the relationship between a change in the reactor design or input parameters and subsequent variation in performance. An important feature to test in future works is the cyclability of the systems, in order to better understand their applicability, despite the number of cycles reported is usually limited and long-term stability remains to be assessed Furthermore, the scaling of the setups according to limited volumes present in already build houses is yet to be addressed. While many reactors focused on zeolites as TCMs, the same designs could be adapted also to use salt hydrates that, exploited in composite materials, could be beneficial in terms of energy storage density, thermal conductivity and sorption kinetics.

1.9 Multiphysical modeling of thermochemical reactors

The exploitation of computational models for the description of thermochemical reactors currently appears a very useful tool in their development and optimization. The main goal of thermochemical modelling is to study properties of the system that cannot be detected experimentally and predict changes in the setup geometry to improve its performance. Thermochemical reactor models can be grouped in three categories: steady state, spatially resolved and lumped parameter. Steady state models present the lowest level of complexity, allowing the representation of the system without taking into account any non-equilibrium phenomena. Their main disadvantage is the extreme simplicity, making them useful in preliminary analyses or for very simple systems. On the other hand, spatially resolved models permit to represent the real geometry of a reactor, taking into consideration all the constraints and processes of the real system, but with the highest computational costs. Lumped parameter models simplify a system dividing it into elements and taking into account only the most important mechanisms, trying to find a balance between accuracy and complexity [122].

Models for thermochemical storage with salt hydrates can be divided in two main groups depending on the scale considered. A set of developed models focuses more on the identification of the dehydration/hydration mechanisms in the salt hydrates and on thermodynamical evaluations on the species equilibrium states [72,135]. Other models describe the systems at a larger scale, studying the behavior of heat and mass transfer in salt beds and in reactors [136,137]. The two model scales can than interact with each other, with the possibility to give a complete explanation of the thermochemical process [138].

Okhrimenko et al. [72] used thermodynamical models to explain the presence of different hydration states in $MgSO_4$ at different temperature and humidity

conditions, fitting the experimental data obtained with X-Ray Diffraction (XRD) analysis. Their model describes the salt hydrate as a solid solution of water molecules in a bulk state of anions and cations. In this way, they were also able to predict non-stoichiometric forms of the salt, obtaining a complete overview of the stable and metastable states of hydration.

Lan et al. [135] focused on the realization of a model to explain the behavior of salt hydrates subjected to TGA. The model geometry is a TGA furnace and phenomena such as heat and mass transfer between the grains of $Li_2SO_4·H_2O$ and the environment are addressed with Computational Fluid Dynamics (CFD). The model describes the sorption/desorption process with the nucleation and growth of a new phase into the present phase. Differences in sample performance resulting from a change in masses, water vapor pressures and heating rates can be predicted by this model. The application of these findings to other salt hydrates could be a valuable tool to understand the differences in hydration/dehydration kinetics provided by different chemical species.

An open reactor model was developed by Hawwash et al. [136]. It uses $KAl(SO_4)_2·12 H_2O$ as salt hydrate, distributed in a cylindrical bed in which air is blown and used as heat and mass transfer medium. In particular, the variation in system performance caused by a change in bed geometry is addressed. Thermofluid dynamics parameters such as temperature and pressure drops were extrapolated from the model to evaluate the value of the use of a truncated cone instead of a simple cylinder as salt bed shape, varying in this way the inlet and outlet area. The optimal dimensions for the reactor are identified after seven different cases are discussed. The procedure developed in this work could be applied to other reactors in order to maximize the performance after selecting the application-related constraints.

Xu et al. [137] also studied the dehydration in a similar cylindrical salt bed in which $MgCl_2·6H_2O$ is included as reactant. This material is chosen because, while providing optimal thermochemical properties, it has a multi-step dehydration reaction, changing from the hexahydrate state to a tetrahydrate and then to a dihydrate. The goal of this model is to provide a method to analyze this phenomenon in the large scale, in order to predict the presence of the different dehydration steps that happen simultaneously inside the reactor.

Fopah-Lele et al. [138] proposed a 3D model for the performance evaluation of a closed thermochemical reactor. This work is based on the system formed by a honeycomb structure filled with $SrBr_2·6H_2O$ already discussed in the previous paragraph. The dehydration reaction is represented using the front reaction model, considering the salt bed present in a single honeycomb cell and defining a surface that divides the hydrated and dehydrated states. The surface moves through the salt bed while the reaction proceeds and allows the calculation of the total conversion. Those data are then fitted in the spatially resolved model to obtain a complete description of the reactor. In this case, different parameters were extracted from the simulation, e.g. the temperature distribution inside the reactor, the charging power and the energy storage density of the TCM.

Thermochemical storage is a complex process that takes into account multiple phenomena happening at different scales. Many approaches were tested in literature to evaluate salt hydrates properties or reactor performance. The majority of works focuses only on one of the two phases of the storage process, hydration or dehydration. While the most important from an application point of view is the discharge of the battery, because of more strict constraints of the heat power and temperatures required by the systems, it is important to develop complete models that can address both the thermochemical stages. Many works also simplified the reactor geometry in 1D or 2D model. While those results are valuable in the development of new methods in this field, full space resolved models are required for a complete description of thermochemical reactions, addressing their use in real applications.

1.10 Scope and structure of the thesis

While TCMs present excellent properties in view of applications for greenhouse gases emissions reduction, additional research and development is needed towards large-scale application of this technology. Salt hydrates present high energy storage density and fast sorption/desorption kinetics, but also important drawbacks such as low thermal conductivity, corrosivity and low chemical stability due to morphological modification after several hydration/dehydration cycles [102].

The main strategy to overcome those limitations is the inclusion of salts in porous matrices made of oxides, polymers or graphite. While enhanced performance was claimed by different authors, a revolutionary material was not yet identified. Expanded graphite used as matrix presents interesting properties such as high thermal conductivity and porosity, but has a low chemical compatibility with salt hydrates [119]. Encapsulation with polymers ensure a high mechanical stabilization, but introduces an inert phase that reduces the energy storage density and kinetics [109].

Different open and closed thermochemical reactors were proposed for applications such as cogeneration and space heating together with the development of preliminary spatially resolved models to fully understand the reactors performance [94].

Based on this scenario and current limitations, the work in this PhD thesis was focused on the improvement of thermochemical energy storage both introducing new approaches in the design of composite TCMs including graphitic matrices and polymeric binders. In addition, different thermochemical reactor designs are conceptualized and tested in laboratory scale devices.

This thesis is structured in six chapters:

Chapter 1 illustrates the state of the art of TES technology, with a focus on thermochemical energy storage. The properties and limitations of salt hydrates are addressed, in particular in the fabrication of composites. A review of thermochemical reactors and models is also presented and discussed.

Chapter 2 reports the materials and methods used to prepare the composite materials, as well as details on the characterization procedures employed

Chapter 3 focuses on the salts screening and selection in order to identify the best candidate for the preparation of composites. After a literature screening, three salt hydrates were selected (magnesium sulfate, strontium bromide and lanthanum chloride) and characterized using TGA and DSC techniques, as well as mixed dehydration/hydration tests in the oven and climatic chamber.

Chapter 4 reports the work performed on the development of composite materials. The effect of the addition of polymeric binders in graphene/salt composites is evaluated. The characterization performed include the study of energy storage density, thermal conductivity and reaction kinetics. Two different routes for the fabrication of composites are compared, namely wet impregnation and freeze-drying. Part of the work described in this chapter has been previously published in:

Chapter 5 comprehends the studies related to thermochemical reactors. Different setup concepts were designed, assembled and tested. In particular, two systems were used for a comprehensive test of the properties of TCMs in the larger scale. An open reactor in which composite materials are included in form of tabs and air is used as a heat and mass transfer medium. A closed system encompassing an internal airflow to force the movement of water to and from the salt hydrate bed. This last reactor was also modeled using thermofluid dynamics approach in order to understand its functioning. Part of the work described in this chapter has been previously published in:

Chapter 6 reports the general conclusions and future perspectives.

Chapter 2

Materials and Methods

2.1 Materials

Strontium Bromide Hexahydrate (SBH), $SrBr_2 \cdot 6H_2O$, was purchased from Alfa Aesar®. It presents a purity >95% and a bulk density of 2.386 g/cm^3, as reported in the material datasheet. Lanthanum Chloride Heptahydrate, $LaCl_3 \cdot 7H_2O$ was purchased from VWR Chemicals with a purity >98% and a bulk density of 3.84 g/cm^3. Magnesium Sulfate Heptahydrate, $MgSO_4 \cdot 7H_2O$, was purchased from Merck® with a purity >98% and a bulk density of 1.68 g/cm^3.

Expanded Graphite (G) was supplied by TIMCAL (CH), commercial grade TIMREX® BNB90. The producer reports a bulk density of 0.0300 g/cm^3, a particle size of 85 μm and a specific surface area of 28.4 m^2/g. Graphene (g) is provided by Avanzare and obtained by oxidation and thermal reduction of natural graphite. It presents a surface area of 196 m^2/g, I_D/I_G=1.3 and 2% O evaluated from X-Ray Photoemission Spectroscopy. The flakes possess a typical lateral size of few microns and a thickness of few nanometers.

Poly diallyldimethylammonium chloride (PDAC) 20% wt/wt water solution with an average molecular weight of 400,000–500,000 g/mol was purchased from Merck®. Sodium carboxymethyl cellulose (CMC) with an average molecular weight of 250000 g/mol and a degree of substitution of 0.7 was purchased from Merck®. Cellulose NanoFibers (CNF) 1.5 % wt/wt water suspension was prepared with mechanical machining and an enzymathic treatment [139,140] of cellulose. When dried the fibers present a diameter of 3-15 nm and a length 0.7-3 nm. Polyacrylic acid (PAA) purchased from Merck® as 35% wt/wt water solution presents an average molecular weight of 100.000 g/mol declared by the producer.

Water used for the preparation of the suspensions is supplied by a Direct-Q® 3 UV Millipore System. Vermiculite pellets with a diameter of 2-3 mm and a powder density of 0.1 g/cm^3 used in the open reactor were shipped by Merck®. Sodium

acetate trihydrate (SAH) and lithium acetate dihydrate (LAH) were purchased from Merck®. Mobiltherm 605 thermal oil provided by EXXON MOBIL was used in the sodium acetate system.

2.2   Composites preparation methods

The main steps of the preparation procedure of the composites are reported in Figure 24. At first, the graphitic materials are dispersed in water in a becher, using magnetic stirring for graphite and an ultrasonication probe (Sonics Vibracell VCX-750, Sonics & Materials Inc.) with a 30 s pulse at 150 W for 30 min for graphene. After that, a water solution/dispersion of the selected binder was added in the becher. PAA, PDAC and CNF were used as received, CMC was dissolved in water with magnetic stirring for 1 h. Eventually, SBH was added in the dispersion and it was left in agitation overnight to assure a complete homogenization of the system.
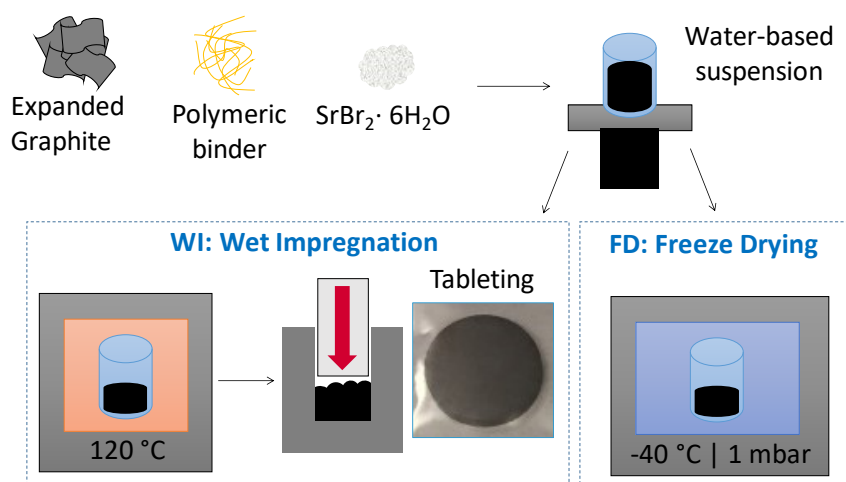
Figure 24. Composite materials preparation methodologies.

Two different techniques were used to obtain the final composites: Wet Impregnation (WI) and Freeze Drying (FD). In WI, water was removed with a heater placed under the becher at 100°C under continuous magnetic stirring. When the dispersion viscosity was too high to allow any further stirring, the wet material was placed in a vacuum oven at 25 mbar and 50 °C overnight to complete the process. After that, the samples were tableted using a stainless steel mold in a hydraulic press under the pressure of 1 t. The nominal tab size was 30 mm in diameter. In FD, the dispersions were frozen in an ethanol bath at -80°C and placed in a Pascal LIO-5P 4K freeze-dryer for 5 days at -40 °C and ~1 mbar (Figure 24).

The compositions of prepared composites and the codes employed in this thesis to denote them are listed in Table 7. To set standard conditions before doing any measurement, the materials were completely dehydrated in oven at 120°C and hydrated in a climatic chamber at 23.0±0.1 C and 50.0±0.1% RH.

Table 7. List of the prepared composite materials. The values are weight ratios between the components.

Sample	SBH	G	E	Binder	Binder type	Preparation
SBH	1	0	0	0	None	None
SBH_G	5	1	0	0	None	WI
SBH_G_PDAC(0.1)	5	1	0	0.1	PDAC	WI
SBH_G_PDAC(0.5)	5	1	0	0.5	PDAC	WI
SBH_G_PDAC(1)	5	1	0	1	PDAC	WI
SBH_G_CMC	5	1	0	0.5	CMC	WI
SBH_g/G_CMC	5	0.7	0.3	0.5	CMC	WI
SBH_g_CMC	5	0	1	0.5	CMC	WI
SBH_G_PAA	5	1	0	1	PAA	WI
SBH_G_CNF	5	1	0	1	CNF	WI
SBH_G_CNF_FD	5	1	0	1	CNF	FD
SBH_G_PDAC_FD	5	1	0	1	PDAC	FD

2.3 Materials characterization

Dry Thermogravimetric Analysis (TGA)

Dry TGA dehydration tests were carried out with a Discovery TGA by TA Instruments. The samples were analyzed in powder form and weighted on a Radwag AS220.R2 analytical balance, presenting a mass in the range 7.0±0.5 mg. The powders, stored in a controlled environment at 23.0±0.1 C and 50.0±0.1% RH, were placed in open platinum pans and directly loaded in the TGA, minimizing the material exposure time to the laboratory environment. To control the sample environment, gaseous nitrogen with a humidity of ~0% RH is flown in the TGA furnace at 100 ml/min. A heating rate of 10 °C/min was selected in the analyses. Two analysis programs were chosen to characterize the salt hydrates. In the first, a temperature ramp from 35°C to 250°C was used to study the dehydration behavior of the salt hydrates. In the second program, a ramp from 35°C to 90°C followed by a 90 min isotherm at 90°C was employed to study the performance of the materials simulating a low temperature heat source. This temperature was chosen accordingly to common heat sources for thermal storage, as shown in chapter 1 (Table 3).

Dry Differential Scanning Calorimetry (DSC)

DSC dehydration tests were carried out with a Q20 by TA Instruments in open aluminum pans. Samples preparation procedure and temperature programs for the characterization of salt hydrates were kept equal to dry TGA tests, in order to compare the output data from the two instruments. The only differences between the two experiments was in the nitrogen flow rate, set at 50 ml/min for DSC due to requirements of the experimental setup, and the pans, made of aluminum for DSC tests.

DSC analyses on sodium acetate trihydrate and lithium acetate dihydrate were carried out with three cycles: a heating ramp from -30°C to 100°C, a cooling ramp from 100°C to -30°C and a third ramp from -30°C to 100°C.

Hydration/Dehydration cycles of pure salts were performed in DSC Q20 using the already described 90°C isotherm program. After each analysis, the samples were left in the open pans and placed in controlled conditions (23.0±0.1 C and 50.0±0.1% RH) to allow rehydration. The DSC measurement was repeated with the same conditions and the change in enthalpy over hydration time was evaluated.

The experimental values of energy storage densities E_d were calculated using a state of the art procedure [109]. The net heat flow $\dot{Q}$ was calculated with equation (6) by subtracting the baseline value BL from the recorded DSC(t) signal. BL was also obtained from the DSC signal by considering the plateau value at the end of each test, related to the sensible heat alone provided to the dry salt hydrate.

$$\dot{Q} = DSC(t) - BL \qquad (6)$$

The experimental enthalpy of reaction ΔH_r is calculated using equation (7) by integrating the heat flow between the starting and ending times of the experiment, noted as t_1 and t_2 respectively.

$$\Delta H_r = \int_{t_1}^{t_2} \dot{Q}\, dt \qquad (7)$$

The experimental energy storage density values E_d are obtained with equation (8) as the ratio of ΔH_r and the sample mass m.

$$E_d = \frac{\Delta H_r}{m} \qquad (8)$$

An experimental error of ±50 J/g was estimated by repeated samples measurements.

Humid coupled DSC and TGA tests

A Netzsch STA 449 F3 TGA/DSC was employed to characterize the hydration kinetics of the composite salt hydrates with complete dehydration/hydration cycles. The instrument was coupled with a ProUmid MHG Modular Humidity Generator, in order to provide a gas flow with controlled humidity during the tests, thus allowing the analysis of both dehydration and hydration phases. Two dehydration/hydration cycles of the materials were realized. In each cycle, the material was dehydrated with a 90 °C isotherm, similarly to the dry tests settings. . After that, temperature is lowered to 25°C in dry conditions to avoid material hydration with unstable temperature. The cycle is repeated twice. The first cycle is used to set known initial conditions, the second one to characterize the material. The steps of the temperature/humidity program used are listed in Table 8.

Table 8. Temperature/humidity program for the dehydration/hydration tests.

Cycle	Segment	Program	Process	Water vapor pressure (Pa)
I	1	Ramp: 27-90°C|10°C/min	Dehydration	1500
	2	Isotherm: 90°C|60min	Dehydration	1500
	3	Ramp: 90-25°C|2°C/min	Equilibration	70
	4	Isotherm: 25°C|40min	Equilibration	70
	5	Isotherm: 25°C|360min	Hydration	1500
II	6	Ramp: 27-90°C|10°C/min	Dehydration	1500
	7	Isotherm: 90°C|60min	Dehydration	1500
	8	Ramp: 90-25°C|2°C/min	Equilibration	70
	9	Isotherm: 25°C|40min	Equilibration	70
	10	Isotherm: 25°C|360min	Hydration	1500

In order to compare results from different samples, a normalized weight for sorbed water $m_{w,n}$ was calculated with the following procedure.

Water weight m_w is obtained with equation (9) by subtracting the mass of the dry sample m_{dry}, which is the recorded mass sample at the end of segment 7, from the recorded mass sample m.

$$m_w(t) = m(t) - m_{dry} \qquad (9)$$

Equation (10) was then used to calculated $m_{w,n}$, normalizing m_w over m_{dry}.

$$m_{w,n}(t) = \frac{m_w(t)}{m_{dry}} \qquad (10)$$

Thermal conductivity: Transient Plate Source (TPS) Method

Thermal conductivity tests were carried out on cylindrical tabs with dimensions of 30 mm in diameter and 3 mm in height. TPS 2500S by Hot Disk AB (S) was used with a 6.4 mm radius Kapton sensor. Because of the small height of the samples, the slab method was employed [141]. Specimens were stored at 23.0±0.1 C and 50.0±0.1% RH for more than 48 h before each test, to allow full hydration. During the measurements, the samples were kept at a constant temperature of 23.00±0.01 °C with a Haake A40 silicon oil bath.

Scanning Electron Microscopy (SEM)

The materials morphology was investigated with a Zeiss LEO-1450VP SEM morphology with a 15 kV accelerating voltage. The samples were gold-coated before each experiment. The cross section images were obtained after fragile fracture of the prepared tabs at room temperature.

X-Ray Diffraction (XRD)

A Philips/Panalytical X′Pert Pro using a Philips PW3040/60 X-ray generator with a Cu anode was used to carry out XRD analyses using a Kα wavelength. The settings used were a 2θ angle range of 10–70 with a 0.026° scan step (nominal time

per step of 100 s) with a scanning PixCell 1d detector. The intensity of all reported SBH diffractograms is normalized on SBH (110) peak.

Hydration kinetics evaluation on tabs

To study the hydration of the prepared tabs, they were dehydrated in an oven at 120°C until a constant weight was reached and then hydrated in a climatic chamber (Binder KBF 240, D) at 23.0±0.1 °C, and 50.0±0.1% RH. The weight increase due to water sorption was recorded with an accuracy of 0.5 mg by a Radwag AS 220.R2 analytical balance. The water weight increase m_w as function of time is reported as normalized over the weight of the dry sample, using equations (9) and (10) with the same procedure applied for humid TGA/DSC tests. The only difference is that m_{dry} is set as the sample weight measured after dehydration in the climatic chamber. With repeated hydration tests a 10% error on the mass measurement was evaluated.

2.4   Thermofluid dynamics systems modelling

The model of the closed thermochemical reactor was realized with the software COMSOL® Multiphysics 5.4 using the modules Heat Transfer, Computational Fluid Dynamics and Chemical Reaction Engineering. The main equations used for the modeling are reported below. Bolded and unbolded characters represent vector and scalar quantities respectively.

Three main domains were defined in the model geometry to represent the thermochemical process: flow, evaporator and condenser. The flow domain is composed of humid air enclosed in a geometry that represents the real reactor. The model is set to calculate flow, mass and heat transport in the domain. Water vapor transport in air is defined by equation (11).

$$\frac{\partial [H_2O]_{vap}}{\partial t} + \nabla \cdot \boldsymbol{J}_w + \boldsymbol{u} \cdot \nabla [H_2O]_{vap} = R_w \tag{11}$$

Here $[H_2O]_{vap}$ is the water vapor concentration, $\boldsymbol{u}$ is the flow velocity and R_w is the rate of water production or consumption. The diffusion flux of water in air $\boldsymbol{J}_w$ is defined according to Fick's first law (equation 12), where D_w is the diffusivity of water vapor in air.

$$\boldsymbol{J_w} = -D_w \nabla [H_2O]_{vap} \tag{12}$$

Heat transfer in fluids is modeled using equation (13).

$$\rho C_{p,air} \frac{\partial T}{\partial t} + \rho C_{p,air} \boldsymbol{u} \cdot \nabla T + \nabla \cdot \boldsymbol{q} = Q_s \tag{13}$$

Here ρ is the density, C_{air} is the heat capacity of air, T is the temperature, Q_s is the heat source or sink and k is the thermal conductivity of air and $\boldsymbol{q}$ is the heat flux defined by Fourier's law (equation (4)).

Flow was modeled in the laminar regime using Navier-Stokes equation (14), where **K** represents the viscous forces and **g** is the gravity acceleration, and the continuity equation (15).

$$\rho(\frac{\partial \boldsymbol{u}}{\partial t} + \boldsymbol{u} \cdot \nabla \boldsymbol{u}) = \boldsymbol{K} + \rho \boldsymbol{g} \tag{14}$$

$$\frac{\partial \rho}{\partial t} + \nabla \cdot (\rho \boldsymbol{u}) = 0 \tag{15}$$

Both evaporator and condenser domains are represented as two separate reactant surfaces. In particular, water desorption from the evaporator surface represents the TCM bed dehydration, while water adsorption on the condenser surface represent condensation.

Two chemical equations are defined to describe the dehydration reaction c and the condensation d.

$$H_2O_{cry} \rightarrow H_2O_{vap} \tag{c}$$

$$H_2O_{vap} \rightarrow H_2O_{liq} \tag{d}$$

Where H_2O_{cry} is the water of crystallization in the salt hydrate, H_2O_{vap} is water vapor in the environment and H_2O_{liq} is liquid water condensed at the bottom of the conical flask.

Two reaction rate values r_1 and r_2 are defined for reactions c and d respectively, each related to an equilibrium constant (defined as k_1 and k_2) as explained in equations (16) and (17). Here $[H_2O_{vap}]$ is the volumetric molar concentration of water vapor in air.

$$r_1 = k_1 [H_2O]_{vap} \tag{16}$$

$$r_2 = k_2 (\frac{1}{[H_2O]_{vap}}) \tag{17}$$

A boundary condition is imposed between the flow domain and the reactant surfaces by setting the reaction rate term R_w in water vapor transport equation (11) equal to the evaporation or condensation reaction rate. In particular, conditions $R_w = r_1$ and $R_w = r_2$ are applied in the regions near the evaporator and condensation surfaces, respectively. These conditions represent $[H_2O]_{vap}$ increase near the salt hydrate bed due to the dehydration reaction and decreases in the condenser due to condensation.

Chapter 3

Materials screening and selection

3.1 Salt hydrates

The first step in the design of a thermochemical composite is the selection of the active material that in this case is a salt hydrate. As described in chapter 1 a broad variety of compounds was considered in literature reviews. For the studies performed in this thesis, we decided to focus on materials that are suitable for heat storage applications between 10 °C and 100 °C and are already available on the market to avoid an excessive increase of the costs. A recent review by N'Tsoukpoe et al. [58] evaluated the salts available for thermochemical storage applications on the basis of multiple parameters such as: cost, availability, health and environmental safety, high energy storage density and complete reversibility of the hydration/dehydration reactions. In the referenced work, after a multi-step screening process, three salt hydrates are identified: strontium bromide hexahydrate ($SrBr_2 \cdot 6H_2O$), lanthanum chloride heptahydrate ($LaCl_3 \cdot 7H_2O$) and magnesium sulfate hexahydrate ($MgSO_4 \cdot 6H_2O$).

These three salts were selected and analyzed with TGA and DSC techniques to characterize their heat storage properties. Two different temperature programs were used to study the dehydration of salts: a heating ramp and an isotherm. By heating the sample from 25 °C to 250 °C at a heating rate of 10 °C/min (Figure 25a, c) a different dehydration mechanism is found for each salt. In particular, a three step reaction for $LaCl_3 \cdot 7H_2O$ whereas a two step reaction was observed for both $MgSO_4 \cdot 7H_2O$ and $SrBr_2 \cdot 6H_2O$. The identification of the reaction steps is important for salt hydrates application, because it allows identifying the temperature ranges in which a certain hydrate is in equilibrium, and therefore its parameters of operation. These materials are commonly used in applications where charge/

discharge temperatures and water vapor pressures correspond to thermodynamically stable states of the salt, to avoid issues such as partial or inhomogeneous hydration. For example, strontium bromide was investigated for heat storage purposes in two different temperature ranges: below 100 °C, using the equilibrium reaction between $SrBr_2 \cdot 6H_2O$ and $SrBr_2 \cdot 1H_2O$ [134], and between 150 °C and 300 °C with the reaction between $SrBr_2 \cdot H_2O$ and $SrBr_2$ [93].

An isotherm at 90 °C was then employed to represent a low temperature source (i.e. waste heat from a car engine or heat coming from a solar thermal panel), in order to evaluate the storage performance (Figure 25b, d). The dehydration starts immediately at the beginning of the experiment, while the temperature is still increasing from 35°C to 90°C. This is linked to the presence of an anhydrous gas flow with ~0% RH that sets the dehydrated form as the thermodynamically more stable even at low temperatures (as showed by the phase diagram in Figure 16). For example, at a water vapor pressure of 0.5 mbar the salt dehydrates at a temperature of 5 °C. While these analysis programs are not representative of a real case scenario, where RH in the salt bed environment is expected to be greater than 0 %, they can be applied to study the fundamental properties presented in this chapter. The chosen heating rate also affects the measurement (e.g. a high heating rate may lead to salt melting, possibly causing recrystallization and changes in the materials morphology). The used value of 10 °C/min was found suitable for the identification of salt hydrates properties by N'Tsoukpoe et al. [58].
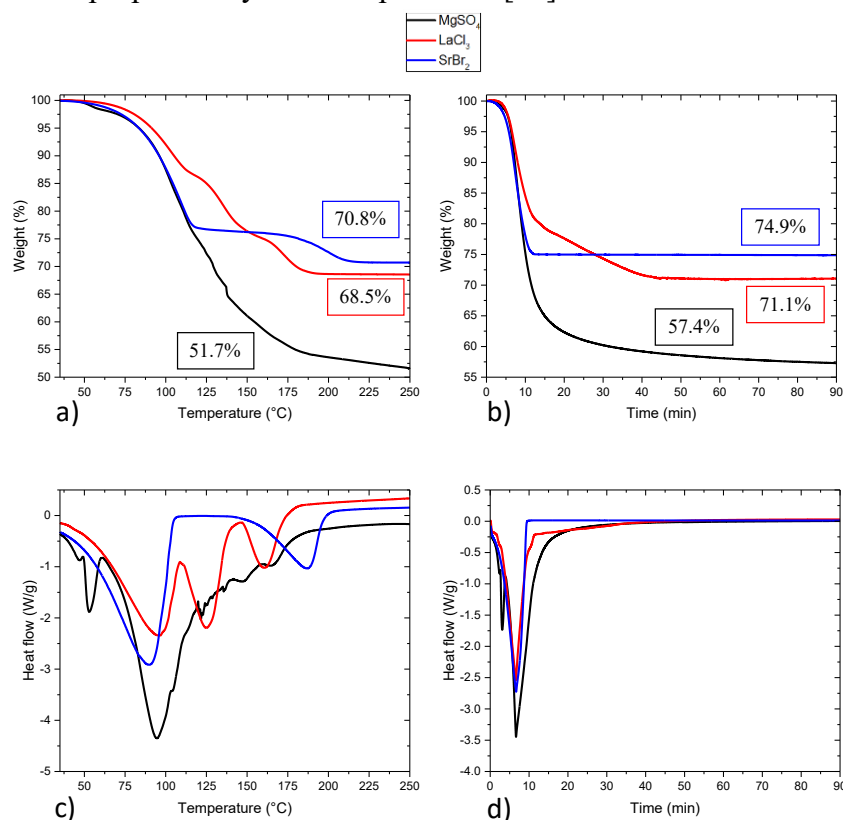

Figure 25. TGA (a, b) and DSC (c, d) curves for the ramp (a, c) and isotherm (b, d) experiments. The values reported in the TGA plots represent the sample weight at the end of the test.

The DSC dehydration peaks were integrated to obtain the experimental energy storage densities (E_d), that are reported in Table 9 in comparison to literature values (E_l). While magnesium sulfate and lanthanum chloride present values close to literature, strontium bromide shows a lower energy storage density than expected. This behavior may be caused by a lower pristine material purity compared to the other salts (95% instead of >98%).

From the weight curves it is possible to evaluate the experimental weight loss w_e. By comparing those values to theoretical weight losses (w_t), it is possible to deduce a dehydration mechanism for the salts. w_t is calculated with equation (18).

$$w_t = \frac{M_{w,desorbed}}{M_{w,hydrate}} \cdot 100 \qquad (18)$$

$M_{w,water}$ and $M_{w,hydrate}$ are the molar weights of the desorbed water and of the salt in its hydrate form, respectively. The results are reported in Table 9. The measured values are in accordance with the theoretical ones with an accuracy of ± 1 %.

Table 9. Dehydration mechanisms and energy storage densities for isotherm experiments.

Reaction	E_d (J/g)	E_l (J/g)	w_e (%)	w_t (%)
$MgSO_4 \cdot 7H_2O \rightarrow MgSO_4 \cdot H_2O + 6H_2O$	1296	1363 [58]	42.7	42.6
$LaCl_3 \cdot 7H_2O \rightarrow LaCl_3 \cdot H_2O + 6H_2O$	939	958 [58]	29.0	28.0
$SrBr_2 \cdot 6H_2O \rightarrow SrBr_2 \cdot H_2O + 5H_2O$	707	846 [55] 948 [58]	25.2	24.3

Different dehydration rates can also be evaluated from the curves. While magnesium sulfate reaches its fully dehydrated state after ~80 min, lanthanum chloride takes ~45 min and strontium bromide shows the fastest rate, since it is dehydrated in ~10 min. All the curves show a fast dehydration behavior in the first 10 min of experiment. After this time, strontium bromide is fully dehydrated, while water desorption continues in lanthanum chloride and magnesium sulfate with a slower rate, probably due to a multi-step dehydration mechanism. Since dehydration time of magnesium sulfate is too high in comparison to the other two salts, it is not considered in further characterizations. To evaluate the hydration kinetics, the dehydrated salts were exposed to a constant humidity and temperature environment (50% RH and 23 °C) for different times (i.e. 0.5 h, 15 h, 25 h and 48 h) and then tested by DSC, using the already described program constituted by isothermal heating at 90 °C. Figure 26 reports the value of the integral of the dehydration peaks as a function of the hydration time. The full hydration lines show the measured values for energy storage density of the salts as received. Strontium bromide shows fast hydration kinetics, achieving complete rehydration even with

short exposure times (0.5 h) and remaining stable, within experimental deviation, for longer exposure to the moist environment. On the other hand, LaCl$_3$ reaches its fully hydrated state after more than 15 h of moisture exposure and shows tendency of deliquescence, probably due to partial over-hydration of the salt. Strontium bromide was therefore selected to be further characterized.
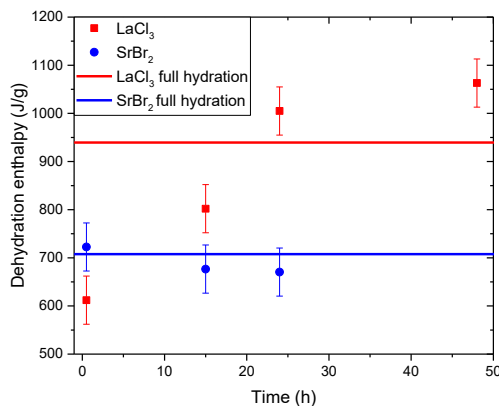
Figure 26. Results of the hydration/dehydration cycles experiments with DSC.

As the dehydration kinetics is expected to depend on both the mass and the geometrical constraints, a second dehydration test was carried out on 10 g of (as received) strontium bromide by heating it at 120 °C in a round bottom glass flask and measuring the weight vs time, reflecting the water desorption. From the measured sample weight during dehydration m(t), conversion α is calculated using equation (19) and plotted in Figure 27.

$$\alpha = \frac{m_s - m(t)}{m_{w,cry}} \tag{19}$$

m_s is the starting mass of the sample (10 g) and $m_{w,cry}$ is the mass of the theoretical crystallization water calculated assuming a completely hydrated starting sample.
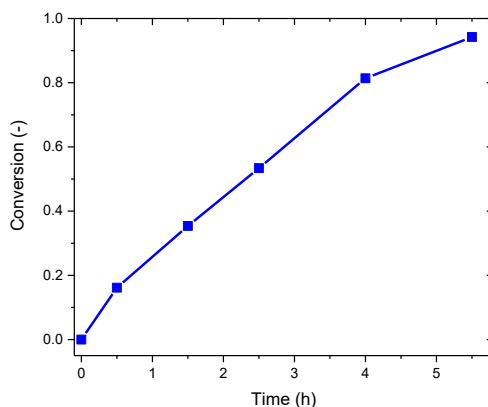
Figure 27. Conversion of the dehydration reaction with 10 g of salt.

Strontium bromide is able to reach the full hydration state after ~6h, showing an approximately linear water sorption. The reduction of sorption rate with an increased sample mass is mainly caused by mass transfer issues (a reduced salt/air surface accessible for the reaction) and heat transfer issues (more sensible heat is needed to reach the desired temperature with an increased thermal mass) [70].

Since hydration/dehydration cycle stability is a critical issue for salt hydrates, as discussed in section 1.5, a cyclability test was performed to further evaluate the applicability of strontium bromide. When the pristine salt is implemented in thermochemical reactors (reviewed in section 1.8), it shows a strong decrease in performance after each cycle. In particular, this effect was evaluated in the system reported by Michel et al. [134], that comprises 200 kg of salt used for 7 cycles at a dehydration temperature of 80 °C and in the reactor by Fopah-Lele et al. [98] that uses 1 kg of salt for 13 cycles at a temperature of 100 °C. On the other hand, the stability of this salt was demonstrated by Richter et al. [93] with TGA analysis on a 15 mg sample over 10 cycles in the temperature range 90-190 °C.

To verify the stability of strontium bromide, 2.5 g of salt were subjected to 50 cycles of dehydration in an oven at 120 °C and rehydration in a climatic chamber at 23 °C and 50% RH. The results are shown in Figure 28, where the sample weights are plotted as a function of the cycle number. The theoretical hydrated weight (blue line) corresponds to the weight of the sample as purchased, while the theoretical dehydrated weight is calculated by diminishing the hydrated weight by the mass loss for a full salt dehydration (25.1%), experimentally evaluated with TGA and shown in Figure 25. After some oscillations in the first 10 cycles, the weight difference is stable until cycle 50. The change in hydration/dehydration behavior was already studied for salt hydrates evidencing the formation of cracks after the first hydration/dehydration cycles, caused by the mass transfer of water in the salt [92].
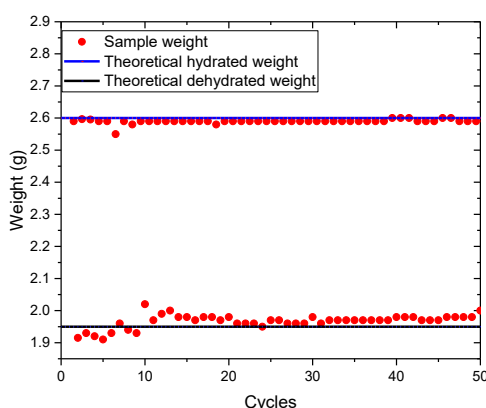
Figure 28. Sample weight for cyclability test.

Cyclability in the salt hydrate is therefore sufficiently stable to allow its usage as TCM. The aforementioned issues in reactor performance are probably related to the usage of large quantities of pristine salt that causes major morphological changes such as salt grains aggregation.

To conclude, while all the considered materials are suitable for thermochemical energy storage, strontium bromide hexahydrate was selected because of its fastest hydration/dehydration kinetics with respect to lanthanum chloride heptahydrate and magnesium sulfate hexahydrate.

3.2 Supercooling salts

In addition to thermochemical energy storage, supercooling acetate salts were preliminary tested as an alternative to TCMs for long-term storage. Both sodium acetate trihydrate (SAH) and lithium acetate dihydrate (LAH) were considered for this purpose.

These were characterized with a DSC analysis, reported in Figure 29. An endothermic peak is observed in the first heating cycle due to the salt melting and no other signals are present in the subsequent cooling and heating cycles. This effect can be attributed to a supercooling of the salts, that remain in the molten state even at -30°C without any crystallization phenomenon [142]. The registered peak for SAH is at 67.69°C and has an enthalpy per unit mass of 260.2 J/g, close to literature data [143]. For LAH the dehydration temperature is 60.04°C and the enthalpy per unit mass is 304.1 J/g.
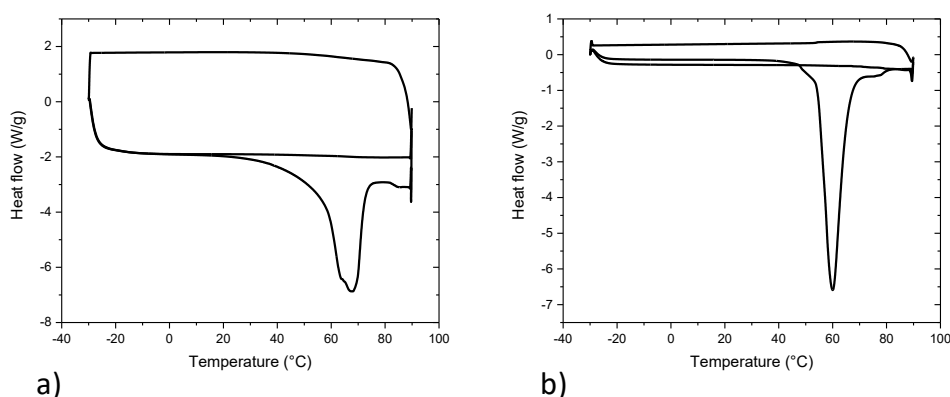
Figure 29. DSC curves for sodium acetate trihydrate (a) and lithium acetate dihydrate (b).

To check whether the supercooling properties of the salts can be scaled up, 5 g of SAH and LAH were put in round bottom glass flasks, closed with a plug and immersed in a silicon oil bath. The bath temperature was raised to 100°C for 1h to allow the melting of the salts and then the system was left cooling at room temperature. While SAH was capable of maintaining a supercooled state, as reported in literature [144], LAH didn't show the same behavior and is therefore considered not suitable as supercooling salt for long term storage.

Eventually, acetate salts present a limited choice of materials and energy density values in the range 250-300 J/g, much lower than TCMs, that present values in the range of 700-1200 J/g [55]. Therefore, it was decided to focus on the applicability of salt hydrates using thermochemical storage processes.

Chapter 4

Organic/inorganic thermochemical composites

Part of the work described in this chapter has been previously published in:

S. Salviati, F. Carosio, G. Saracco, A. Fina, Hydrated Salt / Graphite / Polyelectrolyte Organic-Inorganic Hybrids for Efficient Thermochemical Storage, Nanomaterials. 9 (2019) 420. doi:10.3390/nano9030420

S. Salviati, F. Carosio, F. Cantamessa, L. Medina, L.A. Berglund, G. Saracco, A. Fina, Organic/inorganic composite materials for thermochemical energy storage, in: Proc. Eurotherm Semin. #112 Adv. Therm. Energy Storage, 2019

F. Cantamessa, Materiali compositi per lo stoccaggio termochimico di calore a base di grafite naturale espansa e bromuro di stronzio idrato, 2018, Master Thesis in Materials Engineering, 23/03/2018, Politecnico di Torino.

This chapter presents the results obtained on composite materials encompassing graphite-based matrices, strontium bromide hexahydrate and polymeric binders. Such complex composite structure is designed to obtain a better control and stability of salt organization.

Expanded graphite high porosity can allow the distribution of the salt grains inside its structure, thus enhancing the salt/air interface surface and the contact with environmental water vapor. In addition, as it was described in chapter 1, graphite shows higher thermal conductivity than salt hydrates, possibly allowing for an improvement in heat transfer between the active material and the matrix.

Binders were also included in the composites, selected after a literature screening based on parameters such as chemical affinity with both graphite lamellae

and ionic salts, with the aim to increase the materials stability, and water sorption properties, thus possibly contributing to the thermochemical storage process. The binders selected are polydiallyldimethylammonium chloride (PDAC or polyDADmac) [145,146], polyacrylic acid (PAA) [147], cellulose nanofibers (CNF) [148] and carboxymethyl cellulose (CMC) [149]. Their chemical structures are reported in Figure 30.

PDAC
Polydiallyldimethyl
ammonium chloride

PAA
Polyacrylic acid

CNF
Cellulose nanofibers

CMC
Carboxymethyl cellulose
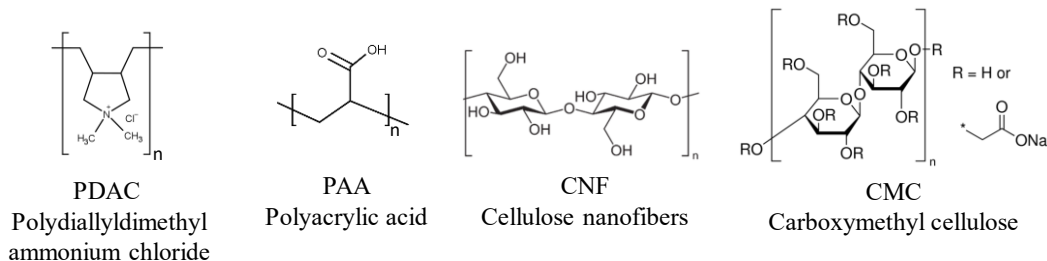
Figure 30. Chemical structure of the binders used in composite materials.

While salt/graphite and salt/polymer composites were already developed in literature (cfr section 1.6), at the best of my knowledge no studies are present on three-components materials. The design of composites with complex architectures is therefore addressed in this chapter as a route to improve the existing TCMs.

4.1 Preliminary studies on binders

SBH/graphite composite materials prepared with WI method already presented in the literature [118,119] as high performance TCMs were selected as starting material to study the effect of polymers inclusion in SIMs. As a preliminary test on the influence of binders in TCM composites, the WI method was used to prepare four composite formulations, listed in Table 10. One sample (SBH_G) was produced as reference material without the inclusion of any binder, while the other three contained PAA, CNF and PDAC.

Table 10. Samples realized for preliminary studies on binders.

Sample	SBH	G	Binder	Binder type	Preparation
SBH_G	5	1	0	None	WI
SBH_G_PDAC	5	1	1	PDAC	WI
SBH_G_PAA	5	1	1	PAA	WI
SBH_G_CNF	5	1	1	CNF	WI

Composites morphology and energy storage density were investigated by SEM and DSC respectively. Figure 31 reports representative SEM micrographs of the different composites.
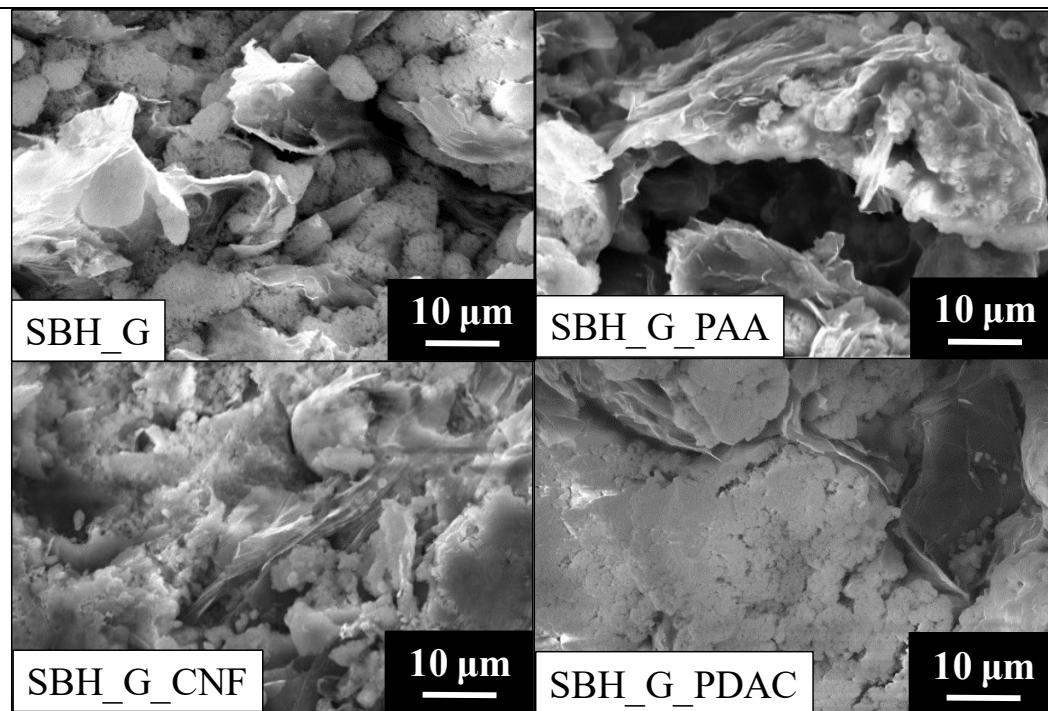
Figure 31. SEM micrographs of the prepared samples.

The top left micrograph shows a picture of SBH_G. The structure is characterized by an inhomogeneous mixture with separate micron-scale domains of salt and graphite. The other micrographs represent samples where the different polymeric binders were included during the preparation process. A better coverage of SBH over graphite lamellae can be generally observed, suggesting an influence of the binders as compatibilizers between salt and graphite. The presence of aggregates of salt crystals is limited, and the smaller crystals appears to be embedded in an organic matrix surrounding G platelets.

Figure 32 shows the dehydration enthalpies calculated from the DSC curves. The blue bars represent the experimental energy storage density (E_d) calculated from DSC plots, while the orange ones show the expected energy storage values ($E_{d,exp}$) of the composites obtained with equation (20).

$$E_{exp} = x_{SBH} \cdot E_{SBH} \qquad (20)$$

Where x_{SBH} is the weight ratio of SBH in the composite and $E_{d,SBH}$ is the measured Energy Storage density for SBH, equal to 714 J/g as reported in chapter 3.
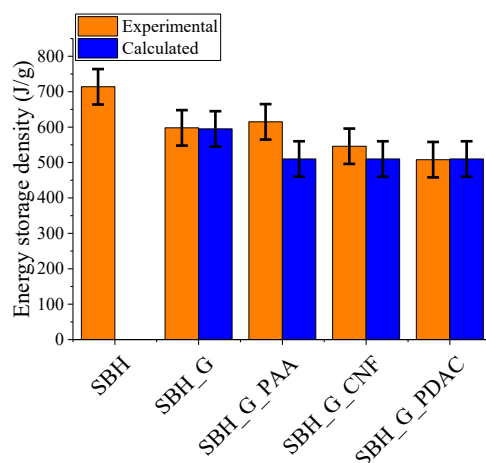
Figure 32. Experimental (orange) and calculated (blue) energy storage density values for the prepared samples.

While SBH_G yields similar experimental and expected values it is possible to notice that the presence of the binders results in higher experimental values, compared to the theoretical values. This phenomenon has been already reported in literature for conventional salt/polymer composites [115] and was explained as a partial deliquescence of the salts stabilized by the polymeric matrix. Deliquescence can lead to higher experimental values due to the presence of phenomena of solubilization of the salt in sorbed water and solution dilution, in addition to the solid/gas reaction used in the thermochemical process[150]. In our case, no evidence of deliquescence was observed neither for the pristine salt, nor for the composite. Therefore this effect can be described as an active contribution of the binders to the sorption process, probably due to polyelectrolyte-water interaction, since the salt was hydrated at the equilibrium conditions for the hexahydrate phase (23°C and 50% RH), as reported on the SBH/water phase diagram [127]. While the usage of polymers has been previously reported as beneficial for the structure stability and water mass transfer, a comparison with the enthalpy values to the pristine salt resulted in a reduction in the energy storage density [70,116] due to the addition of an inert component. In contrast, in this work the use of hygroscopic polyelectrolyte binders is therefore a valuable route for the salt hydrates stabilization, while enhancing their moisture absorbance capability.

To further investigate the effect of the binders on the TCMs structure and performance, it was decided to study the effect of a change in the binder concentration in samples morphology, thermal properties and sorption kinetics. PDAC was selected as binder due to is known water sorption properties that could lead to an active contribution to the thermochemical storage process [146].

4.2   Binder concentration studies

PDAC was selected for this study because of its known water sorption properties and three different formulations were prepared, with a binder/graphite weight ratio of 0.1, 0.5 and 1 respectively, reported in Table 11.

Table 11. Samples prepared for binder concentration studies.

Sample	SBH	G	Binder	Binder type	Preparation
SBH	1	0	0	None	None
SBH_G	5	1	0	None	WI
SBH_G_PDAC(0.1)	5	1	0.1	PDAC	WI
SBH_G_PDAC(0.5)	5	1	0.5	PDAC	WI
SBH_G_PDAC(1)	5	1	1	PDAC	WI

Morphological analysis

As the microstructure of the TCM may affect the kinetic of hydration/dehydration, SEM was employed to investigate the influence of PDAC concentration on the morphology and microstructure of the prepared samples. The micrographs (Figure 33) unveil the effect of PDAC in the salt distribution. In particular, in the absence of PDAC, salt aggregates in globular shapes with dimensions in the order of few μm were observed between flakes of expanded graphite. This was already observed previously when evaluating the effects of the different polyelectrolytes (Figure 31). In the presence of PDAC, the shape of salt aggregation changes as a function of the different polyelectrolyte concentration. Indeed, the average size of globular salt agglomerates was reduced in the sample with a PDAC/G ratio of 0.1 (PDAC content of 2% w/w, Figure 33b), and appears to be completely absent in the samples with ratio 0.5 (PDAC content of 10% w/w of PDAC) and 1 (PDAC content of 18% w/w of PDAC), as shown in Figure 33c, d respectively. It seems that PDAC acted as a binder between salt crystals as well as an adhesion promoter at the salt/graphite interface, as schematized in Figure 33e. Therefore, a variation in binders' concentration implies a variation of the salt hydrates aggregation on the graphitic substrate.
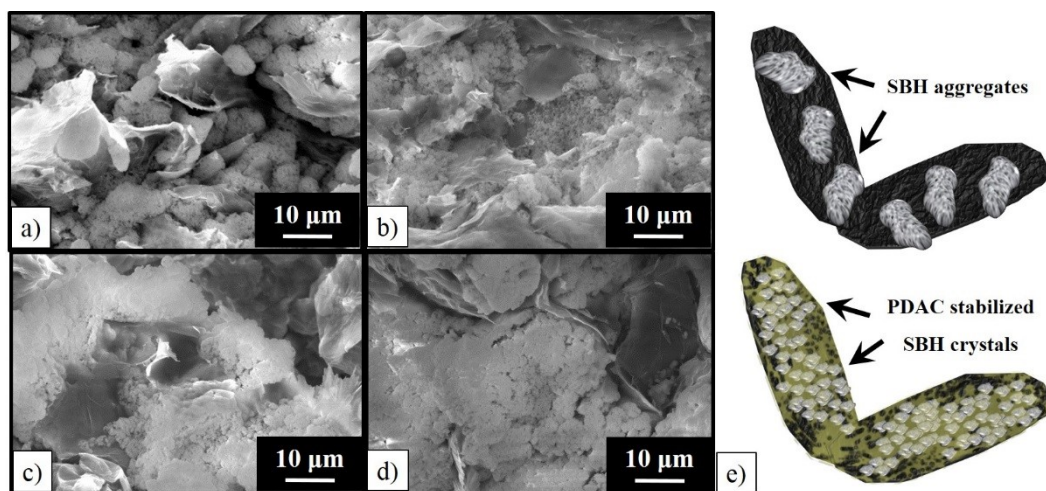
Figure 33. SEM representative images of samples cross sections. (a) SBH_G, (b) SBH_G_PDAC(0.1), (c) SBH_G_PDAC(0.5) (d) SBH_G_PDAC(1). (e) Illustration of the PDAC effect in the SBH_G mixture.

XRD analysis was used to identify the crystal structure of the employed salt; in particular, it was used to investigate possible anion exchange reactions between SBH and the polyelectrolyte during the water dissolution and recrystallization process. The concentration of Cl^- ions provided by PDAC and Br^- ions provided by SBH was calculated based on the weight ratio of the samples presented in Table 11. The weight ratio Cl^-/Br^- and was found to be 0.02, 0.11 and 0.22 for samples SBH_G_PDAC(0.1), SBH_G_PDAC(0.5) and SBH_G_PDAC(1) respectively. Therefore, phenomena of ion exchange between PDAC and SBH leading to the formation of unwanted chemical species (e.g. $SrCl_2$) are possible. The collected diffractograms for purchased SBH and G are reported in Figure 34, while diffraction patterns for SBH_G and the counterparts with different PDAC concentrations are reported in Figure 35.
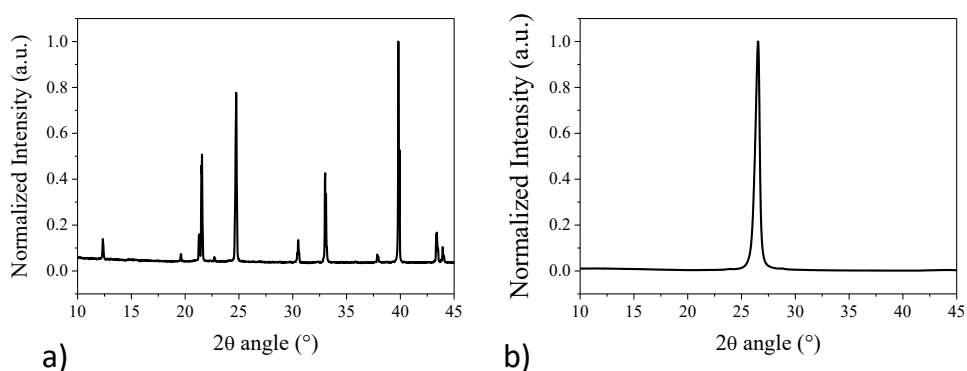
Figure 34. Collected XRD diffractograms for (a) SBH and (b) G
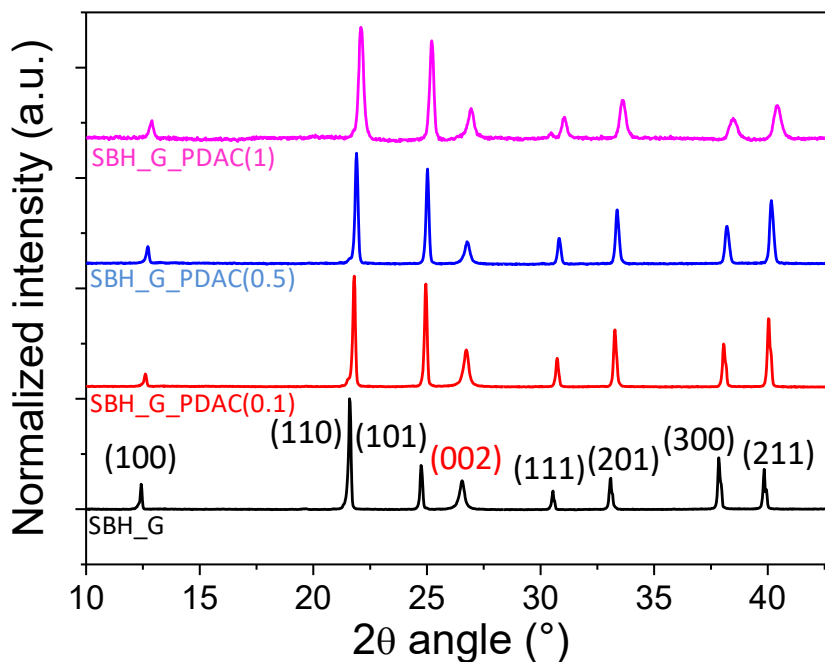
Figure 35. XRD diffractograms of the prepared samples. Miller indices are depicted in black for SBH and in red for graphite crystal planes. Intensity is normalized on the SBH (110) peak.

Using the Joint Committee on Powder Diffraction Standards-International Centre for Diffraction Data database (JCPDS-ICDD) [151], both $SrBr_2 \cdot 6H_2O$ and graphite crystal planes were identified, their Miller indices being reported on the diffractogram in black and red, respectively. The absence of additional peaks excluded the formation of crystalline byproducts derived from ion exchanges between PDAC and SBH during the manufacturing process. Nonetheless, differences in relative intensities of selected peaks (i.e., signals at 24.7 and 39.8) were observable in the diffractogram between samples with and without polyelectrolyte addition. This could be ascribed to the influence of the polyelectrolyte in the growth of salt hydrates crystals, as previously reported in the literature [152]. In addition, a limited broadening of the SBH main peaks was observed at the highest PDAC concentration, supporting for the binder role in the aggregation of SBH crystals. Finally, the absence of extra peaks in PDAC-containing composites confirmed the amorphous nature of the polyelectrolyte.

Thermal analysis

DSC and TGA analyses were first employed to study the dehydration of the composites in dry conditions. The temperature program was chosen to simulate a 90°C heat source charging the thermochemical system, similarly to characterizations shown in chapter 3. DSC results are reported in Figure 36, showing heat flow plots for different samples, characterized by an endothermic peak corresponding to the dehydration reaction.
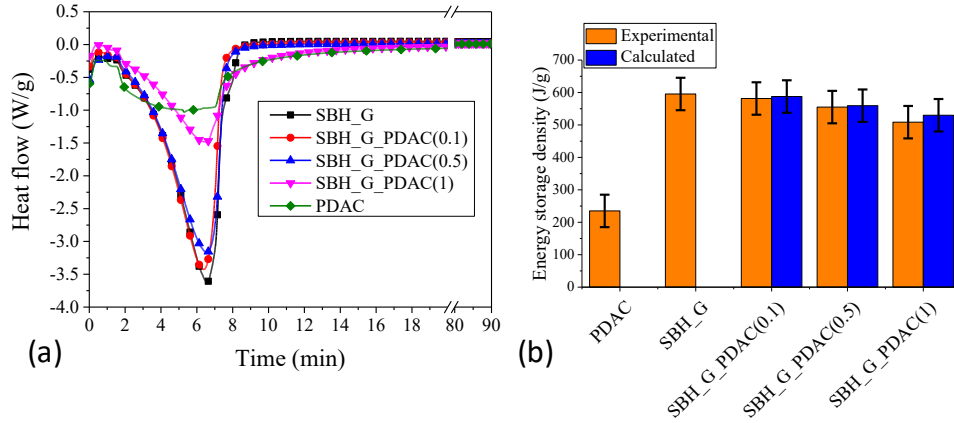
Figure 36. (a) Differential scanning calorimetry (DSC) curves of the prepared samples. (b) Experimental and calculated values for energy storage density.

From DSC plots it is possible to observe that SBH_G and PDAC analysis results in two different curves, both in their shape and offset points (10 min and 18 min respectively), testifying the presence of two different endothermic phenomena. These properties were already identified and studied for salt hydrates and polyelectrolytes separately. Salt hydrates hydration is considered a chemisorption phenomenon, in which water molecules are included in the bulk structure of the material. [73] On the other hand, in polyelectrolytes water molecules are attracted and bound to the ionic charges on the polymeric chains with physisorption [153]. An effect of these two different phenomena was experimentally evidenced by the great difference between the energy storage density values for SBH and PDAC (714 J/g and 235 J/g respectively, as reported in Figure 36b).

In Figure 36a SBH_G_PDAC(0.1) and SBH_G_PDAC(0.5) show a behavior similar to SBH_G, thus implying a small influence of the binder. On the other hand, SBH_G_PDAC(1) curve differs from the other two samples, suggesting a major contribution of PDAC in the sorption process due to its higher concentration.

Figure 36b reports the energy storage density values, calculated from the integral of heat flow plots. For SBH_G_PDAC mixtures, the experimental values were compared with the theoretical values, calculated according with the rule of mixture (Equation (21)), based on the individual components of energy storage density, and their concentration in the mixture.

$$E_c = x_{PDAC}E_{PDAC} + x_{SBH\_G}E_{SBH\_G} \qquad (21)$$

Where E_c is the energy density of the composite materials with SBH, G, and PDAC, E_{PDAC} is the energy density of PDAC, E_{SBH_G} is the energy density of SBH_G and x_{PDAC} and x_{SBH_G} are the weight fractions of PDAC and SBH_G in the final composites, respectively. As reported in Figure 36b, the calculated experimental values fell within the experimental deviation of the expected ones, within this points out that the system acts as an ideal mixture of the two components, with no synergic nor antagonist interaction between PDAC and SBH, in terms of total energy stored. By increasing the content of PDAC, a reduction of the total

energy storage density was obtained, diminishing the overall efficiency of the composite for thermal storage applications by approximately 15% at the highest PDAC concentration. This is ascribed to the previously discussed great difference in energy storage density between PDAC and the SBH

The dehydration of SBH_G_PDAC(x) was also evaluated by TGA measurements allowing for the assessment of the amount and kinetics of water removal upon heating, as a function of the polyelectrolyte concentration (Figure 37).
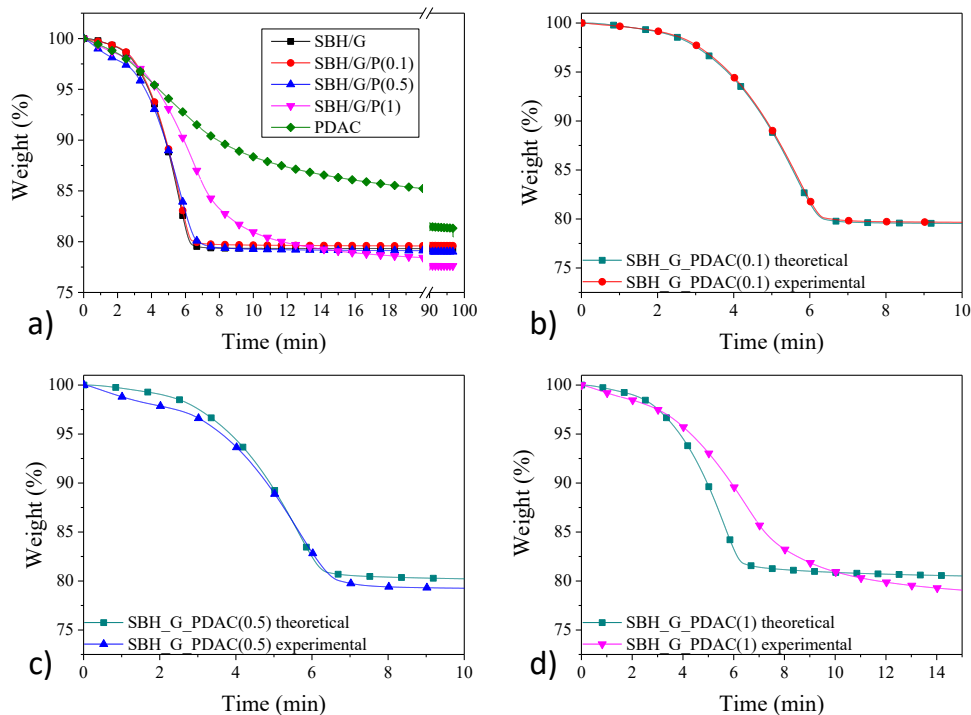
Figure 37. Thermogravimetric analysis (TGA) weight plots of the different SBH_G_PDAC mixtures, compared with pristine PDAC (a), and comparison between experimental end calculated data for SBH_G_PDAC(0.1) (b), SBH_G_PDAC(0.5) (c) SBH_G_PDAC(1) (d).

At low PDAC concentrations (0.1 and 0.5 PDAC/G weight ratios), the polyelectrolyte did not significantly alter the dehydration kinetics with respect to the SBH_G composite. On the other hand, SBH_G_PDAC(1) exhibited a delayed weight loss compared to SBH_G, reflecting the slow dehydration kinetics observed for neat PDAC. To further investigate the effect of PDAC, the theoretical composite weight loss curves (w_c) for the composites were calculated by applying a rule of mixture between the neat PDAC and SBH_G (Equation (22)).

$$w_c(t) = x_{PDAC}w_{PDAC}(t) + x_{SBH}w_{SBH}(t) \tag{22}$$

Where w_p and x_p are the weight and mass fraction of PDAC in the composite, while w_s and x_s are the weight and mass fraction of SBH in the composite, respectively. As reported in Figure 37b, c, the samples with 0.1 or 0.5 weight ratios

showed limited differences between the theoretical and experimental plots, thus suggesting two dehydration processes, from PDAC and SBH, to proceed independently. For SBH_G_PDAC(1), a significant deviation was observed between theoretical and experimental plots, suggesting that kinetics of dehydration were controlled by the interaction between the two phases. This is consistent with the polyelectrolyte binding action between the salt crystals, observed by SEM and ascribed to the delayed diffusion of the water, released by the salt, through the polyelectrolyte. Indeed, while the release of water from crystalline hydrated SBH was simply triggered by the temperature, the amorphous structure of PDAC, with its high free volume, broadened the water release in time, through a series of absorption/desorption steps, eventually reducing the overall dehydration rate. The above results suggest that a high concentration of polyelectrolyte binder can partially reduce the efficiency of the thermochemical system under study by both decreasing the heat storage density (Figure 36b) and slowing down water dehydration kinetics (Figure 37d). Thus, only composites with a PDAC/G weight ratio of 0.1 and 0.5 were selected for further characterizations.

It is known that the surface/volume ratio can strongly influence the heat and mass transfer phenomena in a thermochemical storage system [109]. For this reason, while values collected with dry TGA and DSC analyses may be used to compare the performance of different composites, these are not directly representative of a real application, both in terms of diffusion effects and ambient moisture. For these reasons, composite tabs were fabricated with a cylindrical shape, in order to obtain a modular component scalable to dimensions suitable for real applications.

The thermal conductivity of prepared composite tabs was also evaluated, as heat exchange is obviously crucial for the efficiency of heat storage devices. Results reported in Figure 38 show that the thermal conductivity of the prepared composites remained constant within the experimental error, in the 16–16.5 W/mK range, demonstrating no detrimental effects related to the presence of the polyelectrolyte. Furthermore, thermal conductivity values obtained in this work were significantly higher than previously reported values for similar graphite SBH composites [118]. In particular, Zhao et al. [119] found that in SBH/G composites, an increase in density leads to a higher thermal conductivity, because of a reduction of the air fraction, reaching values up to 8 W/mK with a density of 0.812 g/cm^3. The high values of thermal conductivity of the tabs fabricated in this work are mainly related to their high density, measured in the range 2.6±0.1 g/cm^3.
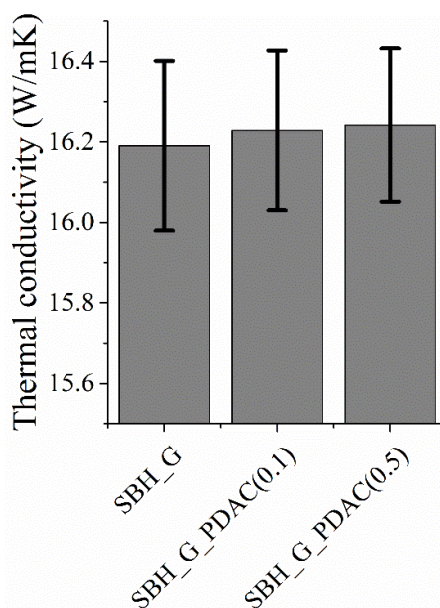
Figure 38. Collected data on thermal conductivity.

Sorption kinetics

Hydration kinetics have been also evaluated in a climatic chamber on the composites. Hydration curves, calculated as the measured weight gain normalized over the weight of the dry tabs, are reported in Figure 39a. The mass vs time plots clearly show a monotonic weight gain for both SBH/G and counterparts including PDAC. However, dramatic differences in moisture absorption kinetics were observed as a function of PDAC concentration. Indeed, while limited differences existed between SBH_G_PDAC(0.1) and SBH_G, the hydration rate of SBH_G_PDAC(0.5) was much higher, especially within the first hours of the test, reaching the full hydration of both phases in the mixture (equivalent to 0.26 $g_{water}/g_{mixture}$ calculated on the basis of Equation (22)) within approximately 10 h, whereas hydration of the other samples was still ongoing after 45 h (Figure 39a). To elucidate the hydration phenomena in the composite, both absorption from PDAC and SBH were quantified independently after full drying followed by exposure to 23°C and 50% R.H. After exposure the dehydration enthalpy was measured in DSC as reported in Figure 36a. Results clearly showed that PDAC has lower dehydration enthalpy compared to SBH and the dehydration enthalpy for the mixture SBH/PDAC follows a rule of mixture (Figure 36b). Clearly different mechanisms (crystal vs amorphous hydration) control the absorption by the two phases and the kinetics of the two processes is expected to be different. Indeed, when analyzing the TGA plots, it is apparent that the presence of PDAC (at high concentration) slows down the whole dehydration process. During hydration of composite tabs, the amount of water absorbed by PDAC is limited by its low concentration (1:10 PDAC:salt) as well as by its lower ability (with respect to SBH) to absorb water as demonstrated by TGA (Figure 37a). Overall, the contribution in total water mass absorption by PDAC during tabs hydration is evaluated to be lower than 10%. Therefore, the main contribution to mass increase during the test is

related to SBH hydration. The SBH_G_PDAC(0.5) curve plateau reported in Figure 39a corresponds to the theoretical water uptake value calculated according to the rule of mixture. Therefore, it appears that the role of PDAC is linked to the kinetics of hydration rather than its thermodynamics.
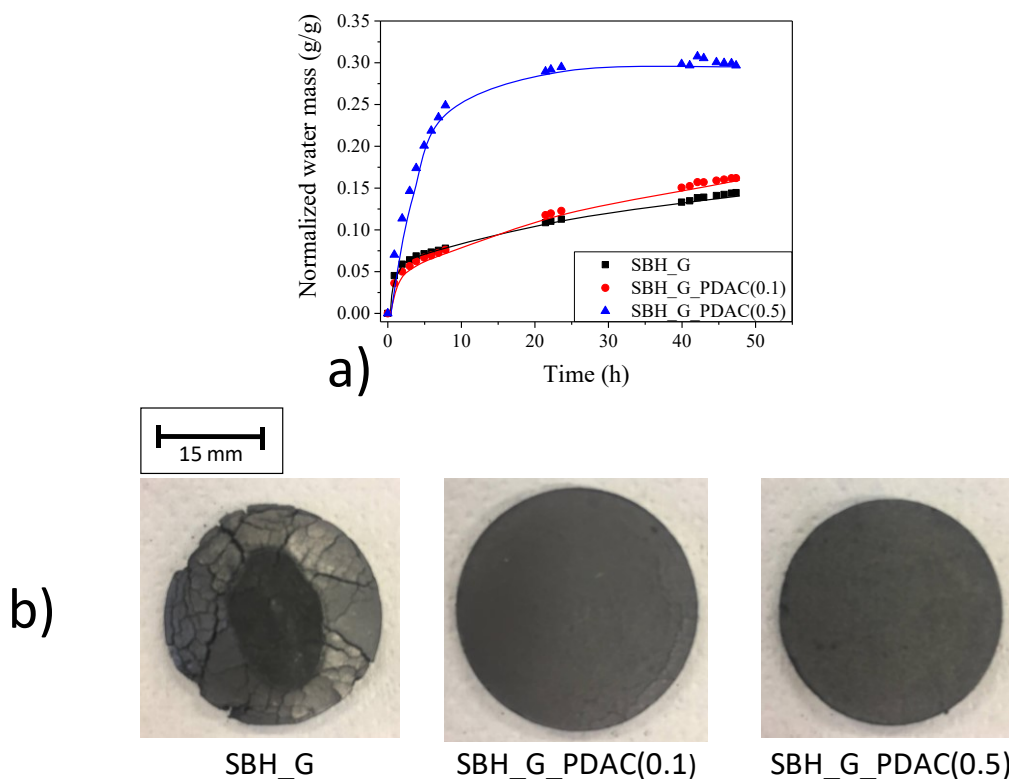
Figure 39. (a) Hydration test on composites tabs; (b) pictures of the tabs after one dehydration/hydration cycle.

Another important aspect to evaluate when considering a real application was represented by the durability of the prepared composite. This had a potentially strong impact on the effectiveness and practicability of the thermochemical storage solution. Furthermore we observed severe damage in the form of cracks to the SBH_G tabs immediately after the first hydration/dehydration cycle (Figure 39b), thus proving this aspect to be a serious drawback of the graphite/salt hydrate composite approach. The mechanical stress in the samples may have been caused by the volume change of the salt during the hydration process. In fact, it is reported that the density of SBH changes between 3.5 g/cm^3 and 2.4 g/cm^3 from hexahydrate to monohydrate form [154]. On the other hand, the presence of a polymeric binder appeared to strongly reduce crack formation at a polymer/G ratio of 0.1, and completely prevent it a 0.5 ratio, thus maintaining the structural integrity of the composites.

As clearly depicted by the characterizations reported, the composite with a PDAC/G ratio of 0.5 was capable of achieving superior water adsorption kinetics while maintaining high thermal conductivity values thus proving that the inclusion of a polymer binder was a successful strategy for the design of an efficient thermochemical storage solution.

Since the properties of a composite TCM were found as deeply dependent on its structure, additional designs were tested in order to improve the sorption kinetics of the materials. In particular, the effect of a higher matrix porosity was evaluated in section 4.3, using the freeze-drying method for samples preparation and in section 4.4 by using graphene instead of expanded graphite.

4.3 Freeze-drying

As detailed in Chapter 1, the most widely applied technique to produce TCM composites is Wet Impregnation (WI), by which a water based solution or dispersion of the components (matrix, salt hydrate and possible additional binders) is heated to remove water, leading to the formation of the TCM composite powder or film. This procedure may grant a good and homogeneous dispersion of the employed components but provides limited control over the structure. Another well-known method for processing water-based solution/suspension into composite materials is the Freeze-Drying (FD) technique [155]. During freezing of the solution/suspension, ice crystals grow and confine the solubilized/suspended components into interstitial solid-rich regions. The templating ice is then removed by sublimation, resulting in highly porous foams [155]. The structure obtained is a function of the employed ingredients and their concentration: in non-optimal conditions, the resulting structure may not possess enough mechanical properties upon ice removal and collapse. Cellulose nanofibrils (CNF) have been widely employed as a green and sustainable structural material in the preparation of lightweight and highly resistant foams [156]. Nano-cellulose is considered as one of the most promising nature-based building block for the production of high performing renewable materials [157]. CNFs can be conveniently extracted from wood-based cellulosic fibers yielding swirled fibrils with typical dimensions of 4-10 nm in diameter and few microns in length. The high aspect ratio and the strong fibril-fibril interactions allow CNF to produce self-sustained and mechanically strong foams during FD processes.

While the use of CNF for the production of structural foams is widely investigated, to the best of my knowledge, there are no studies employing CNF as structural component for TCM composite foams. To this aim, in this work the use of FD for the production of CNF/G/SBH composite materials is investigated, aiming at a better control and stability of salt organization, maximizing the area of the air/salt and salt/graphite interfaces and eventually enhancing mass and heat transfer. PDAC was tested and compared with CNF, using the same preparation routes, because of its already described performance in mechanical stabilization and sorption rate improvement in TCMs. The following formulations were prepared for comparison (Table 12). In sample SBH_G_PDAC a binder/salt ratio of 1 was selected to provide a high polymer concentration, needed for the formation of a templating structure in FD technique, despite its low performance described in chapter 4.2.

Table 12. Samples prepared for freeze-drying studies.

Sample	SBH	G	Binder	Binder type	Preparation
SBH	1	0	0	None	None
SBH_G	5	1	0	None	WI
SBH_G_PDAC	5	1	1	PDAC	WI
SBH_G_PDAC_FD	5	1	1	PDAC	FD
SBH_G_CNF	5	1	1	NFC	WI
SBH_G_CNF_FD	5	1	1	NFC	FD

The morphology of prepared composites was investigated by means of SEM (Figure 40). Morphology for SBH_G_PDAC_FD (Figure 40a, b and c) is characterized by a compact mixture of salt, graphite and polymer, similarly to the sample produced with the WI technique (Figure 40b). Weak interactions between PDAC, graphite and salt hydrates caused the formation of a fragile structure that collapsed during ice sublimation. On the other hand, the micrographs for SBH_G_CNF_FD (Figure 40d, e and f) highlight a high porosity and preferentially oriented pores, which are typical for FD processed foams [157]. The SBH_G_CNF_FD cellular structure is characterized by open channels, resulting from growing ice crystals, in the range of 100 μm. High magnification micrographs reveal the structure of the cell walls where salt crystals are embedded in a G/CNF matrix (Figure 40f).
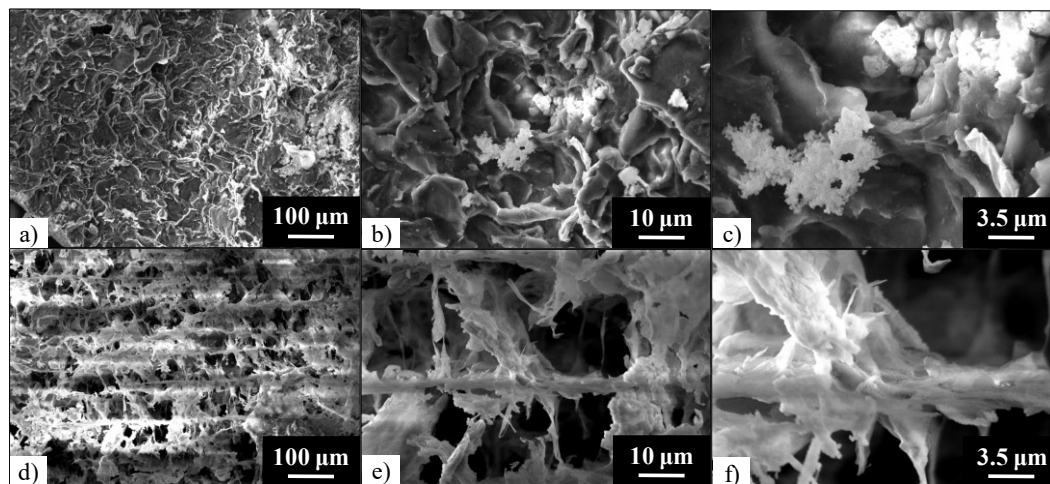
Figure 40. SEM micrographs of FD_G/PDAC (a, b, c) and FD_G/CNF (d, e, f) samples, at different magnifications.

As it was not possible to fabricate a sample with a foam structure using PDAC as a binder, the sample SBH_G_PDAC_FD was not investigated regarding its energy storage density and sorption rate.

Energy storage densities of prepared composites have been evaluated by DSC in a full dehydration cycle. Figure 41a shows the integrals of the DSC curves of the FD composites compared to the WI samples already presented in Figure 32.
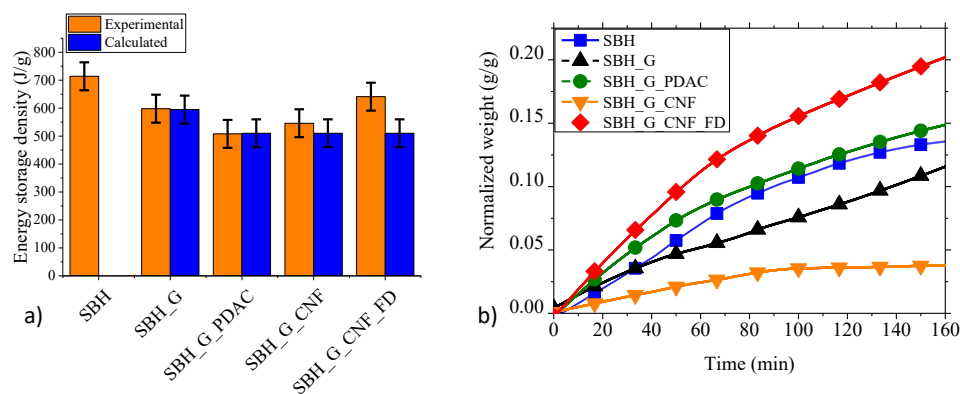
Figure 41. a) Experimental (orange) and calculated (blue) energy storage density values for the prepared samples. b) Sorption kinetics of the composite materials.

In Figure 41a, the orange bars represent the experimental energy storage density values evaluated from the DSC data, while the blue ones show the theoretical energy storage values of the composites obtained with equation (21). In particular, sample SBH_G_CNF_FD shows energy storage densities higher than the value obtained for SBH_G_CNF (both experimental and calculated). FD technique introduces therefore the possibility to enhance energy storage density compared to WI, probably due to a higher exposed salt/air interface that causes a higher concentration of water adsorbed on the salt surface. In fact, nanocellulose films exhibit strong interactions that can hinder water mass transfer from and to salt hydrates.

During hydration at 23°C 50% RH, pristine salt showed a linear mass gain, in the range of 7.0 %/h, for the first 70 min, followed by a progressive reduction in the hydration rate and leading to an approximate 12 % weight gain after 160 min. The addition of graphite in the sample SBH_G results in a reduced hydration rate (5.0 %/h), compared to the pristine salt, likely related to the barrier effect to moisture diffusion within the salt aggregates, induced by the presence of graphite flakes. Organic binders were also observed to strongly affect the hydration rate (chapter 4.2). In fact, SBH_G_PDAC hydration kinetics was slightly improved (7.9 %/h in the linear phase) with respect to the pristine salt. On the other hand, SBH_G_CNF showed the lowest hydration kinetics (2.4 %/h), which may be ascribed to the formation of a dense and packed structure due to the strong interactions between CNF. However, the possibility to produce open and oriented porous structures by FD can compensate for the barrier effect from CNF aggregation in bulk. Indeed, hydration rate for SBH_G_CNF_FD was found to be greatly enhanced (10.8 %/h), both compared to pristine SBH and SBH_G_PDAC, which is explained by the increased salt/air interfacial surface due to the previously commented porous structure (Figure 40). Beside the increase in water sorption rate, the change in volumetric energy density of the composite materials should also be considered, when addressing the design of a thermal storage system. Depending on the target application, the volume of the TCM bed, and therefore of the reactor, may be a limiting factor in the development of this technology [94]. The densities of the prepared composite materials were calculated in the range of ~0.5 g/cm^3 for

SBH_G, SBH_G_PDAC and SBH_G_CNF (obtained with WI technique) and ~0.1 g/cm^3 for SBH_G_CNF_FD. While FD is clearly expected to produce higher porosity compared to WI methods, it is worth noting that the porosity may be tuned by modifying the processing parameters, such as the weight ratios of the components in the starting dispersion [158], as well as the freezing temperature and speed [159]. In this way, the foam porosity can be adjusted to match the selected application requirement, in particular by identifying the suited balance between hydration kinetics and volumetric energy density stored. In fact, dehydration kinetic is directly affecting the power of thermochemical system. The target level of needed heating power varies according to the final application of the device (e.g. in the industrial, transport or residential field), but the low heating power was reported as one of the limiting factors in the scale up of prototypal thermochemical storage devices [131].

4.4   Sorption studies in humid TGA/DSC

Humid TGA/DSC is a well-established technique to characterize TCMs [109]. It couples a humidifier to standard TGA/DSC equipment, in order to control the RH of the inlet gas, in addition to temperature control. In this way, multiple hydration/dehydration cycles can be performed subsequently on the same sample. This analysis allows materials kinetics characterization closer to real operating conditions, since water vapor pressure in air highly influences the salts sorption kinetics (as explained in chapter 3.1).

For this purpose, seven formulations were prepared, with composition described in Table 13.

Table 13. Samples characterized with humid TGA/DSC.

Sample	SBH	G	g	Binder	Binder type	Preparation
SBH	1	0	0	0	None	None
SBH_G	5	1	0	0	None	WI
SBH_G_PDAC(0.5)	5	1	0	0.5	PDAC	WI
SBH_G_CMC	5	1	0	0.5	CMC	WI
SBH_g/G_CMC	5	0.7	0.3	0.5	CMC	WI
SBH_g_CMC	5	0	1	0.5	CMC	WI

In this case, in addition to a change in the binder type (PDAC or CMC), also the thermal conductive component was varied, using expanded graphite, graphene or a mixture of graphene and expanded graphite while maintaining the overall concentration of the graphitic material constant. The samples were analyzed both in powder form and after being tableted in order to standardize the materials morphology, density and surface/volume ratio.

Figure 42 shows the SEM images of the cross sections of the compressed tabs, obtained by mechanical fracture, produced to analyze the cross-section of the tabs.
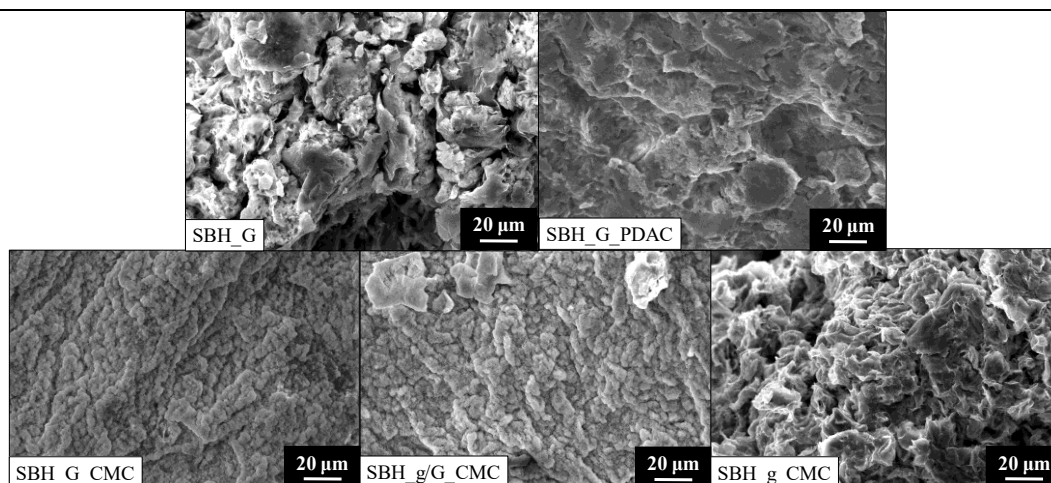
Figure 42. SEM micrographs of the prepared samples.

The images present different morphologies depending on the samples composition. Sample SBH_G (top left) is composed by a porous mixture of salt and graphite as already commented in the previous chapters (Figure 31 and Figure 33). SBH_G_PDAC (top right) shows a more compact structure in which the polymer contributes in the stabilization of the salt (chapter 4.2). In addition, sample SBH_G_CMC (bottom left) has a compact structure, but the salt is distributed with a granular architecture, differing from the smoother surfaces obtained with PDAC. The addition of graphene together with graphite in sample SBH_g/G_CMC (bottom middle) results in minor changes in the morphology. However, when graphene is used alone in sample SBH_g_CMC (bottom right) it affects the structure increasing the porosity of the mixture and making the salt grains only slightly detectable on the exposed surface, likely owing to the higher surface area of graphene compared to graphite.

Figure 43 reports the TGA/DSC test of a representative sample (SBH_G in powder form).
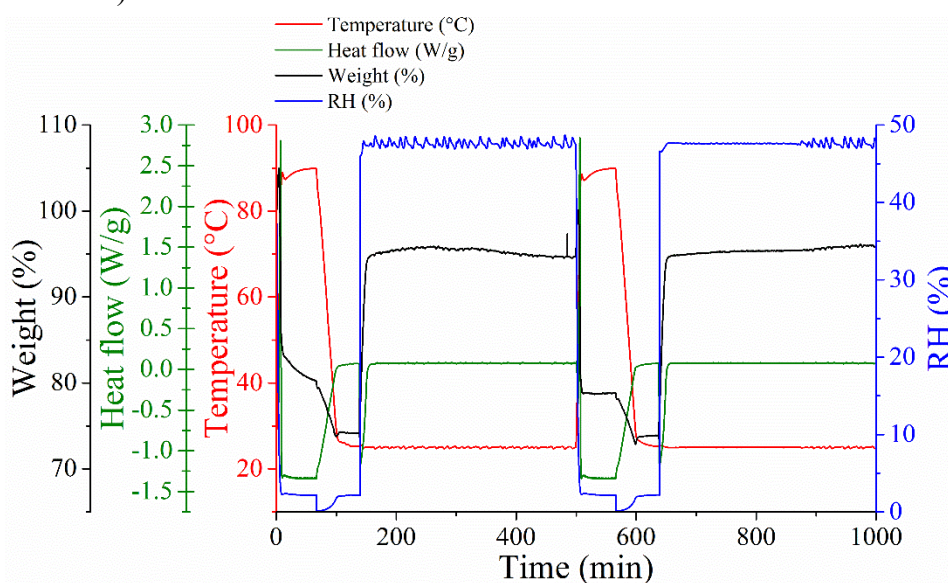
Figure 43. TGA/DSC analysis for sample SBH_G in powder form.

Since the hydration status of the samples was unknown before the measurements, they were analyzed with two identical and subsequent dehydration/hydration cycles at 1500 mbar of water vapor pressure, with dehydration at 90 °C and hydration at 25 °C. The first cycle was employed to obtain a fully hydrated sample, the second one to collect data on the hydration kinetics of the material. When the relative humidity of the analysis chamber is increased, the TGA signal (in black) shows an immediate increase in the sample mass and the DSC curve (in green) reports an endothermic peak, both confirming the samples hydration. To compare the performance of each prepared material, the hydration curve of the second cycle was considered. Figure 44 shows a comparison of the sorption curves for the analyzed materials in powder form (left) and after tableting (right).
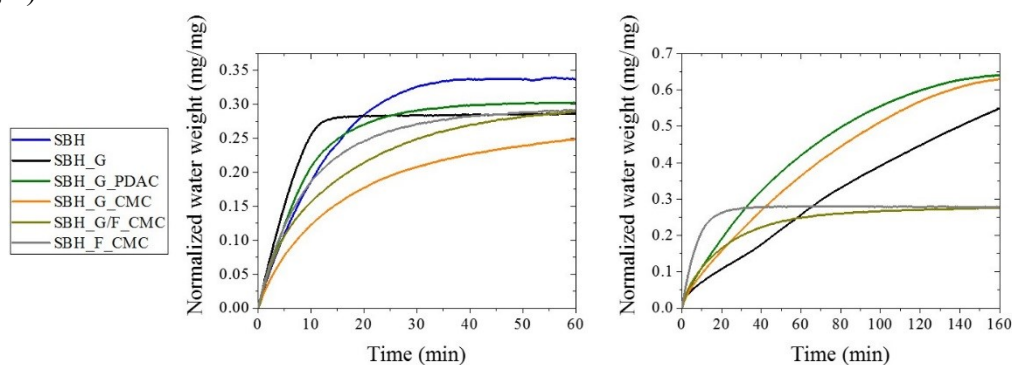
Figure 44. TGA hydration curves of prepared TCM composites in a) powder or b) tabs form.

The hydration curves for the powders show that the addition of a graphitic matrix can increase the sorption rate, probably due to a higher salt/air surface area available for the reaction. On the other hand, the further inclusion of a binder in the structure reduces sorption, indicating a hindrance to the water mass transfer generated by the presence of an additional component. Within the CMC containing samples, the change from pure expanded graphite to a mixture of expanded graphite and graphene or pristine graphene reveals a higher sorption rate for this latter. This effect can be explained by a broader distribution of the salt in the materials pores. Samples SBH, SBH_G and SBH_G_PDAC reached a plateau during the measurement that is related to the obtainment of a full hydrated state and is coherent with values already observed in this chapter (section 4.2).

To better compare the materials behavior, the powders were tableted to reduce the influence of different density and surface area of the samples in the sorption process. The measured densities of the analyzed samples are in the range of 2.6±0.1 g/cm^3. The resulting curves (Figure 44, right) present sorption performance that differ from the ones of the powders. In this case, the addition of binders always results in a higher sorption rate compared to sample SBH_G, in agreement with results obtained (section 4.2). While the formulations containing graphene present curves that are comparable to their powder form, all the samples with expanded graphite matrix show a higher mass sorption. This effect can be explained by considering that powders compression reduces the composite porosity, therefore

introducing a hindrance in water mass transfer. Expanded graphite presents a lower surface area compared to graphene, thus being affected by a reduction in the hydration kinetic after powders molding more than composites containing graphene. A difference in the two morphologies can be evaluated by comparing e.g. SEM micrographs of samples SBH_G_PDAC and SBH_g_CMC in Figure 42.

To further investigate this phenomenon, also a DSC analysis of sample SBH_G in tab form was performed, reported in Figure 45 together with the TGA curve.
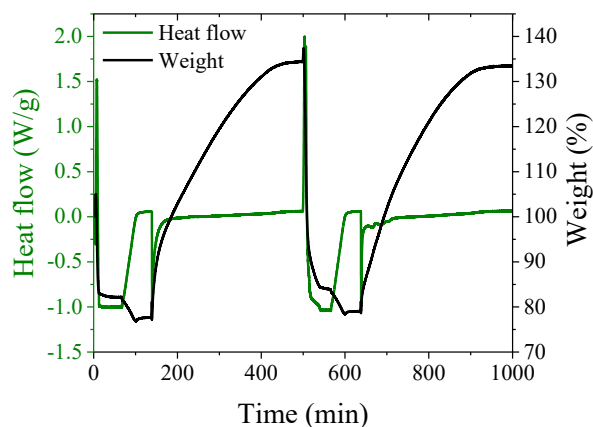
Figure 45. TGA/DSC analysis of SBH_G in powder form.

The energy density values for sample SBH_G in powder and tableted forms (obtained by integration of the DSC hydration peaks) are 655 J/g and 1340 J/g respectively. Since the value for SBH_G is expected from literature, the higher value for the tableted form confirms the presence of a higher quantity of sorbed water relative to the phenomena of over-hydration and solubilization. This phenomenon was already observed in literature by Posern et al. [160] and was explained as a correlation between an increase in water adsorbed by the matrix and a decrease in pore size caused by capillary condensation. While this effect increases in the composite energy storage density, it causes salt solubilization and dissolution at every cycle, thus introducing deep changes in the materials morphology and the risk of leakage.

Chapter 5

Thermochemical reactors: design, development and validation

Part of the work described in this chapter has been previously published in:

S. Salviati, N. Vasile, F. Carosio, G. Saracco, A. Fina, CFD Modeling of a Laboratory-Scale Setup for Thermochemical Materials Performance Analysis, in: COMSOL Conf. 2018 Lausanne, 2018.

The inclusion of TCMs in reactors is a mandatory step in the determination of their performance towards real applications. Dramatic changes in the materials performance occur when their masses are increased from the mg scale of TGA and DSC characterization to the g or kg scale of thermochemical systems, caused by mass and energy transport phenomena. This chapter reports all the work performed to develop novel reactors designs, with the aim to provide efficient ways of TCMs implementations. At first, different designs were tested in simple systems to preliminary determine the main issues related to those devices. Then, a closed and open reactor were addressed and evaluated.

5.1 Preliminary tests

In this chapter, two closed thermochemical setup concepts are presented with different layouts. In coupled systems, evaporator and condenser are composed of two separate chambers linked with a connection pipe. In uncoupled systems, two surfaces are included in the same container: one surface hosts the active material, holding and heating the salt bed, while the other carries out the function of condenser inducing water droplets condensation. These tests aim at the evaluation

of advantages and drawbacks in the two concepts and the preliminary study of salt hydrates performance in reactors.

Coupled system

In the tested coupled system, the evaporator is composed of a single neck round bottom flask, containing SBH, placed on a heater set at 120 °C. A rubber balloon was used as condenser to collect the desorbed water, while allowing system expansion on heating and a glass elbow pipe was used to connect the two. The glass flask and the connection pipe were covered with aluminum foil to reduce radiative heat loss. The system layout is reported in Figure 46.
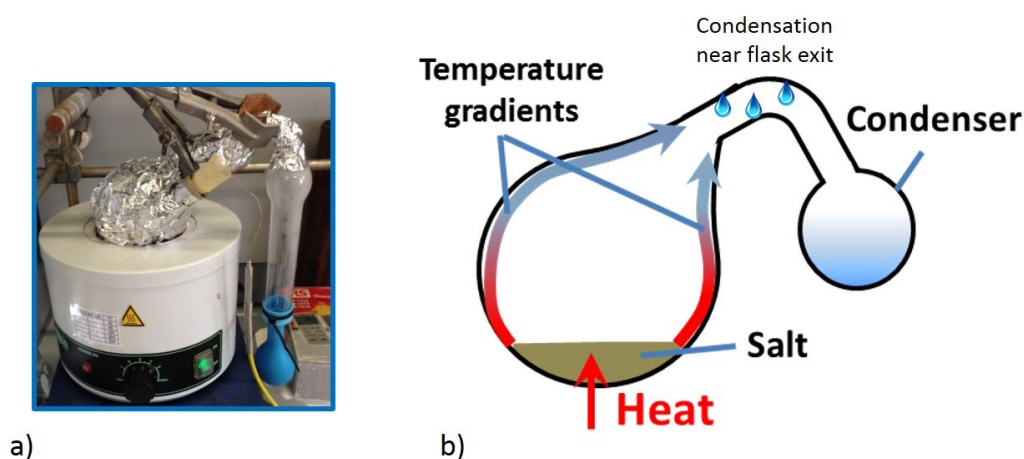
Figure 46. Picture (a) and scheme (b) of the coupled system used for preliminary tests.

During the experiment, the temperature of the flask exit is checked with a thermocouple, finding values near to room temperature and thus indicating a temperature gradient between the lower and upper part of the system. After the experiment, aluminum foil was removed ad water droplets were observed inside the transparent connecting glass pipe near the flask exit, but not in the condenser (Figure 46b). Because of the thermal gradient present on the surface between evaporator and condenser, water vapor pressure obtained because of the salt dehydration is high enough to allow water condensation at intermediate temperatures between the two components. It is therefore difficult to dehydrate the salt hydrates in this system, as the conditions cannot be fully controlled.

Modifications in the system layout can lead to a better heat and mass transfer management. For example, the addition of an airflow from the evaporator to the condenser as additional driving force could lead to a higher control in water condensation. This approach was tested in the closed reactor presented later in chapter 5.2 Another method to avoid undesired condensation phenomena is to include evaporator and condenser as two uncoupled areas in the same closed environment, thus removing thermal gradients on surfaces between the two components. Two system based on this approach are presented in this chapter.

Uncoupled system I

In the first uncoupled system, an electrical heater was placed under an aluminum plate with a diameter of 7 cm filled with $MgSO_4 \cdot 7H_2O$. Those components are closed in a chamber made by a petri dish and a becher, both made of PYREX glass, as shown in Figure 47. The glass surface available for condensation was measured as 380 ± 10 cm^2 by adding the internal surface of the becher to the uncovered surface of the dish.

During a test, the heater is set to 90°C and condensation is observed on the becher walls and on the petri. The salt weight is measured before and after each test on a balance. Three tests are performed varying salt mass and test time, as shown in Table 14.

Figure 47. Becher system.

The main advantage of this system compared to the coupled concept is that water condensation occurs on the chamber walls, without the possibility of droplet formation on undesired surfaces. The conversion α of the dehydration reaction is calculated with equation (19) and, as reported in Table 14, is equal to 0.56 at 90 min with 10 g of material. An increase in the dehydration time to 120 min increases the conversion to only 0.58, while doubling the amount of salt greatly reduces α to a value of 0.25. The strong effect of mass in the reaction kinetic was already evaluated for magnesium sulfate with smaller samples (5-50 mg) in TGA experiments [70]. Different concurrent effects contribute to the kinetics variation. A mass increase induces a delay in the heating of the entire sample, mainly caused by a low thermal conductivity of magnesium sulfate (~0.7 W/mK [99]). In addition, in our setup the size of the sample holder was maintained constant for all the tests, thus keeping a constant exposed salt surface while causing an increase in sample thickness together with the mass. This effect induces the formation of an insulating coverage that reduces heat transfer from the bottom of the sample (in contact with the heat source) to the top. Furthermore, the upper layers of the salt bed act as a physical barrier to water vapor transfer between the lower layers and air, thus decreasing the dehydration rates.

To better evaluate the influence of sample mass in the desorption process, an improved uncoupled setup was realized and tested.

Table 14. Parameters and conversion values for the experiments performed with uncoupled system I.

Test	Salt mass (g)	Time (min)	α (-)
1	10	90	0.56
2	20	90	0.25
3	10	120	0.58

Uncoupled system II

The second uncoupled system consists of a 7 cm diameter aluminum plate, identical to the one used in the first uncoupled system, placed on top of a metal cylinder and in the middle of a round aluminum container internally coated with Teflon and closed with a plastic bowl. The total surface available for water condensation is 2500 ± 10 cm^2. The salt is positioned in the plate (the evaporator) and dehydration is started by turning on an electrical heater placed under the cylinder. The salt hydrate is then heated at a temperature of 90 °C. Water condensation happens on the surfaces of the bowl and container. To improve the water vapor pressure difference between the two components, a cooling system made of pipes with running water is placed around the Teflon container. Figure 48 shows a picture ad a descriptive sketch of the system.
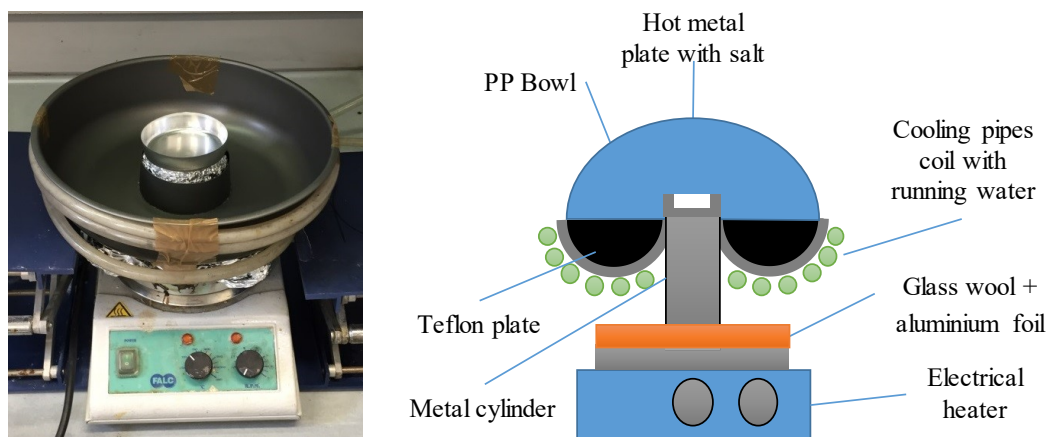
Figure 48. Picture (left) and scheme (right) describing the uncoupled system II. PP=polypropylene.

Two tests were performed using MgSO$_4$·7H$_2$O varying the sample mass: 10 g and 30 g. The conversion of the two samples over time is showed in Figure 49. As expected from experiments performed with the first uncoupled system, mass greatly influences the dehydration rate. By comparing the two setups, in the same experimental conditions (a temperature of 90 °C, a sample mass of 10 g and a dehydration time of 90 min), α is 0.9 in the second system instead of 0.56 as evaluated for the first setup. The second solution thus shows a substantial increase in dehydration rate. This effect is probably caused by the great increase in the

condensation surface (6.5 time wider) and in its lower temperature, provided by water cooling instead of exposure to the environment.
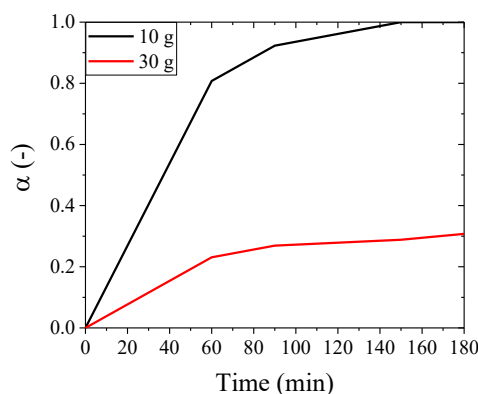
Figure 49. MgSO$_4$ hydrate conversions in uncoupled system II tests.

5.2 Closed thermochemical setup

As detailed in chapter two, closed thermochemical reactors provide the advantages of isolation from the environment, with no concerns on TCMs release and the possibility to work independently from ambient conditions. On the other hand, closed reactors are more complex in their design since these include a condenser, coupled with the salt bed and kept in controlled temperature and/or pressure to obtain conditions suitable for condensation. The presented approach in the design of a closed reactor is to build a small lab scale system that operates at ambient pressure, in which a forced airflow is introduced to facilitate the water mass transfer between the evaporator and the condenser. A multiphysical model is also developed based on the reactor geometry to evaluate the overall heat and water vapor mass transfer, air fluid dynamics, dehydration chemical reaction and water condensation in the condenser.

The design of the closed thermochemical setup is reported in Figure 50. The evaporator consists of a two-necked 250 ml Pyrex glass round bottom flask and the condenser of a 500 ml Pyrex glass Büchner conical flask. An air flux is generated by a LABOPORT® MINI pump, with a 2±0.25 l/min flow measured with a flowmeter (correspondent to an inlet velocity of 1.5 m/s). The evaporator is filled with 36 g of TCM, which is the graphene/salt composite SBH_G obtained with wet impregnation method (as described in chapter 2 of this thesis). The flask is then immersed in a silicon oil bath at a controlled temperature equal to 120 °C, while the condenser is kept in an ice bath. The evaporator temperature is chosen to represent a heat source able to fully dehydrate the salt. Water vapor concentration in air is measured with a Testo 0628.0021 humidity probe hygrometer and a type K thermocouple.

Figure 50. Descriptive scheme of the closed setup design.

The water condensation in the condenser is tracked by weighting the flask water on a technical balance with precision ±0.01 g. The evaporator containing the salt bed is also weight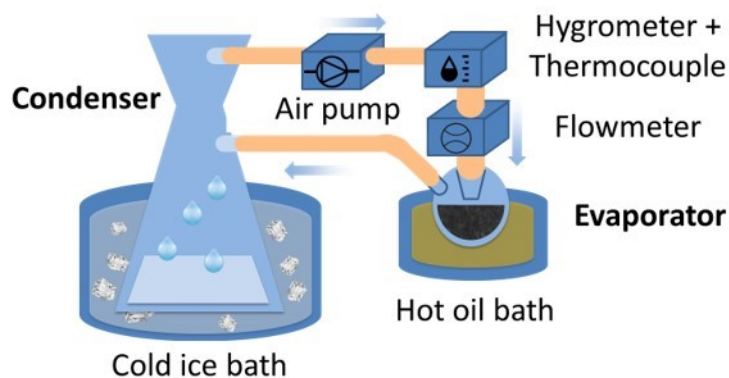ed before and after the test to track the crystallization water loss and to control that the evaporated water mass is equal to the condensed water mass, thus confirming the isolation of the reactor from the environment.

In this test, the charging phase of the thermochemical battery was studied experimentally, to develop a thermo-fluid-dynamics model. The aim of the presented modeling approach is to spatially calculate the evolution of the thermochemical process over time. Different physical phenomena were selected as the most important in the determination of the mechanism: water dehydration from the salt hydrate bed, condensation in the condenser, airflow, heat and mass transfer in air. While the full spatial representation of these phenomena presents high computational costs [161], we implemented a modeling approach that comprehends two different subsequent steps in order to reduce the calculation time. In the first step, named 0D, experimental water concentration in the condenser is fitted using Lavenberg-Marquardt least squares method to calculate k_1 and k_2 constants from equations (16) and (17). In this step, the reactions are considered as developing in a simplified geometry consisting of a batch environment, thus removing all the additional calculations required for a spatially resolved fitting. In the second step, named 3D, k_1 and k_2 values obtained in 0D step are used as first guess in the evaluation of the reactions in a geometry corresponding to the real reactor. Water vapor concentration in air, $[H_2O]_{vap}$, is evaluated as volumetric concentration (with units of mol/m^3) while both crystallization water contained in the salt $[H_2O]_{cry}$ and condensed water $[H_2O]_{liq}$ are studied as superficial concentrations (with units of mol/m^2). In addition, heat transfer and air fluid dynamics are studied in this step.

Figure 51 collects all the experimental and calculated water concentrations as a function of time. $[H_2O]_{liq}$ (green circles) is obtained by dividing the measured weight by the bottom area of the conical flask. Experimental $[H_2O]_{vap}$ (red circles) is obtained from temperature and humidity data using equation (28). Fitting curves are obtained for both $[H_2O]_{liq}$ and $[H_2O]_{vap}$ (green and red lines respectively). The obtained values for the equilibrium constants are 0.043 1/s for k_1 and 0.011 1/s for k_2. These are dependent from the geometry of the presented reactor as well as from

the temperature and airflow used. A calculated curve for the decreasing concentration $[H_2O]_{cry}$ (blue line) is also reported.
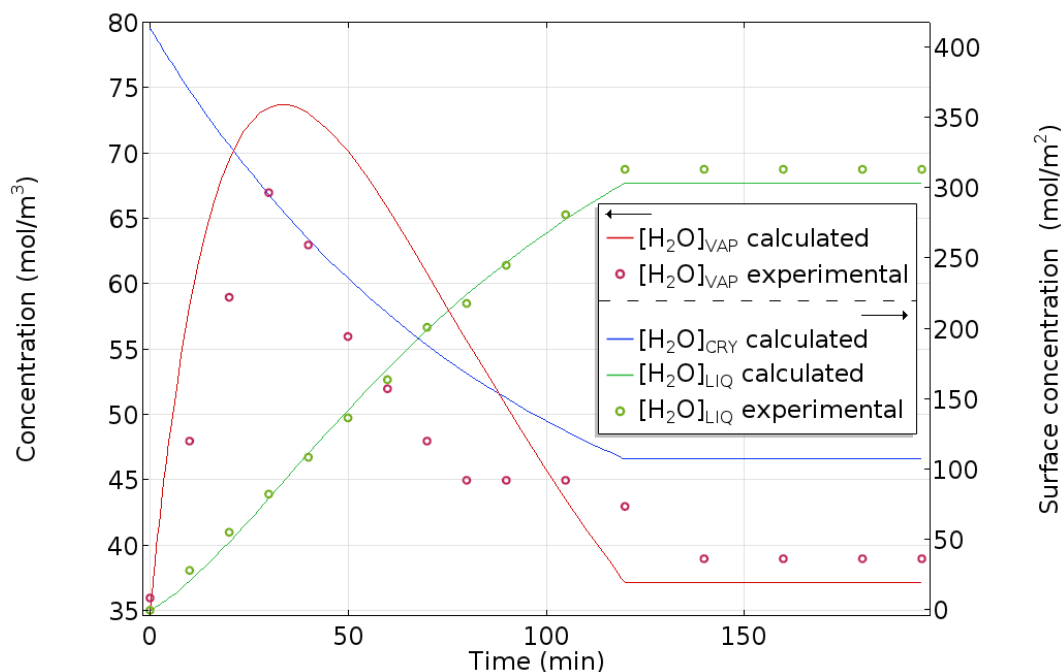
Figure 51. Experimental and fitted data for the reaction points.

In the 3D step, the full geometry of the reactor is drawn as reported in Figure 52. Both the salt bed and the condensation zone are modeled as two surfaces able to exchange water with the environment. The dehydration and condensation reactions are defined on the lower inner surface of the round flask and on the lower inner surface of the conical flask, respectively.
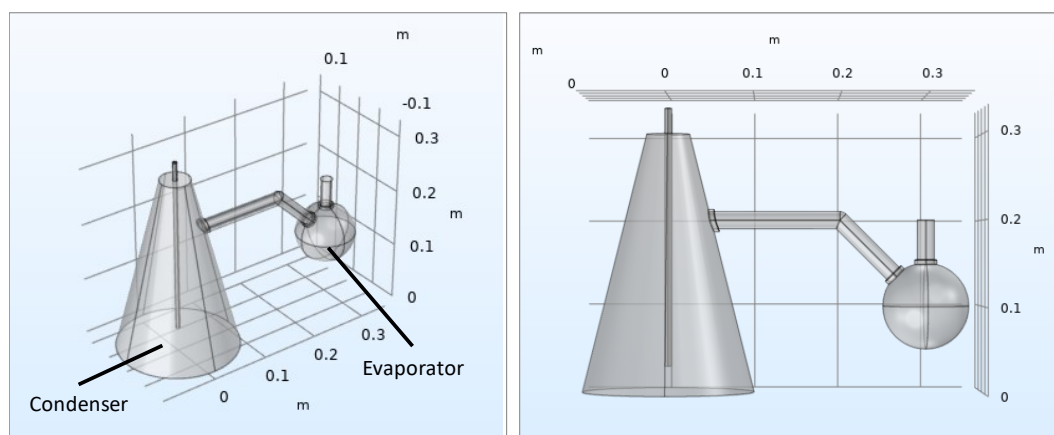
Figure 52. 3D model geometry from two different points of view.

Two temperatures are also set in the system based on the experimental conditions: 120 °C on the dehydration surface and 0 °C on the condensation surface. The forced airflow is applied from the evaporator to the condenser. Local air velocity and temperature are calculated as a function of time, reaching a stable

distribution after ~1000 s (Figure 53). Flow is considered in the laminar regime, showing the highest velocities at the center of the connecting pipes.
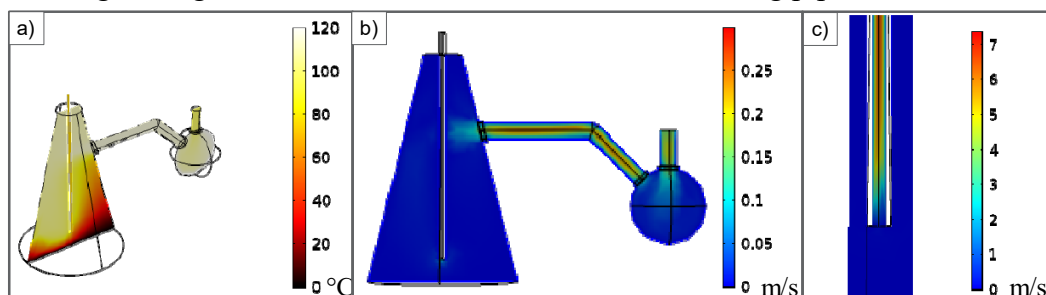
Figure 53. Temperature (a) and airflow velocity (b) distribution in the closed reactor, with a magnification over the outlet pipe (c), at time t=1000s.

In addition, the surface concentrations of crystallization and condensed water were calculated, as shown in Figure 54. While at the beginning of the test water is found only in the evaporator, at t=100 min almost all of the water is condensed in the flask, accordingly to experimental data.
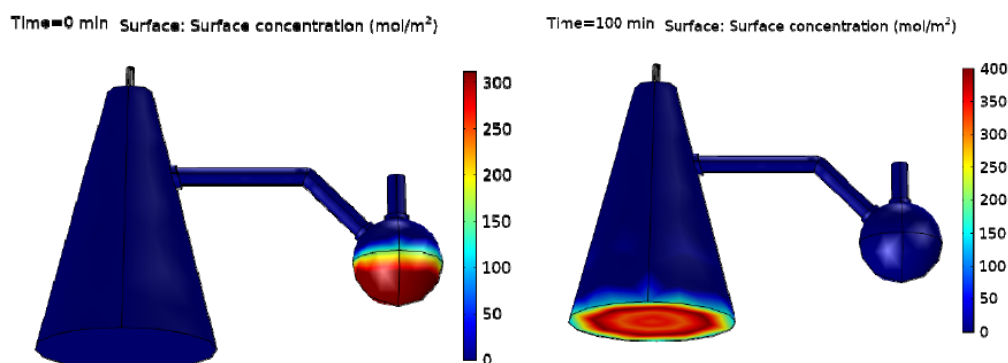
Figure 54. Concentration evolution of evaporator and condenser.

The calculated values of water concentration and temperature were used to evaluate the values of local RH inside the reactor with equation (23), assuming water vapor as an ideal gas.

$$RH = \frac{p_w(T, [H_2O]_{vap})}{p_{w,sat}(T)} = \frac{R \cdot T \cdot [H_2O]_{vap}}{p_{w,sat}(T)} \tag{23}$$

Here R is the gas constant and $p_{w,sat}$ is the water vapor saturation pressure calculated with Antoine equation (24), where A, B and C are empirical constants [128].

$$log_{10}(p_{w,sat}) = A - \frac{B}{C + T} \tag{24}$$

Two volumes were then defined in the reactor, depending on the value of RH, namely condensation zone for RH=100% and non-condensation zone for RH<100%. Figure 55 shows the evolution of the two regions over time in a vertical cross section. While at the beginning of the test condensation phenomena occur in different parts of the reactor, after 70 minutes the condensation zone is reduced due to an increase in temperature and a reduction in water vapor concentration caused by condensation.
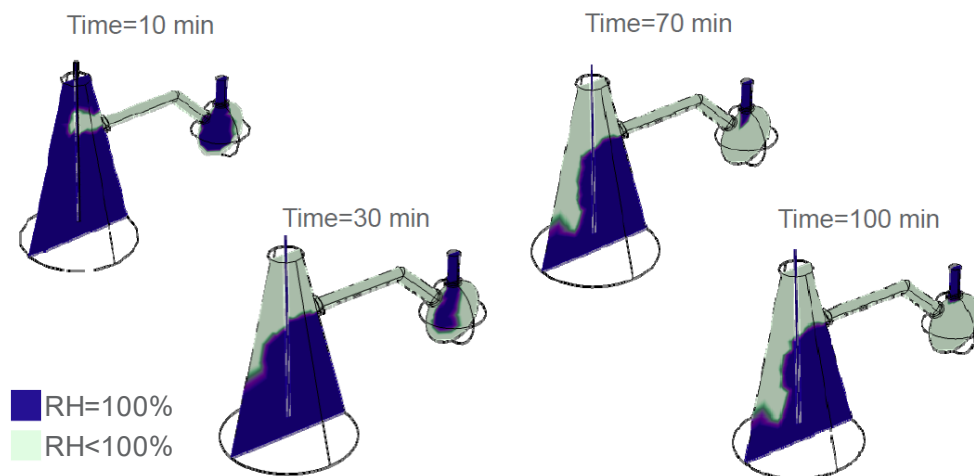
Figure 55. Evolution of condensation regions.

Therefore, this model provides a tool for the study of closed thermochemical reactors. By fitting experimental data on water condensation, it is possible to apply this approach in different system geometries, studying air fluid dynamics, temperature distribution, dehydration/condensation kinetics and water condensation areas. The model can be further developed in order to evaluate the reactor performance varying a key parameter, such as evaporator or condenser temperatures, inlet airflow or the dimensions of a component. For example, after the realization of experiments with different evaporator temperatures, it is possible to fit all the experimental data, studying the temperature dependence of k_1 and k_2 and therefore optimizing the reactor operating conditions.

5.3 Open thermochemical setup

An open thermochemical setup was assembled and tested in order to analyze the performance of composite TCMs developed in chapter 4. All the experiments were performed with a custom built experimental setup (Figure 56), based on a design developed by Gaeini et al. [131] .

Figure 56a reports the complete layout of the setup, which can be operated both in charging mode (dehydration) or discharging mode (hydration). In the first case, dry air (80 Pa at 25°C) at 4 bar flows in a Bronkhorst Gas Flow Controller (GFC) where the flow is set to 48 g/min (Figure 56a). After that, a heater placed before the reactor inlet raises air temperature to 90±2 °C. Then, without interrupting the airflow, inlet temperature is lowered to environmental conditions in order to cool

the reactor with dry air, avoiding salt rehydration. In discharging mode, air flows through a stainless steel vessel filled with deionized water and regulated with a Bronkhorst Liquid Flow Controller (LFC) at 28 g/h. Subsequently a Bronkhorst Controlled Evaporator Mixer (CEM) blends dry and wet flows at a temperature of 25 ± 2 °C to obtain a water vapor pressure of 1.5 kPa. The outlet water flow is measured with humidity and temperature sensors positioned after the reactor with a sampling rate of 0.1 Hz.
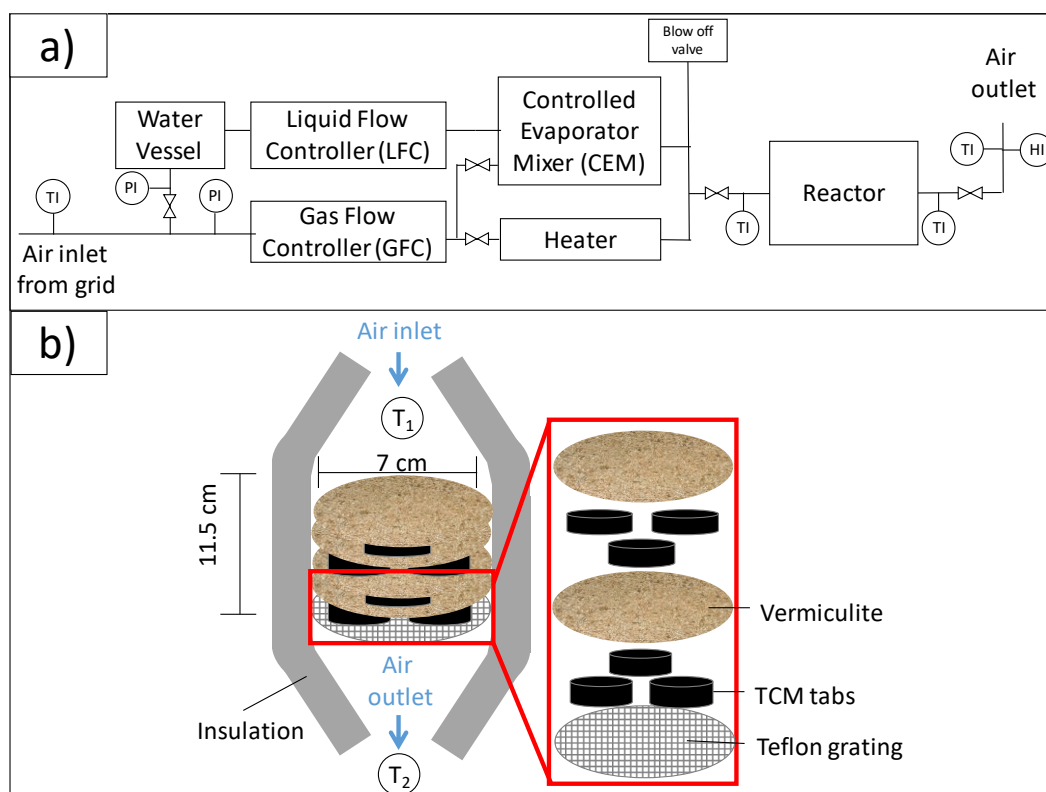
Figure 56. a) Thermochemical setup layout. b) Schematic representation of the reactor.

Figure 56b depicts the detail of the reactor. It is composed of an insulated cylinder with 11.5 cm height and 7 cm diameter made of stainless steel on the outside and of Teflon on the inside. Two thermocouples, set at a sampling rate of 0.1 Hz, were included to measure air temperature at the inlet and the outlet, namely T_1 and T_2 respectively.

Three materials already presented in chapter 4 were tested in the reactor: SBH, SBH_G and SBH_G_PDAC. Table 15 reports their mass and compositions.

Table 15. Masses, expressed in g, of the materials tested in the reactor and their components.

Sample	Composite	SBH	G	PDAC
SBH	100	100	0	0
SBH_G	120	100	20	0
SBH_G_PDAC	120	90	18	12

Formulations SBH_G and SBH_G_PDAC were included in the reactor as cylindrical tabs with a diameter of 30±0.1 mm, a height of 3.1±0.1 mm and a weight of 4.0±0.1 g each, already presented in chapter 4. As illustrated in Figure 56b, the composites were placed in the reactor in 10 layers of 3 tabs each, as an example of a modular and scalable design. In order to avoid contact between the tabs, 18 g of vermiculite pellets were used in each test to separate the layers. Vermiculite is widely used as supporting substrate in TCM fabrication because it presents low density and has no interactions with water [162]. Pristine SBH was mechanically mixed with 18 g of vermiculite and used to preliminarily test the reactor. All the materials were stored in closed containers in environmental conditions prior to the experiments.

The data collected with a Pico Technology TC-08 acquisition module from complete dehydration/hydration cycles were analyzed. The difference between outlet air temperature T_2 and inlet air temperature T_1 is calculated with equation (25) and an experimental error of ±3 °C was evaluated after multiple experiments.

$$\Delta T = T_2 - T_1 \tag{25}$$

The difference between the outlet water vapor flow $\dot{m}_{w,out}$ and inlet water vapor flow $\dot{m}_{w,in}$ is calculated with equation (26) with an error of ± 2 g/h evaluated after multiple experiments.

$$\Delta \dot{m}_w = \dot{m}_{w,out} - \dot{m}_{w,in} \tag{26}$$

While $\dot{m}_{w,in}$ is set at a value of 28 g/h, outlet vapor flow is calculated with the equation (27) [163].

$$\dot{m}_{w,\,out} = \dot{m}_{air} \cdot X = \dot{m}_{air} \cdot \frac{p_w}{p_{amb} - p_w} \cdot \frac{M_w}{M_{air}} \tag{27}$$

Where $\dot{m}_{air}$ is set at 48 g/min, X is the mixing ratio of water vapor in air, M_w and M_{air} are the molecular weights of water and dry air respectively, p_{amb} is the ambient pressure (1 atm) and p_w is the water vapor pressure calculated with equation (28):

$$p_w = p_{w,\,sat} \cdot RH \tag{28}$$

$p_{w,sat}$ is the water vapor saturation pressure calculated with Antoine equation [128] and RH is the relative humidity measured with the sensor at the outlet of the reactor.

The mass of water exchanged between TCM and environment m_w is then calculated using equation (29).

$$m_w = \int_{t_1}^{t_2} \Delta \dot{m}_w\,(t)\,dt \tag{29}$$

Where $t1$ and $t2$ are the starting and ending time of the experiment, respectively. The net convective power ΔP_{conv} is calculated with equation (30).

$$\Delta P_{conv} = P_{air,\,out} - P_{air,\,in} \tag{30}$$

$P_{air,\,in}$ and $P_{air,\,out}$ are calculated with equations (31) and (32) respectively, where $C_{p,air}$ and $C_{p,w}$ are the values of heat capacities for air and water.

$$P_{air,\,in} = (\dot{m}_{air} C_{p\,air} + \dot{m}_{w,\,in} C_{p,\,w}) \cdot T_1 \tag{31}$$

$$P_{air,\,out} = (\dot{m}_{air} C_{p,\,air} + \dot{m}_{w,\,out} C_{p,\,w}) \cdot T_2 \tag{32}$$

At first, two dehydration/hydration cycles were performed with the SBH/vermiculite mixture with the aim to set known starting experimental conditions and to evaluate the reactor performance. The calculated values from the latter are reported in Figure 57. During dehydration (Figure 57a), both T_1 and T_2 increase, the former reaching the set value of 90 °C at t=1.0 h and the latter reaching a plateau at 80 °C at t=~1.5 h. In steady state condition, a temperature gradient inside the reactor is observed, with a difference between T_1 and T_2 of ~10 °C, related to a heat loss of the system in the experimental setup. The time delay in temperature increase of T_2 is caused by heat transferred to the reactor components and the salt bed $\Delta \dot{m}_w$ rises at the beginning of the experiment, reaching a peak value of 23 g/h, due to salt dehydration that increases outlet air humidity until t=1.75 h, when the reaction is considered completed. During hydration (Figure 57b), T_1 is stable at the set point value of 25 °C, while T_2 increases due to heat released from the salt bed to the airflow, reaching a peak value of 46 °C. $\Delta \dot{m}_w$ drops to -27 g/h at the beginning of the test due to humidity sorbed by the salt, rising linearly to a value of 0 at t=4.5 h, where the hydration reaction is considered completed. During the tests, the decrease in T_2 and $\Delta \dot{m}_w$ before t=0.1 h is caused by the equilibration of the system from environmental to experimental conditions. These experiments indicate the correct functioning of the reactor in both charging and discharging phases.
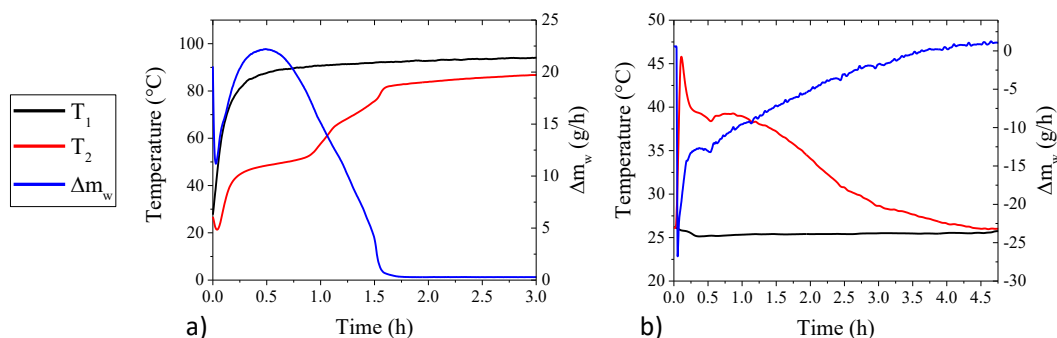
Figure 57. Temperature and water vapor flow difference for SBH_G_PDAC during the 4th cycle of a) dehydration and b) hydration.

Composites SBH_G and SBH_G_PDAC were then tested, performing four hydration/dehydration cycles for each set of tabs. No significant differences for the two formulations in the four cycles are evaluated in ΔT and $\Delta \dot{m}_w$ within the experimental errors and cycle 4 for each material is taken as representative test to illustrate the obtained results (Figure 58). The salt hydrate reaction phenomena is not detectable after t=~1.75 h for dehydration (Figure 58a) and after t=2 h for hydration (Figure 58b). Peak values for ΔT during discharge phase are in the range 14±3 °C.
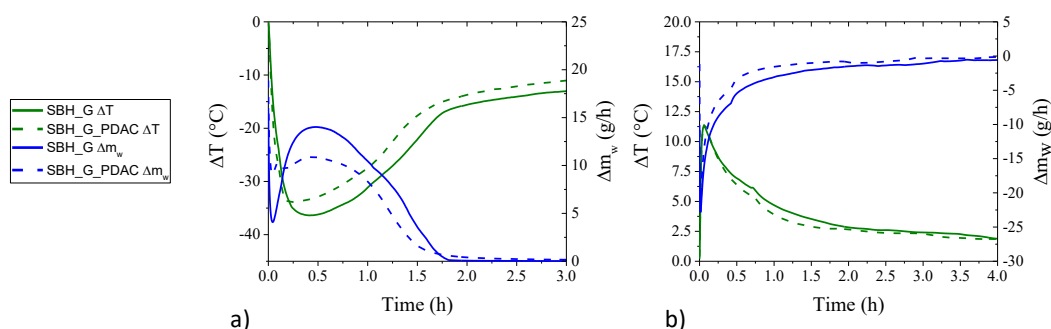
Figure 58. ΔT and $\Delta \dot{m}_w$ for a) dehydration and b) hydration of representative tests with SBH_G and SBH_G_PDAC.

Table 16 reports the integrated values of desorbed water m_w for cycles 2, 3 and 4 for the tests with composites. Cycle 1 is not reported because the materials were not in controlled temperature and humidity conditions before the first experiments.

Integrated values obtained for hydration steps are not presented since values lower than for the subsequent dehydration were obtained, suggesting these values to be affected by a systematic experimental error. In fact, since in hydration experiments the recorded RH values are much lower than environmental humidity, it is possible that outflow values were not measured correctly.

Considering the integrated values for dehydration steps, it is apparent that both composites are unable to fully dehydrate and rehydrate accordingly to the theoretical values (calculated considering the weight fraction of salt in the composites). Within the experimental error of ±2 g in Δm_w, it is not possible to

detect differences between SBH_G and SBH_G_PDAC, despite the great variations in sorption kinetics evaluated in climatic chamber experiments (Figure 39a in chapter 4.2). The discrepancies in these results can be related to different experimental conditions. In particular, the presence of the airflow in the reactor that forces the contact between water vapor and the TCM surface reduces the auxiliary effect provided by the polymer in the static humidity conditions of the climatic chamber.

Table 16. Integrated values, expressed in g, for Δm_w curves.

	SBH_G	SBH_G_PDAC
Theoretical water	25	25
Dehydration 2	-*	16
Dehydration 3	14	13
Dehydration 4	16	12

*non detectable due to technical failure of the setup.

Convective power curves for the hydration process are reported in Figure 59. Since measured values for $\dot{m}_{air}$ are two orders of magnitude higher than $\dot{m}_{w,in}$ and $\dot{m}_{w,out}$ for all the tested materials, the water flow terms are not included in equations 31 and 32 for power calculation. A power peak in the range 10-12 W and an average provided power in the range 1-3 W is calculated without detectable differences between the two composites and during the cycles, resulting in an average material power density (up to 10 h) of 10-100 mW/g, depending on the inlet temperature variation. A comparable material power of 90 mW/g for 3 h was obtained by Zhao et al. [119], testing 4.2 kg of a similar composite material realized with a higher SBH:G weight ratio (9:1), no binders and low density (0.743 g/cm^3) in a closed thermochemical reactor.
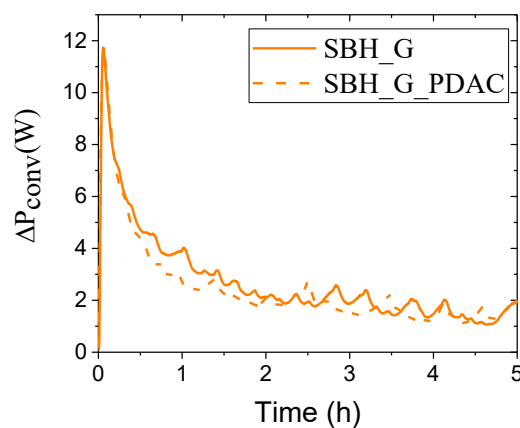
Figure 59. ΔP in hydration of representative tests with SBH_G and SBH_G_PDAC.

While the presented tabs based geometry can be further improved in order to match application related requirements, the exploitation of salt hydrates in modular blocks with cylindrical shape was tested as a route for the development of thermochemical energy storage systems. In order to fully characterize the behavior

of PDAC in SBH/G composites, further investigation on different tabs layout in the reactor as well as temperature and humidity conditions may be useful to elucidate the performance obtainable within and open reactor. Unfortunately, such a comprehensive study was not possible in this thesis, since these experiments were developed during a fixed time visiting period at Eindhoven University of Technology (NL).

Chapter 6

General conclusions

This thesis focused on the development of materials and devices for TES via the realization of novel thermochemical composites and reactors. The main conclusions derived from the obtained results are summarized in this chapter.

Research activities on materials were focused on the production of composites comprising of strontium bromide hexahydrate, expanded natural graphite, and polymeric binders for thermochemical energy storage applications, using a simple and environmentally sustainable water-based process.

Tests on the exploitation of binders in TCMs resulted in an enhancement in energy density due to an active contribution of hygroscopic polymers to the thermochemical storage process. The concentration of one selected binder (PDAC) was then varied to investigate its influence on the TCM performance. Morphological analysis demonstrated how the polymer binder controls the organization of the SBH particles, both in terms of their cohesion and adhesion to the graphite flakes. The materials were characterized with different thermal analysis techniques to assess their performance in terms of energy storage density and capability of heat and mass transfer. The prepared composites were then molded in centimeter-scale tabs suitable for exploitation in a modular-design reactor, in order to analyze their hydration kinetics and thermal conductivity properties. High contents of PDAC polyelectrolyte (SBH_G_PDAC(1)) resulted in reduced dehydration kinetics and energy storage densities. On the other hand, low PDAC contents (SBH_G_PDAC(0.1) or SBH_G_PDAC(0.5)) did not affect dehydration kinetics and caused minimal reduction in energy storage density. Tabs prepared with SBH_G_PDAC(0.5) were found to have significantly higher hydration rates in ambient conditions (23 °C and 50% RH) with respect to the conventional SBH_G composites. Indeed, the polyelectrolyte-containing formulation allowed to reach complete hydration of the tabs in ~10 h, while the samples with no PDAC reached only ~35% of total hydration in the same time. These results relate to the physical

action of the organic polyelectrolyte, acting as a binder between salt crystals, controlling moisture diffusion, and mechanically stabilizing the structure against stress-cracking, which is typical of pristine salt and salt/graphite formulations. Moreover, a state of the art value of 16 W/mK thermal conductivity was obtained for the tabs, with no substantial effects due to the presence of the polyelectrolyte.

Furthermore, CNF were employed for the first time as green and bio-based structural component and compared with PDAC, employed as an alternative polyelectrolyte binder. Freeze-drying was employed as preparation route and compared to wet impregnation. This foam is characterized by an open and randomly oriented porous structure, where the nanofibrils act as continuous matrix embedding the graphite and the salt and provide structural integrity, with the presence of channels assuring efficient moisture transport. The porous structure produced upon freeze-drying of CNF-based composites was found to deliver superior hydration kinetics (+ 54% with respect to the pristine hydrated salt), and hence a higher power supply compared to traditional materials obtained by wet impregnation. Freeze-drying of salt hydrate-based composites was therefore validated as a valuable process for the fabrication of improved composite materials towards the scale up of thermochemical energy storage.

Humid TGA/DSC was then used to characterize composite TCMs, varying the polymeric binder (PDAC and CMC) as well as the conductive component (expanded graphite or graphene). The sorption performance of pressed samples was then compared to materials in powder form highlighting how composites containing expanded graphite experienced a reduction in sorption kinetics caused by salt solubilization due to water condensation in the pores while samples comprising graphene maintained the same sorption rate. This phenomenon was explained with an increased pore reduction in graphite-based compared to graphene-based composites after compression.

Overall, the results collected clearly demonstrate the proposed approaches as promising strategies for the design of efficient thermochemical storage materials. However, following the findings here reported and discussed, some aspects remain to be investigated. Future studies should aim to investigate the cyclability of multiple hydration/dehydration cycles of the composite tabs, under controlled airflow, as well as their engineering in order to exploit processing conditions and geometries capable of reducing charge/discharge cycles and improving the efficiency of the system. Mechanical characterizations of the tabs might also prove important to better understand the stabilizing effect of the polyelectrolyte in the composite structure. All these characteristics will help in the design and fabrication of a TCM suitable for low grade heat reuse and ready for a scale up in prototypes focused on daily and seasonal storage applications, especially where a fast and controlled heat discharge is required, thus overcoming the drawbacks of conventional thermal storage materials.

This thesis also addressed the study of multiple reactor designs, both closed and open systems. The aim of these experiments was to evaluate the performance of TCMs in proof of concept reactors, while the development of a complete system, directly implementable in real applications, is beyond the scope of this thesis.

Closed reactors, usually composed of an evaporator and a condenser, allow the isolation of the materials from the environment, avoiding the use of ambient humidity and contaminations. Rigid temperature and pressure conditions are required due to thermodynamic constraints of TCM hydration/dehydration and condensation/evaporation of water. An innovative design was preliminary evaluated, in which evaporator and condenser are uncoupled as two different surfaces placed in the same chamber. This system provides the advantage of removing temperature gradients on connecting surfaces, avoiding unwanted condensation phenomena. Furthermore, an increase in dehydration rate was recorded in uncoupled systems after an expansion in the condenser area, while this parameter is strictly dependent on geometry and must be addressed separately in each design.

A lab scale closed reactor comprising a forced airflow was also assembled and used to test the dehydration phase of a graphite/salt TCM, developing a thermofluid dynamics, spatially resolved model. A simulation approach divided in two steps was implemented for the first time in the study of a thermochemical reactor. The evolution of temperature, air velocity and water vapor concentration distributions were efficiently represented. In addition, a tool for the representation of condensation areas with >99% RH was tested as a valuable resource in reactors design.

Eventually, an open reactor was used to perform scale up experiments on composite tabs SBH_G and SBH_G_PDAC already characterized for their hydration in a climatic chamber. Open systems present a simpler approach in reactor design, in which an external airflow is forced through the material bed and used as heat and mass transfer medium. This reactor was evaluated in both charge and discharge modes, observing no differences between the two composites and obtaining an output power in the range of a few tens of mW/g.

The results reported in this thesis introduce the possibility of salt hydrate-based TCMs performance enhancement. On the one hand, the development of composites comprising polymeric binders provide improved sorption kinetics, thermal conductivity and mechanical stability compared to state of the art materials. On the other hand, new reactor concepts allow a better understanding of TCMs scalability and performance. Therefore, the comprehension of phenomena governing the thermochemical processes sets the necessary basis for scale up and application of this technology, towards a sustainable use of thermal energy.

References

[1]   United Nations, Paris Agreement on Climate Change, United Nations Framew. Conv. Clim. Chang. (2015) 27–52. http://bigpicture.unfccc.int/#content-the-paris-agreemen.

[2]   International Energy Agency, Co2 Emissions From Fuel Combustion 2018 Overview, (2018).

[3]   X. Zhang, Energy Solutions to Combat Global Warming, 2017. doi:10.1007/978-3-319-26950-4.

[4]   M. Aneke, M. Wang, Energy storage technologies and real life applications – A state of the art review, Appl. Energy. 179 (2016) 350–377. doi:10.1016/j.apenergy.2016.06.097.

[5]   S. Kalaiselvam, R. Parameshwaran, Thermal Energy Storage Technologies for Sustainability, Academic Press, 2014. doi:10.1016/B978-0-12-417291-3.00002-5.

[6]   P. Arce, M. Medrano, A. Gil, E. Oró, L.F. Cabeza, Overview of thermal energy storage (TES) potential energy savings and climate change mitigation in Spain and Europe, Appl. Energy. 88 (2011) 2764–2774. doi:10.1016/j.apenergy.2011.01.067.

[7]   IEA, Technology Roadmap Energy Storage, 2014. doi:10.1007/SpringerReference_7300.

[8]   B. Arcuri, C. Spataru, M. Barrett, Evaluation of ice thermal energy storage (ITES) for commercial buildings in cities in Brazil, Sustain. Cities Soc. 29 (2017) 178–192. doi:10.1016/j.scs.2016.12.011.

[9]   M.T. Islam, N. Huda, A.B. Abdullah, R. Saidur, A comprehensive review of state-of-the-art concentrating solar power (CSP) technologies: Current status and research trends, Renew. Sustain. Energy Rev. 91 (2018) 987–1018. doi:10.1016/j.rser.2018.04.097.

[10]   A. Eisentraut, A. Brown, Secure Sustainable Together FEATURED INSIGHT HEATING WITHOUT GLOBAL WARMING Market Developments and Policy Considerations for Renewable Heat, (2014). https://www.iea.org/publications/freepublications/publication/FeaturedInsight_HeatingWithoutGlobalWarming_FINAL.pdf.

[11]   J. Xu, R.Z. Wang, Y. Li, A review of available technologies for seasonal thermal energy storage, Sol. Energy. 103 (2014) 610–638. doi:10.1016/j.solener.2013.06.006.

[12]   M.P. Islam, T. Morimoto, Advances in low to medium temperature non-concentrating solar thermal technology, Renew. Sustain. Energy Rev. 82 (2018) 2066–2093. doi:10.1016/j.rser.2017.08.030.

[13]   L. Miró, J. Gasia, L.F. Cabeza, Thermal energy storage (TES) for industrial waste heat (IWH) recovery: A review, Appl. Energy. 179 (2016) 284–301. doi:10.1016/j.apenergy.2016.06.147.

[14]   R. De Boer, S.F. Smeding, K. Biesheuvel, Waste Heat recovery in industrial batch processes: analysis of combined heat storage and heat pump application., 12th IEA Heat Pump Conf. (2013) 1–9.

https://www.ecn.nl/publications/PdfFetch.aspx?nr=ECN-M--17-008.

[15] P. Kauranen, T. Elonen, L. Wikström, J. Heikkinen, J. Laurikko, Temperature optimisation of a diesel engine using exhaust gas heat recovery and thermal energy storage (diesel engine with thermal energy storage), Appl. Therm. Eng. 30 (2010) 631–638. doi:10.1016/j.applthermaleng.2009.11.008.

[16] M. Nasri, I. Burger, S. Michael, H.E. Friedrich, Waste heat recovery for fuel cell electric vehicle with thermochemical energy storage, 2016 Elev. Int. Conf. Ecol. Veh. Renew. Energies. (2016) 1–6. doi:10.1109/EVER.2016.7476439.

[17] Y. Kato, Thermal Energy Storages in Vehicles for Fuel Efficiency, n.d.

[18] G. Li, Sensible heat thermal storage energy and exergy performance evaluations, Renew. Sustain. Energy Rev. 53 (2016) 897–923. doi:10.1016/j.rser.2015.09.006.

[19] A. V. Novo, J.R. Bayon, D. Castro-Fresno, J. Rodriguez-Hernandez, Review of seasonal heat storage in large basins: Water tanks and gravel–water pits, Appl. Energy. 87 (2010) 390–397. doi:10.1016/J.APENERGY.2009.06.033.

[20] L. Mesquita, D. McClenahan, J. Thornton, J. Carriere, B. Wong, Drake Landing solar community: 10 years of operation, ISES Sol. World Congr. 2017 - IEA SHC Int. Conf. Sol. Heat. Cool. Build. Ind. 2017, Proc. (2017) 333–344. doi:10.18086/swc.2017.06.09.

[21] Drake Landing Solar Community, (n.d.). www.dlsc.ca.

[22] H. Nazir, M. Batool, F.J. Bolivar Osorio, M. Isaza-Ruiz, X. Xu, K. Vignarooban, P. Phelan, Inamuddin, A.M. Kannan, Recent developments in phase change materials for energy storage applications: A review, Int. J. Heat Mass Transf. 129 (2019) 491–523. doi:10.1016/j.ijheatmasstransfer.2018.09.126.

[23] S.E. Kalnæs, B.P. Jelle, Phase change materials and products for building applications: A state-of-the-art review and future research opportunities, Energy Build. 94 (2015) 150–176. doi:10.1016/j.enbuild.2015.02.023.

[24] A. De Gracia, L.F. Cabeza, Phase change materials and thermal energy storage for buildings, Energy Build. 103 (2015) 414–419. doi:10.1016/j.enbuild.2015.06.007.

[25] J. KoŚny, K. Biswas, W. Miller, S. Kriner, Field thermal performance of naturally ventilated solar roof with PCM heat sink, Sol. Energy. 86 (2012) 2504–2514. doi:10.1016/j.solener.2012.05.020.

[26] A.S. Garrigos, Phase change materials characterization (PCM) and thermochemical materials (TCM) development and characterization towards reactor design for thermal energy storage, (2015).

[27] A. Safari, R. Saidur, F.A. Sulaiman, Y. Xu, J. Dong, A review on supercooling of Phase Change Materials in thermal energy storage systems, Renew. Sustain. Energy Rev. 70 (2017) 905–919. doi:10.1016/j.rser.2016.11.272.

[28] S. Puupponen, A. Seppälä, Cold-crystallization of polyelectrolyte absorbed polyol for long-term thermal energy storage, Sol. Energy Mater. Sol. Cells. 180 (2018) 59–66. doi:10.1016/j.solmat.2018.02.013.

[29] B. Sandnes, The physics and the chemistry of the heat pad, Am. J. Phys. 76 (2008) 546–550. doi:10.1119/1.2830533.

[30] K.E. Nielsen, M. Molinas, Superconducting Magnetic Energy Storage (SMES) in power systems with renewable energy sources, IEEE Int. Symp. Ind. Electron. (2010) 2487–2492. doi:10.1109/ISIE.2010.5637892.

[31] L. Zhou, Z. Qi, Review of flywheel energy storage system, ISES Sol. World Congr. 2007, ISES 2007. 4 (2007) 2815–2819. doi:10.1109/PowerEng.2011.6036455.

[32] A. González, E. Goikolea, J.A. Barrena, R. Mysyk, Review on supercapacitors: Technologies and materials, Renew. Sustain. Energy Rev. 58 (2016) 1189–1206. doi:10.1016/j.rser.2015.12.249.

[33] S. Rehman, L.M. Al-Hadhrami, M.M. Alam, Pumped hydro energy storage system: A technological review, Renew. Sustain. Energy Rev. 44 (2015) 586–598. doi:10.1016/j.rser.2014.12.040.

[34] H. Lund, G. Salgi, The role of compressed air energy storage (CAES) in future sustainable energy systems, Energy Convers. Manag. 50 (2009) 1172–1179. doi:10.1016/j.enconman.2009.01.032.

[35] R. Dufo-López, J.L. Bernal-Agustín, Techno-economic analysis of grid-connected battery storage, Energy Convers. Manag. 91 (2015) 394–404. doi:10.1016/j.enconman.2014.12.038.

[36] H.J.G. Diersch, D. Bauer, Analysis, modeling and simulation of underground thermal energy storage (UTES) systems, Woodhead Publishing Limited, 2014. doi:10.1533/9781782420965.1.149.

[37] M. Bonte, P.J. Stuyfzand, A. Hulsmann, P. van Beelen, Underground thermal energy storage: Environmental risks and policy developments in the Netherlands and European Union, Ecol. Soc. 16 (2011). doi:10.5751/ES-03762-160122.

[38] E. González-Roubaud, D. Pérez-Osorio, C. Prieto, Review of commercial thermal energy storage in concentrated solar power plants: Steam vs. molten salts, Renew. Sustain. Energy Rev. 80 (2017) 133–148. doi:10.1016/j.rser.2017.05.084.

[39] Y.H. Yau, B. Rismanchi, A review on cool thermal storage technologies and operating strategies, Renew. Sustain. Energy Rev. 16 (2012) 787–797. doi:10.1016/j.rser.2011.09.004.

[40] H. Jarimi, D. Aydin, Z. Yanan, G. Ozankaya, X. Chen, S. Riffat, Review on the recent progress of thermochemical materials and processes for solar thermal energy storage and industrial waste heat recovery, Int. J. Low-Carbon Technol. (2018) 1–26. doi:10.1093/ijlct/cty052.

[41] J. Cot Gores, Compact thermal storage a-state-of-the-art review of experimental results, Treballs Final Màster (UDL. Ciències Apl. a l'Enginyeria). (2011) 103. http://hdl.handle.net/10459.1/45826.

[42] G. Streckienė, V. Martinaitis, A.N. Andersen, J. Katz, Feasibility of CHP-plants with thermal stores in the German spot market, Appl. Energy. 86 (2009) 2308–2316. doi:10.1016/J.APENERGY.2009.03.023.

[43] Ž. Bogdan, D. Kopjar, Improvement of the cogeneration plant economy by using heat accumulator, Energy. 31 (2006) 2285–2292. doi:10.1016/J.ENERGY.2006.01.012.

[44] Y. Ding, S.B. Riffat, Thermochemical energy storage technologies for building applications: a state-of-the-art review, Int. J. Low-Carbon Technol. 8 (2012) 106–116. doi:10.1093/ijlct/cts004.

[45] CREATE, (n.d.). http://www.createproject.eu/.

[46] SWSheating, (n.d.). http://www.swsheating.eu/.

[47] K.E. N'Tsoukpoe, H. Liu, N. Le Pierrès, L. Luo, A review on long-term sorption solar energy storage, Renew. Sustain. Energy Rev. 13 (2009) 2385–2396. doi:10.1016/j.rser.2009.05.008.

[48] N. Yu, R.Z. Wang, L.W. Wang, Sorption thermal storage for solar energy,

Prog. Energy Combust. Sci. 39 (2013) 489–514. doi:10.1016/j.pecs.2013.05.004 Review.

[49] A. Žužić, V. Filipan, Absorption cooling devices with LiBr/H2O as working media, Chem. Eng. Trans. 52 (2016) 61–66. doi:10.3303/CET1652011.

[50] K. Gommed, G. Grossman, F. Ziegler, Experimental investigation of a LiCI-water open absorption system for cooling and dehumidification, J. Sol. Energy Eng. Trans. ASME. 126 (2004) 710–715. doi:10.1115/1.1643075.

[51] A. Hauer, Thermal Energy Storage with Zeolite for Heating and Cooling Applications, Int. Sorption Heat Pump Conf. 2002. 1 (2002) 385–390.

[52] A. Ristić, N.Z. Logar, S.K. Henninger, V. Kaučič, The performance of small-pore microporous aluminophosphates in low-temperature solar energy storage: The structure-property relationship, Adv. Funct. Mater. 22 (2012) 1952–1957. doi:10.1002/adfm.201102734.

[53] A. Elsayed, E. Elsayed, R. AL-Dadah, S. Mahmoud, A. Elshaer, W. Kaialy, Thermal energy storage using metal–organic framework materials, Appl. Energy. 186 (2017) 509–519. doi:10.1016/j.apenergy.2016.03.113.

[54] J. Cot-Gores, A. Castell, L.F. Cabeza, Thermochemical energy storage and conversion: A-state-of-the-art review of the experimental research under practical conditions, Renew. Sustain. Energy Rev. 16 (2012) 5207–5224. doi:10.1016/j.rser.2012.04.007.

[55] F. Trausel, A.J. De Jong, R. Cuypers, A review on the properties of salt hydrates for thermochemical storage, Energy Procedia. 48 (2014) 447–452. doi:10.1016/j.egypro.2014.02.053.

[56] Y.D. Palacios, Anabel, Maria Elena Navarro, Camila Barreneche, Thermochemical Water-sorption materials screening for Thermal Energy Storage: building application, in: Eurotherm Semin. #112 Adv. Therm. Energy Storage, 2019.

[57] A. Gutierrez, M. Linder, Bromide salts for thermochemical heat upgrade and storage: Investigation of the reversibility of reactions, in: Eurotherm Semin. #112 Adv. Therm. Energy Storage, 2019.

[58] K.E. N'Tsoukpoe, T. Schmidt, H.U. Rammelberg, B.A. Watts, W.K.L. Ruck, A systematic multi-step screening of numerous salt hydrates for low temperature thermochemical energy storage, Appl. Energy. 124 (2014) 1–16. doi:10.1016/j.apenergy.2014.02.053.

[59] T. Yan, R.Z. Wang, T.X. Li, L.W. Wang, I.T. Fred, A review of promising candidate reactions for chemical heat storage, Renew. Sustain. Energy Rev. 43 (2015) 13–31. doi:10.1016/j.rser.2014.11.015.

[60] M. Deutsch, D. Müller, C. Aumeyr, C. Jordan, C. Gierl-Mayer, P. Weinberger, F. Winter, A. Werner, Systematic search algorithm for potential thermochemical energy storage systems, Appl. Energy. 183 (2016) 113–120. doi:10.1016/j.apenergy.2016.08.142.

[61] P.A.J. Donkers, L.C. Sögütoglu, H.P. Huinink, H.R. Fischer, O.C.G. Adan, A review of salt hydrates for seasonal heat storage in domestic applications, Appl. Energy. 199 (2017) 1–26. doi:https://doi.org/10.1016/j.apenergy.2017.04.080.

[62] M. Richter, E.M. Habermann, E. Siebecke, M. Linder, A systematic screening of salt hydrates as materials for a thermochemical heat transformer, Thermochim. Acta. 659 (2018) 136–150. doi:10.1016/j.tca.2017.06.011.

[63] P.A.J. Donkers, L. Pel, O.C.G. Adan, Experimental studies for the cyclability of salt hydrates for thermochemical heat storage, J. Energy Storage. 5 (2016)

25–32. doi:10.1016/j.est.2015.11.005.

[64] S. Kiyabu, J.S. Lowe, A. Ahmed, D.J. Siegel, Computational Screening of Hydration Reactions for Thermal Energy Storage: New Materials and Design Rules, Chem. Mater. 13 (2018) 5. doi:10.1021/acs.chemmater.7b05230.

[65] S. Afflerbach, R. Trettin, A systematic screening approach for new materials for thermochemical energy storage and conversion based on the Strunz mineral classification system, Thermochim. Acta. 674 (2019) 82–94. doi:10.1016/j.tca.2019.02.010.

[66] Y. Ammar, S. Joyce, R. Norman, Y. Wang, A.P. Roskilly, Low grade thermal energy sources and uses from the process industry in the UK, Appl. Energy. 89 (2012) 3–20. doi:10.1016/j.apenergy.2011.06.003.

[67] N. Yes ßiller, J.L. Hanson, E.H. Yee, Waste heat generation: A comprehensive review, Waste Manag. 42 (2015) 166–179. doi:10.1016/j.wasman.2015.04.004.

[68] M. Wahlroos, M. Pärssinen, S. Rinne, S. Syri, J. Manner, Future views on waste heat utilization – Case of data centers in Northern Europe, Renew. Sustain. Energy Rev. 82 (2018) 1749–1764. doi:10.1016/j.rser.2017.10.058.

[69] L.F. Cabeza, A. Castell, C. Barreneche, A. De Gracia, A.I. Fernández, Materials used as PCM in thermal energy storage in buildings: A review, Renew. Sustain. Energy Rev. 15 (2011) 1675–1695. doi:10.1016/j.rser.2010.11.018.

[70] V.M. van Essen, H. a. Zondag, J.C. Gores, L.P.J. Bleijendaal, M. Bakker, R. Schuitema, W.G.J. van Helden, Z. He, C.C.M. Rindt, Characterization of MgSO4 Hydrate for Thermochemical Seasonal Heat Storage, J. Sol. Energy Eng. 131 (2009) 041014. doi:10.1115/1.4000275.

[71] F. Bertsch, B. Mette, S. Asenbeck, H. Kerskes, H. Müller-Steinhagen, Low temperature chemical heat storage–an investigation of hydration reactions, Effstock Conf. Stock. (2009) 1–8. doi:10.1049/iet-smt:20080075.

[72] L. Okhrimenko, L. Favergeon, K. Johannes, F. Kuznik, M. Pijo-lat, F. Kuznik, M. Pijolat, Thermodynamic study of MgSO4-H2O system dehydration at low pressure in view of heat storage, (2017). doi:10.1016/j.tca.2017.08.015.

[73] K. Linnow, M. Niermann, D. Bonatz, K. Posern, M. Steiger, Experimental studies of the mechanism and kinetics of hydration reactions, Energy Procedia. 48 (2014) 394–404. doi:10.1016/j.egypro.2014.02.046.

[74] E. Ruiz-Agudo, J.D. Martín-Ramos, C. Rodriguez-Navarro, Mechanism and kinetics of dehydration of epsomite crystals formed in the presence of organic additives, J. Phys. Chem. B. 111 (2007) 41–52. doi:10.1021/jp064460b.

[75] C.J. Ferchaud, R.A.A. Scherpenborg, H.A. Zondag, R. De Boer, Thermochemical seasonal solar heat storage in salt hydrates for residential applications - Influence of the water vapor pressure on the desorption kinetics of MgSO4·7H2O, Energy Procedia. 57 (2014) 2436–2440. doi:10.1016/j.egypro.2014.10.252.

[76] C.J. Ferchaud, H.A. Zondag, J.B.J. Veldhuis, R. De Boer, Study of the reversible water vapour sorption process of MgSO 4.7H2O and MgCl2.6H2O under the conditions of seasonal solar heat storage, J. Phys. Conf. Ser. 395 (2012). doi:10.1088/1742-6596/395/1/012069.

[77] K.E. N'Tsoukpoe, H.U. Rammelberg, A.F. Lele, K. Korhammer, B.A. Watts, T. Schmidt, W.K.L. Ruck, A review on the use of calcium chloride in

applied thermal engineering, Appl. Therm. Eng. 75 (2015) 513–531. doi:10.1016/j.applthermaleng.2014.09.047.

[78] A. Fopah-Lele, J.G. Tamba, A review on the use of SrBr2·6H2O as a potential material for low temperature energy storage systems and building applications, Sol. Energy Mater. Sol. Cells. 164 (2017) 175–187. doi:10.1016/j.solmat.2017.02.018.

[79] H.A. Zondag, V.M. Van Essen, M. Bakker, Application of MgCl 2 · 6H 2 O for thermochemical seasonal solar heat storage, Ires 2010. (2010) 22–24.

[80] L.C. Sögütoglu, P.A.J. Donkers, H.R. Fischer, H.P. Huinink, O.C.G. Adan, In-depth investigation of thermochemical performance in a heat battery: cyclic analysis of K2CO3, MgCl2 and Na2S, 215 (2018) 159–173. doi:10.1016/j.apenergy.2018.01.083.

[81] A.D. Pathak, S. Nedea, H. Zondag, C. Rindt, D. Smeulders, A DFT-based comparative equilibrium study of thermal dehydration and hydrolysis of CaCl2 hydrates and MgCl2 hydrates for seasonal heat storage, Phys. Chem. Chem. Phys. 18 (2016) 10059–10069. doi:10.1039/c6cp00926c.

[82] H.U. Rammelberg, T. Schmidt, W. Ruck, Hydration and dehydration of salt hydrates and hydroxides for thermal energy storage - Kinetics and energy release, Energy Procedia. 30 (2012) 362–369. doi:10.1016/j.egypro.2012.11.043.

[83] Q. Huang, G. Lu, J. Wang, J. Yu, Thermal decomposition mechanisms of MgCl2·6H2O and MgCl2·H2O, J. Anal. Appl. Pyrolysis. 91 (2011) 159–164. doi:10.1016/j.jaap.2011.02.005.

[84] M. Gaeini, S.A. Shaik, C.C.M. Rindt, Characterization of potassium carbonate salt hydrate for thermochemical energy storage in buildings, Energy Build. 196 (2019) 178–193. doi:10.1016/j.enbuild.2019.05.029.

[85] M. Roelands, R. Cuypers, K.D. Kruit, H. Oversloot, A.J. De Jong, W. Duvalois, L. Van Vliet, C. Hoegaerts, Preparation & Characterization of Sodium Sulfide Hydrates for Application in Thermochemical Storage Systems, Energy Procedia. 70 (2015) 257–266. doi:10.1016/j.egypro.2015.02.122.

[86] R. De Boer, W.G. Haije, J.B.J. Veldhuis, Determination of structural , thermodynamic and phase properties in the Na2S–H2O system for application in a chemical heat pump, Thermochim. Acta. 395 (2003) 3–19.

[87] D.K. Sahoo, R. Mishra, H. Singh, N. Krishnamurthy, Determination of thermodynamic stability of lanthanum chloride hydrates (LaCl3·H2O) by dynamic transpiration method, J. Alloys Compd. 588 (2014) 578–584. doi:10.1016/j.jallcom.2013.11.115.

[88] A. Gutierrez, L. Miró, A. Gil, J. Rodríguez-Aseguinolaza, C. Barreneche, N. Calvet, X. Py, A. Inés Fernández, M. Grágeda, S. Ushak, L.F. Cabeza, Advances in the valorization of waste and by-product materials as thermal energy storage (TES) materials, Renew. Sustain. Energy Rev. 59 (2016) 763–783. doi:10.1016/j.rser.2015.12.071.

[89] A. Gutierrez, S. Ushak, M. Linder, High Carnallite-Bearing Material for Thermochemical Energy Storage: Thermophysical Characterization, ACS Sustain. Chem. Eng. 6 (2018) 6135–6145. doi:10.1021/acssuschemeng.7b04803.

[90] H.U. Rammelberg, T. Osterland, B. Priehs, O. Opel, W.K.L. Ruck, Thermochemical heat storage materials - Performance of mixed salt hydrates, Sol. Energy. 136 (2016) 571–589. doi:10.1016/j.solener.2016.07.016.

[91]   A.K. Galwey, N. Koga, H. Tanaka, A kinetic and microscopic investigation of the thermal dehydration of lithium sulphate monohydrate, J. Chem. Soc. Faraday Trans. 86 (1990) 531–537. doi:10.1039/FT9908600531.

[92]   M.A.J.M. Beving, A.J.H. Frijns, C.C.M. Rindt, D.M.J. Smeulders, Characterization and modelling of K2CO3 cycles for thermochemical energy storage applications, in: EUROTHERM #112 Adv. Therm. Energy Storage, 2019.

[93]   M. Richter, E. Habermann, E. Siebecke, M. Linder, A systematic screening of salt hydrates as materials for a thermochemical heat transformer, Thermochim. Acta. 659 (2018) 136–150. doi:10.1016/j.tca.2017.06.011.

[94]   B. Fumey, R. Weber, L. Baldini, Sorption based long-term thermal energy storage – Process classification and analysis of performance limitations: A review, Renew. Sustain. Energy Rev. 111 (2019) 57–74. doi:10.1016/j.rser.2019.05.006.

[95]   A. Solé, L. Miró, C. Barreneche, I. Martorell, L.F. Cabeza, Corrosion of metals and salt hydrates used for thermochemical energy storage, Renew. Energy. 75 (2015) 519–523. doi:10.1016/j.renene.2014.09.059.

[96]   A. Solé, L. Miró, C. Barreneche, I. Martorell, L.F. Cabeza, Corrosion Test of Salt Hydrates and Vessel Metals for Thermochemical Energy Storage, Energy Procedia. 48 (2014) 431–435. doi:10.1016/j.egypro.2014.02.050.

[97]   P. D'Ans, E. Courbon, M. Frère, G. Descy, T. Segato, M. Degrez, Severe corrosion of steel and copper by strontium bromide in thermochemical heat storage reactors, Corros. Sci. 138 (2018) 275–283. doi:10.1016/j.corsci.2018.04.020.

[98]   A. Fopah-Lele, C. Rohde, K. Neumann, T. Tietjen, T.R.€ Onnebeck A , Kokouvi Edem N'tsoukpoe, T. Osterland, O. Opel, W.K.L. Ruck, Lab-scale experiment of a closed thermochemical heat storage system including honeycomb heat exchanger, (2016). doi:10.1016/j.energy.2016.08.009.

[99]   F. Kleiner, K. Posern, A. Osburg, Thermal conductivity of selected salt hydrates for thermochemical solar heat storage applications measured by the light flash method, Appl. Therm. Eng. 113 (2017) 1189–1193. doi:10.1016/j.applthermaleng.2016.11.125.

[100] R.S. Graves, T.G. Kollie, D.L. McElroy, K.E. Gilchrist, The thermal conductivity of AISI 304L stainless steel, Int. J. Thermophys. 12 (1991) 409–415. doi:10.1007/BF00500761.

[101] K. Korhammer, M.-M. Druske, A. Fopah-Lele, H.U. Rammelberg, N. Wegscheider, O. Opel, T. Osterland, W. Ruck, Sorption and thermal characterization of composite materials based on chlorides for thermal energy storage, Appl. Energy. 162 (2016) 1462–1472. doi:10.1016/j.apenergy.2015.08.037.

[102] L. Scapino, H.A. Zondag, J. Van Bael, J. Diriken, C.C.M. Rindt, Sorption heat storage for long-term low-temperature applications: A review on the advancements at material and prototype scale, Appl. Energy. 190 (2017) 920–948. doi:10.1016/j.apenergy.2016.12.148.

[103] A. Solé, I. Martorell, L.F. Cabeza, State of the art on gas-solid thermochemical energy storage systems and reactors for building applications, Renew. Sustain. Energy Rev. 47 (2015) 386–398. doi:10.1016/j.rser.2015.03.077.

[104] A.D. Pathak, I. Tranca, S. V. Nedea, H.A. Zondag, C.C.M. Rindt, D.M.J. Smeulders, First-Principles Study of Chemical Mixtures of CaCl2 and MgCl2 Hydrates for Optimized Seasonal Heat Storage, J. Phys. Chem. C.

121 (2017) 20576–20590. doi:10.1021/acs.jpcc.7b05245.

[105] H.U. Rammelberg, M. Myrau, T. Schmidt, W. Ruck, An optimization of salt hydrates for thermochemical heat storage, Int. Symp. Innov. Mater. Process. Energy Syst. 2013 Fukuoka, Japan. (2013).

[106] K. Posern, C. Kaps, Calorimetric studies of thermochemical heat storage materials based on mixtures of MgSO4 and MgCl2, Thermochim. Acta. 502 (2010) 73–76. doi:10.1016/j.tca.2010.02.009.

[107] O. Opel, H.. Rammelburg, M. Gerard, W. Ruck, Thermochemical Storage Materials Research - Tga / Dsc-Hydration Studies, (2006).

[108] Y.E. Milián, A. Gutiérrez, M. Grágeda, S. Ushak, A review on encapsulation techniques for inorganic phase change materials and the influence on their thermophysical properties, Renew. Sustain. Energy Rev. 73 (2017) 983–999. doi:10.1016/j.rser.2017.01.159.

[109] M. Gaeini, A.L. Rouws, J.W.O. Salari, H.A. Zondag, C.C.M. Rindt, Characterization of microencapsulated and impregnated porous host materials based on calcium chloride for thermochemical energy storage, Appl. Energy. 212 (2018) 1165–1177. doi:10.1016/j.apenergy.2017.12.131.

[110] V. Brancato, L. Calabrese, V. Palomba, A. Frazzica, M. Fullana-Puig, A. Solé, L.F. Cabeza, MgSO4·7H2O filled macro cellular foams: An innovative composite sorbent for thermo-chemical energy storage applications for solar buildings, Sol. Energy. 173 (2018) 1278–1286. doi:10.1016/j.solener.2018.08.075.

[111] S.Z. Xu, R.Z. Wang, L.W. Wang, J. Zhu, Performance characterizations and thermodynamic analysis of magnesium sulfate-impregnated zeolite 13X and activated alumina composite sorbents for thermal energy storage, Energy. (2019) 889–901. doi:10.1016/j.energy.2018.10.200.

[112] A. Jabbari-Hichri, S. Bennici, A. Auroux, CaCl2-containing composites as thermochemical heat storage materials, Sol. Energy Mater. Sol. Cells. 172 (2017) 177–185. doi:10.1016/j.solmat.2017.07.037.

[113] A. Mehrabadi, M. Farid, New salt hydrate composite for low-grade thermal energy storage, Energy. 164 (2018) 194–203. doi:10.1016/j.energy.2018.08.192.

[114] B.L.J.I. R. Cuypers, A.J. de Jong, J. Eversdijk, H. van 't Spijker, H. Oversloot, and N.E.P.-B. R.K.H. Cremers, Microencapsulation of Salts for Enhanced Thermochemical Storage Materials, in: 40th Annu. Meet. Expo. Control. Release Soc. 21-24 July 2013, Honolulu, Hawaii, USA, 1-2, 2013. http://ci.nii.ac.jp/naid/10016489498/.

[115] P.A. Kallenberger, K. Posern, K. Linnow, F.J. Brieler, M. Steiger, M. Fröba, Alginate-Derived Salt/Polymer Composites for Thermochemical Heat Storage, 1700160 (2018) 1–8. doi:10.1002/adsu.201700160.

[116] P.A. Kallenberger, F.J. Brieler, K. Posern, M. Fröba, Magnesium Sulfate/Polymer Composites for Seasonal, Thermochemical Energy Storage, Chemie-Ingenieur-Technik. 88 (2016) 379–384. doi:10.1002/cite.201500095.

[117] A. Celzard, J.F. Marêché, G. Furdin, Surface area of compressed expanded graphite, Carbon N. Y. 40 (2002) 2713–2718. doi:10.1016/S0008-6223(02)00183-5.

[118] A. Cammarata, V. Verda, A. Sciacovelli, Y. Ding, Hybrid strontium bromide-natural graphite composites for low to medium temperature thermochemical energy storage: Formulation, fabrication and performance investigation, Energy Convers. Manag. 166 (2018) 233–240.

doi:10.1016/j.enconman.2018.04.031.

[119] Y.J. Zhao, R.Z. Wang, Y.N. Zhang, N. Yu, Development of SrBr2 composite sorbents for a sorption thermal energy storage system to store low-temperature heat, Energy. 115 (2016) 129–139. doi:10.1016/j.energy.2016.09.013.

[120] M.-M. Druske, A. Fopah-Lele, K. Korhammer, H.U. Rammelberg, N. Wegscheider, W. Ruck, T. Schmidt, Developed Materials for Thermal Energy Storage: Synthesis and Characterization, Energy Procedia. 61 (2014) 96–99. doi:10.1016/j.egypro.2014.11.915.

[121] N. Yu, R.Z. Wang, Z.S. Lu, L.W. Wang, Study on consolidated composite sorbents impregnated with LiCl for thermal energy storage, Int. J. Heat Mass Transf. 84 (2015) 660–670. doi:10.1016/j.ijheatmasstransfer.2015.01.065.

[122] G. Krese, R. Koželj, V. Butala, U. Stritih, Thermochemical seasonal solar energy storage for heating and cooling of buildings, Energy Build. 164 (2018) 239–253. doi:10.1016/j.enbuild.2017.12.057.

[123] A.H. Abedin, M.A. Rosen, Closed and open thermochemical energy storage: Energy- and exergy-based comparisons, Energy. 41 (2012) 83–92. doi:10.1016/j.energy.2011.06.034.

[124] W. Streicher, Solar Thermal Technologies for Domestic Hot Water Preparation and Space Heating, Elsevier Ltd, 2015. doi:10.1016/B978-1-78242-213-6.00002-3.

[125] L. Glasser, Thermodynamics of inorganic hydration and of humidity control, with an extensive database of salt hydrate pairs, J. Chem. Eng. Data. 59 (2014) 526–530. doi:10.1021/je401077x.

[126] E.M. Collins, A.W.C. Menzies, A Comparative Method for Measuring Aqueous Vapor and Dissociation Pressures with Some of its Applications, J. Phys. Chem. 40 (1935) 379–397. doi:10.1021/j150372a010.

[127] B. Michel, N. Mazet, S. Mauran, D. Stitou, J. Xu, Thermochemical process for seasonal storage of solar energy: Characterization and modeling of a high density reactive bed, Energy. 47 (2012) 553–563. doi:10.1016/j.energy.2012.09.029.

[128] NIST, Antoine equation parameters for water, (n.d.). https://webbook.nist.gov/cgi/cbook.cgi?ID=C7732185&Mask=4&Type=ANTOINE&Plot=on#ANTOINE.

[129] L.C. Sögütoglu, M. Steiger, J. Houben, D. Biemans, H.R. Fischer, P. Donkers, H. Huinink, O.C.G. Adan, Understanding the Hydration Process of Salts: The Impact of a Nucleation Barrier, Cryst. Growth Des. 19 (2019) 2279–2288. doi:10.1021/acs.cgd.8b01908.

[130] Y.N. Zhang, R.Z. Wang, T.X. Li, Experimental investigation on an open sorption thermal storage system for space heating, 141 (2017) 2421–2433. doi:10.1016/j.energy.2017.12.003.

[131] M. Gaeini, M.R. Javed, H. Ouwerkerk, H.A. Zondag, C.C.M. Rindt, Realization of a 4kW thermochemical segmented reactor in household scale for seasonal heat storage, Energy Procedia. 135 (2017) 105–114. doi:10.1016/j.egypro.2017.09.491.

[132] K. Johannes, F. Kuznik, J. Hubert, F. Durier, C. Obrecht, Design and characterisation of a high powered energy dense zeolite thermal energy storage system for buildings, 159 (2015) 80–86. doi:10.1016/j.apenergy.2015.08.109.

[133] V. Palomba, S. Vasta, A. Freni, Experimental testing of AQSOA FAM Z02 / water adsorption system for heat and cold storage, Appl. Therm. Eng. 124

(2017) 967–974. doi:10.1016/j.applthermaleng.2017.06.085.

[134] B. Michel, N. Mazet, P. Neveu, Experimental investigation of an innovative thermochemical process operating with a hydrate salt and moist air for thermal storage of solar energy: Global performance, Appl. Energy. 129 (2014) 177–186. doi:10.1016/j.apenergy.2014.04.073.

[135] S. Lan, M. Gaeini, H. Zondag, A. Van Steenhoven, C. Rindt, Direct numerical simulation of the thermal dehydration reaction in a TGA experiment, Appl. Therm. Eng. 128 (2018) 1175–1185. doi:10.1016/j.applthermaleng.2017.08.073.

[136] A.A. Hawwash, S. Mori, K. El Feky, H. Hassan, Numerical Study for Open Reactor Design Using Salt Hydrate Numerical Study for Open Reactor Design Using Salt Hydrate, in: 2019 Int. Conf. Smart Power Internet Energy Syst., 2019. doi:10.1088/1755-1315/322/1/012021.

[137] C. Xu, Y. Xie, Z. Liao, Y. Ren, F. Ye, Numerical study on the desorption process of a thermochemical reactor filled with MgCl2·6H2O for seasonal heat storage, Appl. Therm. Eng. 146 (2019) 785–794. doi:10.1016/j.applthermaleng.2018.10.019.

[138] A. Fopah Lele, F. Kuznik, O. Opel, W.K.L. Ruck, Performance analysis of a thermochemical based heat storage as an addition to cogeneration systems, Energy Convers. Manag. 106 (2015) 1327–1344. doi:10.1016/j.enconman.2015.10.068.

[139] M. Henriksson, G. Henriksson, L.A. Berglund, T. Lindström, An environmentally friendly method for enzyme-assisted preparation of microfibrillated cellulose (MFC) nanofibers, Eur. Polym. J. 43 (2007) 3434–3441. doi:10.1016/j.eurpolymj.2007.05.038.

[140] F. Carosio, J. Kochumalayil, F. Cuttica, G. Camino, L. Berglund, Oriented Clay Nanopaper from Biobased Components - Mechanisms for Superior Fire Protection Properties, ACS Appl. Mater. Interfaces. 7 (2015) 5847–5856. doi:10.1021/am509058h.

[141] M. Gustavsson, E. Karawacki, S.E. Gustafsson, Thermal conductivity, thermal diffusivity, and specific heat of thin samples from transient measurements with hot disk sensors, Rev. Sci. Instrum. 65 (1994) 3856–3859. doi:10.1063/1.1145178.

[142] B. Sandnes, J. Rekstad, Supercooling salt hydrates: Stored enthalpy as a function of temperature, Sol. Energy. 80 (2006) 616–625. doi:10.1016/j.solener.2004.11.014.

[143] T. Wada, R. Yamamoto, Y. Matsuo, Heat storage capacity of sodium acetate trihydrate during thermal cycling, Sol. Energy. 33 (1984) 373–375. doi:10.1016/0038-092X(84)90169-5.

[144] R. Naumann, T. Fanghanel, H.-H. Emons, THERMOANALYTICAL INVESTIGATION OF SODIUM ACETATE TRIHYDRATE FOR APPLICATION AS A LATENT HEAT THERMAL ENERGY STORAGE MATERIAL, J. Therm. Anal. 33 (1988) 685–690.

[145] J. Lu, I. Do, H. Fukushima, I. Lee, L.T. Drzal, Stable aqueous suspension and self-assembly of graphite nanoplatelets coated with various polyelectrolytes, J. Nanomater. 2010 (2010). doi:10.1155/2010/186486.

[146] C. Qin, Y. Feng, H. An, J. Han, C. Cao, W. Feng, Tetracarboxylated Azobenzene/Polymer Supramolecular Assemblies as High-Performance Multiresponsive Actuators * S Supporting Information, ACS Appl. Mater. Interfaces. 9 (2017) 58. doi:10.1021/acsami.6b15075.

[147] J. Chong, S. Xun, H. Zheng, X. Song, G. Liu, P. Ridgway, J.Q. Wang, V.S.

Battaglia, A comparative study of polyacrylic acid and poly(vinylidene difluoride) binders for spherical natural graphite/LiFePO 4 electrodes and cells, J. Power Sources. 196 (2011) 7707–7714. doi:10.1016/j.jpowsour.2011.04.043.

[148] W. Qi, R. Lv, B. Na, H. Liu, Y. He, N. Yu, Nanocellulose-Assisted Growth of Manganese Dioxide on Thin Graphite Papers for High-Performance Supercapacitor Electrodes, ACS Sustain. Chem. Eng. 6 (2018) 4739–4745. doi:10.1021/acssuschemeng.7b03858.

[149] M. Dannemand, J. Dragsted, J. Fan, J.B. Johansen, W. Kong, S. Furbo, Experimental investigations on prototype heat storage units utilizing stable supercooling of sodium acetate trihydrate mixtures, Appl. Energy. 169 (2016) 72–80. doi:10.1016/j.apenergy.2016.02.038.

[150] T. Brünig, K. Krekić, C. Bruhn, R. Pietschnig, Calorimetric Studies and Structural Aspects of Ionic Liquids in Designing Sorption Materials for Thermal Energy Storage, Chem. - A Eur. J. 22 (2016) 16200–16212. doi:10.1002/chem.201602723.

[151] JCPDS-ICDD, (n.d.). http://www.icdd.com/ (accessed December 10, 2018).

[152] M. Inoue, I. Hirasawa, The relationship between crystal morphology and XRD peak intensity on CaSO4·2H2O, J. Cryst. Growth. 380 (2013) 169–175. doi:10.1016/j.jcrysgro.2013.06.017.

[153] P. Batys, Y. Zhang, J.L. Lutkenhaus, M. Sammalkorpi, Hydration and Temperature Response of Water Mobility in Poly(diallyldimethylammonium)-Poly(sodium 4-styrenesulfonate) Complexes, Macromolecules. 51 (2018) 8268–8277. doi:10.1021/acs.macromol.8b01441.

[154] A. Fopah, F. Kuznik, O. Opel, W.K.L. Ruck, Performance analysis of a thermochemical based heat storage as an addition to cogeneration systems, Energy Convers. Manag. 106 (2015) 1327–1344. doi:10.1016/j.enconman.2015.10.068.

[155] S. Deville, E. Saiz, R.K. Nalla, A.P. Tomsia, Freezing as a Path to Build Complex Composites, 515 (2006). doi:10.1126/science.1120937.

[156] L. Medina, F. Carosio, L.A. Berglund, Recyclable nanocomposite foams of Poly(vinyl alcohol), clay and cellulose nanofibrils – Mechanical properties and flame retardancy, Compos. Sci. Technol. 182 (2019) 107762. doi:10.1016/j.compscitech.2019.107762.

[157] K.J. De France, T. Hoare, E.D. Cranston, Review of Hydrogels and Aerogels Containing Nanocellulose, Chem. Mater. 29 (2017) 4609–4631. doi:10.1021/acs.chemmater.7b00531.

[158] H. Tamon, H. Ishizaka, T. Yamamoto, T. Suzuki, Preparation of mesoporous carbon by freeze drying, Carbon N. Y. 37 (1999) 2049–2055. doi:10.1016/S0008-6223(99)00089-5.

[159] S.M. Jung, D.L. Mafra, C. Te Lin, H.Y. Jung, J. Kong, Controlled porous structures of graphene aerogels and their effect on supercapacitor performance, Nanoscale. 7 (2015) 4386–4393. doi:10.1039/c4nr07564a.

[160] K. Posern, K. Linnow, M. Niermann, C. Kaps, M. Steiger, Thermochemical investigation of the water uptake behavior of MgSO4 hydrates in host materials with different pore size, Thermochim. Acta. 611 (2015) 1–9. doi:10.1016/j.tca.2015.04.031.

[161] T. Nagel, S. Beckert, C. Lehmann, R. Gläser, O. Kolditz, Multi-physical continuum models of thermochemical heat storage and transformation in porous media and powder beds-A review, Appl. Energy. 178 (2016) 323–

345. doi:10.1016/j.apenergy.2016.06.051.

[162] Y.N. Zhang, R.Z. Wang, Y.J. Zhao, T.X. Li, S.B. Riffat, N.M. Wajid, Development and thermochemical characterizations of vermiculite/SrBr2 composite sorbents for low-temperature heat storage, Energy. 115 (2016) 120–128. doi:10.1016/j.energy.2016.08.108.

[163] A. Bahadori, S. Zendehboudi, G. Zahedi, Estimation of Mixing Ratio for Saturated Air over Water, Chem. Eng. Technol. 36 (2013) 109–114. doi:10.1002/ceat.201200211.